
A Setup for High-Resolution Imaging of Ultracold Lithium Atoms

DISSERTATION

zur Erlangung des Doktorgrades

an der Fakultät für Mathematik, Informatik und Naturwissenschaften

im Fachbereich Physik

der Universität Hamburg

vorgelegt von

Michael Hubertus HAGEMANN

geboren in

Hamburg

Hamburg

2020

Gutachter

Gutachter der Dissertation:	Prof. Dr. Klaus Sengstock Prof. Dr. Henning Moritz
Gutachter der Disputation:	Prof. Dr. Klaus Sengstock Prof. Dr. Henning Moritz Prof. Dr. Roman Schnabel Prof. Dr. Ludwig Mathey Prof. Dr. Markus Drescher
Vorsitzender der Prüfungskommission:	Prof. Dr. Roman Schnabel
Datum der Disputation:	11.02.2021
Vorsitzender des Promotionsausschusses:	Prof. Dr. Wolfgang Hansen
Leiter des Fachbereichs Physik:	Prof. Dr. Günter H. W. Sigl
Dekan der Fakultät für Mathematik, Informatik und Naturwissenschaften:	Prof. Dr. Heinrich Graener

Abstract

In the field of research of ultracold quantum gases, quantum gas microscopes have established as an effective tool for direct observation of spatial correlations and dynamics of an ultracold many-body system. This thesis describes the setup of a new experimental apparatus that aims for quantum gas microscopy of ultracold bosonic and fermionic lithium atoms to simulate atomic and molecular dynamics and to explore anyonic quantum particles.

Lithium atoms offer fast timescales and precise adjustment of their interaction strength. In addition it is possible to work with the bosonic isotope ${}^7\text{Li}$ or the fermionic isotope ${}^6\text{Li}$ in the same experimental apparatus separate from only small technical changes. The combination of this element with the single-atom sensitivity of a quantum gas microscope is a very promising but also technically demanding experimental platform.

The experimental setup to achieve this goal is described in detail in this thesis. We build a compact 2D-/3D-MOT setup without any further transport to facilitate short experimental cycle times. This enables measurements that require very high statistics. The addition of gray molasses cooling and a far-detuned high-power optical dipole trap allows us to routinely produce quantum degenerate gases of lithium atoms.

Single-atom sensitive imaging for lithium atoms requires a very deep optical lattice and an effective cooling mechanism to pin the atoms on their respective lattice site during the imaging process. We build and characterize an accordion lattice along the vertical direction for the preparation of a single plane of atoms and a triangular lattice for the horizontal plane.

For cooling of the atoms in the optical lattice we prepare our experimental setup for the implementation of Raman sideband cooling. Measurements of two-photon Raman transitions and Rabi oscillations as intermediate steps to the actual cooling of the atoms inside the lattice are presented in this thesis. In addition we build an imaging setup for the realization of the necessary high optical resolution. At the end of this thesis an outlook is given on the upcoming experimental steps and on the research projects that shall be realized in the future.

Zusammenfassung

In dem Forschungsgebiet der ultrakalten Quantengase haben sich Quantengasmikroskope als ein effektives Werkzeug zur direkten Beobachtung von räumlichen Korrelationen und Dynamiken eines ultrakalten Vielteilchensystems etabliert. Diese Arbeit beschreibt den Aufbau eines neuen Experiments zur Realisierung von Quantengasmikroskopie bosonischer und fermionischer Lithium-Atome zur Simulation von atomarer und molekularer Dynamik und für die Untersuchung von anyonischen Quantenteilchen.

Lithium-Atome verfügen über schnelle Zeitskalen und ermöglichen die präzise Einstellung ihrer Wechselwirkungsstärke. Darüber hinaus müssen nur kleine technische Änderungen vorgenommen werden, um in demselben Experiment sowohl mit dem bosonischen Isotop ^7Li als auch mit dem fermionischen Isotop ^6Li arbeiten zu können. Die Kombination dieses atomaren Elements mit der Sensitivität für einzelne Atome eines Quantengasmikroskops ist eine vielversprechende aber auch technisch anspruchsvolle experimentelle Plattform.

Der experimentelle Aufbau, mit dem dieses Ziel erreicht werden soll, wird in dieser Arbeit im Detail beschrieben. Wir verwenden einen kompakten 2D-/3D-MOT Aufbau ohne anschließenden Transport, um kurze experimentelle Zykluszeiten zu erreichen. Dies ermöglicht Messungen, die sehr hohe Statistik erfordern. Durch das Hinzufügen einer Graue-Melasse-Kühlung und einer weit verstimzten Dipolfalle mit hoher Leistung können wir routinemäßig ultrakalte Quantengase mit Lithium-Atomen erzeugen.

Das Abbilden von einzelnen Lithium-Atomen erfordert ein sehr tiefes optisches Gitter und einen effektiven Kühlmechanismus, um die Atome während des Abbildungsprozesses auf ihrem jeweiligen Gitterplatz zu fixieren. Wir konstruieren und charakterisieren ein Akkordeongitter entlang der vertikalen Richtung für die Präparation einer einzelnen Ebene von Atomen und wir verwenden ein Dreiecksgitter für die horizontale Ebene.

Um die Atome im optischen Gitter kühlen zu können, bereiten wir das Experiment für die Implementierung von Raman-Seitenband-Kühlen vor. Im Zuge dessen werden in dieser Arbeit Messungen der Raman Zwei-Photonen-Übergänge und der Rabi-Oszillationen als Zwischenschritte zur tatsächlichen Kühlung der Atome im Gitter präsentiert. Darüber hinaus wird ein Abbildungssystem zur Realisierung der benötigten hohen optischen Auflösung aufgebaut. Am Ende dieser Arbeit wird ein Ausblick gegeben auf die kommenden experimentellen Schritte und auf die Forschungsvorhaben, die in Zukunft realisiert werden sollen.

Contents

1	Introduction	1
2	A quantum gas microscope for lithium atoms	5
2.1	Bosonic and fermionic lithium atoms	5
2.2	Quantum gas microscopy	6
2.2.1	A short introduction to quantum gas microscopes	6
2.2.2	High-resolution microscope objective	7
2.2.3	Optical pinning lattices	8
2.2.4	Accordion lattice	10
2.2.5	Triangular lattice	11
2.2.6	Cooling mechanisms for atoms in an optical lattice	14
2.2.7	Raman sideband cooling	14
3	Experimental apparatus	17
3.1	Vacuum chamber	17
3.1.1	Principal design considerations	17
3.1.2	Vacuum setup	18
3.1.3	Steel chamber	19
3.1.4	Science cell	20
3.2	Laser system for near-resonant light	22
3.2.1	2D-/3D-MOT and gray molasses	22
3.2.2	Low- and high-field imaging	24
3.2.3	Raman sideband cooling	24
3.3	Crossed dipole trap	29
3.4	Accordion lattice	31
3.5	Triangular lattice	32
3.6	High resolution imaging setup	34
4	Magnetic field coils	39
4.1	Magnetic fields for ultracold atoms	39
4.2	MOT coils, Feshbach coils and Tilt coil	41
4.2.1	Requirements and restrictions for the design of the coils	42
4.2.2	Simulation of the coil properties	42
4.2.3	Fabrication of the coils	45
4.2.4	Measurement of the coil properties	48
4.2.5	Magnetic field configurations	49

4.3	Offset coils	56
4.4	High currents and water cooling	57
4.4.1	Infrastructure for high currents	58
4.4.2	Switching high currents	59
4.4.3	Active current control	61
4.4.4	Infrastructure for water cooling	62
5	Creation of ultracold lithium gases	65
5.1	Initial laser cooling	65
5.1.1	2D- and 3D-MOT	65
5.1.2	Compressed MOT	68
5.1.3	Gray molasses	68
5.2	Evaporative cooling	70
5.2.1	Molecular BEC	70
5.2.2	Degenerate Fermi gas	73
6	Optical lattices	75
6.1	Accordion lattice	75
6.1.1	Adjustment of the lattice beams	75
6.1.2	Analysis of the lattice spacings	76
6.1.3	Compression of the accordion	78
6.1.4	Next steps	79
6.2	Triangular lattice	79
6.2.1	Adjustment of the lattice beams	80
6.2.2	Kapitza-Dirac scattering	81
6.2.3	Analysis of the lattice structure	82
6.2.4	Next steps	86
6.3	Implementation into the experimental cycle	87
7	Preparation of single-atom resolved imaging	91
7.1	Towards Raman sideband cooling	91
7.1.1	Adjustment of the Raman beams	91
7.1.2	Broadened Raman transition in the dipole trap	92
7.1.3	Narrow Raman transition in the 3D lattice	94
7.1.4	Rabi oscillations	95
7.1.5	Next steps	96
7.2	Implementation of high-resolution imaging	96
8	Conclusion & Outlook	99
8.1	Conclusion	99
8.2	Upcoming experimental steps	100
8.3	Prospective research topics	101
A	Level diagram of ${}^6\text{Li}$	105

B	Magnetic field shift of ${}^6\text{Li}$	107
C	Feshbach resonances of ${}^6\text{Li}$	111
D	Analysis of Kapitza-Dirac peaks	113
	List of Abbreviations	115
	List of Figures	117
	List of Tables	119
	Bibliography	121
	Danksagung	135

Chapter 1

Introduction

One of the main goals of science has always been to understand what are the smallest bricks of matter and how does their interplay define the shape of our world. Remarkable progress has been made in the course of time but the closer we want to look the more difficult it becomes. Even though, we have known for quite some time now that atoms are by far not the smallest particles that exist the fields of research of atomic and solid state physics still face a lot of fascinating and fundamental unsolved questions.

Real time observation of atomic or molecular motion and the interaction between particles is still a big challenge due to the small size and the fast timescales that need to be resolved and significant experimental effort is invested to achieve this goal. Although, we are able today to analytically or numerically calculate the behavior for at least a small number of interacting particles, the understanding of interacting many-body systems still remains a big challenge due to the exponential growth of the corresponding Hilbert space with every particle that is added to a system.

As a solution for the many-body problem, Richard Feynman proposed the concepts of *quantum computation* and *quantum simulation* in a seminal talk in 1982 [1]. A quantum computer [2, 3] consists of quantum mechanical qubits instead of classical bits. Every qubit is entangled with every other qubit. In this way the calculation time for physical systems whose complexity increases exponentially with every new particle could be solved in polynomial time. The idea of quantum simulation is to mimic a quantum system that might be hard to access with another quantum system which has similar properties but might be easier to prepare, manipulate and observe.

Ultracold quantum gases have emerged as one of the most fruitful platforms to perform quantum simulation. Since the experimental realization of the first Bose-Einstein condensates (BEC) in 1995 [4–6] they have proven to be a great toolkit for the analysis of a broad variety of quantum mechanical systems [7–11]. Quantum gases are very pure, can be precisely controlled and manipulated and they offer good possibilities for detection and analysis due to their mesoscopic size and their relatively slow dynamics [12–15]. In recent years the realization of quantum gas microscopy in optical lattices has enabled the advancement of imaging techniques for many-body systems to the single-atom level [16, 17].

The goal of this PhD thesis is to build an experiment that will enable quantum gas

microscopy of bosonic and fermionic lithium atoms. Beyond the regime of ultracold atoms in optical lattices for the simulation of solid state systems, that has already been the subject of intensive studies in the quantum gases community, we want to strive for the simulation of atomic and molecular dynamics with our experiment and seek for the measurement of exotic anyonic quantum particles.

This thesis is structured in the following way:

- **Chapter 2** motivates why we choose to work with bosonic and fermionic lithium atoms in our experiment. We give an introduction to the technique of quantum gas microscopy which we want to implement in our experiment. We emphasize the accordion lattice and the triangular lattice as they are the pinning lattices for our microscope and we provide an introduction to Raman sideband cooling as the cooling mechanism for the atoms in the pinning lattice that we aspire to implement in our experiment.
- **Chapter 3** is dedicated to a detailed description of our experimental apparatus. We begin with the vacuum chamber which consists of a compact steel chamber for the 2D-MOT and a glass cell for all further experimental steps. Next we describe the laser systems that create the near-resonant light for laser cooling, imaging and Raman sideband cooling. After that we focus on the crossed dipole trap and the accordion and triangular lattice. Finally we discuss our setup for single-atom resolved imaging based on an objective with a high numerical aperture.
- **Chapter 4** describes the magnetic field coils of our experiment. We discuss the process of planning, manufacturing and implementing this important part of the experiment. We review the different magnetic field configurations that can be created with our setup and we point out how we provide the necessary high currents and sufficient water cooling for the coils.
- **Chapter 5** shows typical experimental cycles for the creation of quantum degenerate samples. After the initial cooling steps of 2D- and 3D-MOT, compressed MOT and gray molasses we discuss the evaporative cooling sequences, whose efficiency is enhanced by making use of a magnetic Feshbach resonance, to create quantum degenerate gases of lithium atoms.
- **Chapter 6** discusses the implementation and characterization of our optical lattices. The description of both lattices, the vertical accordion lattice and the horizontal triangular lattice, begins with the procedure to adjust the lattices to the position of the ultracold atoms. For the accordion lattice we describe the analysis of the achievable lattice spacings and the dynamic compression of the atomic cloud to create a two-dimensional sample. For the triangular lattice we perform Kapitza-Dirac scattering and analyze the resulting images to determine the actual lattice angles.

- **Chapter 7** traces our way towards the realization of single-atom resolved imaging. We show our first measurements of the two-photon Raman transition and of Rabi oscillations. Then we discuss the implementation of an imaging setup with a high magnification to realize the aspired resolution in the near future.
- **Chapter 8** provides a conclusion about the work that has been done in the course of this PhD thesis. We outline the next experimental steps and give an overview over some of the possible research topics than can be addressed with this experimental setup in the future.

Among the support of several student assistants and Bachelor students the work presented in this thesis has been carried out by the author in collaboration with Andreas Kerkmann, Mathis Fischer, Justus Brüggjenjürgen, Tobias Petersen and Benno Rem. The principal investigators of the project are Klaus Sengstock and Christof Weitenberg. This thesis is the second PhD thesis of the project after the thesis of Andreas Kerkmann [18].

Chapter 2

A quantum gas microscope for lithium atoms

The main design decision at the begin of our new experiment was that we want to build a quantum gas microscope for ultracold bosonic and fermionic lithium atoms. In this chapter we motivate this decision and discuss some of the underlying concepts. We begin with the properties, advantages and challenges of lithium atoms for a quantum gas experiment and then we proceed with on the one hand the many possibilities for interesting experiments that are offered by quantum gas microscopes and on the other hand their significant technical demands and challenges.

2.1 Bosonic and fermionic lithium atoms

For the experimental setup that is described in this thesis we decide to work with either fermionic ${}^6\text{Li}$ or bosonic ${}^7\text{Li}$ atoms. The experiment is designed such that it is possible to work with one of the two isotopes at a time but not with both at the same time. ${}^7\text{Li}$ has a high natural abundance of 92.41 % and the abundance of ${}^6\text{Li}$ is only 7.59 % [19] but highly enriched samples of ${}^6\text{Li}$ are available for reasonable prices. In addition, a source for the bosonic rubidium isotopes ${}^{85}\text{Rb}$ and ${}^{87}\text{Rb}$ is also implemented in the vacuum chamber of the experiment. All measurements described throughout this thesis are performed with ${}^6\text{Li}$ because we decide to focus on one isotope as long as we are working on the initial setup of the experiment.

We choose to work with lithium atoms for several reasons. Lithium is the lightest of the alkali metals which are the most suitable class of atoms for laser cooling and trapping due to their relatively simple level structure. In appendix A we show the energy levels of ${}^6\text{Li}$, which are relevant for the laser cooling techniques that we use, and in appendix B the magnetic field dependence of these states is displayed. The intrinsic timescale of atoms in an optical lattice is the recoil energy E_r which is $E_r = h^2/8ma^2$ for a square lattice, with m being the mass of the atom, a being the spacing of the lattice and h being the Planck constant. Hence the recoil energy scales as $1/(ma^2)$. This means that larger lattice spacings, which are more easy to resolve in a quantum gas microscope, can be used in combination with an atom with a light mass. In addition, the timescales of the system are faster for an atom with a

light mass, for example the dynamics of ${}^6\text{Li}$ are more than 6 times faster than the dynamics of the only other fermionic alkali atom ${}^{40}\text{K}$ that can be used in cold atom experiments.

Another advantage of working with lithium atoms are the broad Feshbach resonances of both isotopes [15]. While bosonic atoms suffer from three-body losses near a Feshbach resonance, Fermi mixtures have long lifetimes even at very high scattering lengths due to the Pauli exclusion principle. However, for both isotopes the Feshbach resonance enables precise adjustment of the interaction strength between the atoms to improve the efficiency of evaporative cooling. In addition Feshbach resonances can be used to explore the physics of the BEC-BCS crossover in fermionic systems [13]. In appendix C we show the Feshbach resonances of ${}^6\text{Li}$ that are important for us.

Besides its advantages many challenges come along with the task of on the one hand creating an ultracold quantum gas with lithium atoms and on the other hand imaging this ultracold gas with a quantum gas microscope. These challenges are discussed throughout this thesis as we describe the setup and the functionality of our experiment. More information on the properties of bosonic and fermionic lithium atoms can be found for example in [20, 21].

2.2 Quantum gas microscopy

In this section we motivate why we want our experiment to be a quantum gas microscope. After a general introduction to quantum gas microscopes we focus on three of their central elements: the high-resolution microscope objective, the deep optical pinning lattice and the mechanisms that can be applied to cool the atoms in these lattices. The vertical lattice in our experiment is an accordion lattice and the horizontal lattice is a triangular lattice. The cooling mechanism that we aspire to implement is Raman sideband cooling. Therefore, we dedicate an extra section to each of these topics to explain them in more detail.

2.2.1 A short introduction to quantum gas microscopes

In the field of research of ultracold quantum gases, quantum gas microscopes have emerged as an extremely powerful tool in the last decade. In most quantum gas experiments absorption images are taken to observe the real space or momentum space distribution of an atomic cloud. Even though, many interesting experiments have been and continue to be carried out in this way they do not advance to the single-particle level because the sensitivity of this imaging technique is too low to be able to resolve individual atoms. However the individual constituents and especially the correlations between them in the case of interacting systems are essential to understand the physics that is happening in such systems.

Quantum gas microscopes overcome this limit because they can detect individual atoms on different sites of an optical lattice. The spacing of the lattice can be chosen

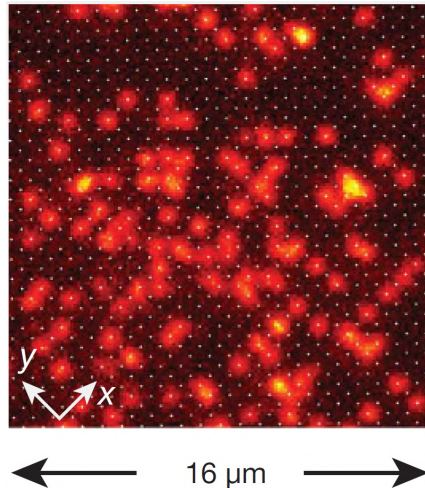


FIGURE 2.1: Fluorescence image of individual ^{87}Rb atoms in a sparsely filled square lattice. Image taken from [17].

such that the tunneling rate of the atoms is high enough to consider the system to be interacting and at the same time individual lattice sites can still be resolved. In figure 2.1 an image from [17] is shown where a square lattice was sparsely filled with ^{87}Rb atoms. Here it is nearly possible to determine with the naked eye whether a lattice site is occupied with an atom or not. Using a quantum gas microscope different quantum states of a system of ultracold atoms can be observed on the single-particle level. In addition charge and spin correlations become accessible by averaging many experimental iterations of the same system.

The first quantum gas microscopes with bosonic ^{87}Rb have been realized at the beginning of the last decade [16, 17]. Later on the bosonic side two microscopes working with ^{174}Yb followed [22, 23]. Since 2015 six groups have presented quantum gas microscopy of fermionic atoms, three working with ^{40}K [24–26] and the other three working with ^6Li [27–29]. First experiments with quantum gas microscopes have looked at the different quantum phases of atoms in an optical lattice. They have been used to study the superfluid to Mott insulator transition of bosonic atoms [17, 30, 31] and the metal to band insulator to Mott insulator transition of fermionic atoms [28, 32, 33] on the single-particle level. Among many other interesting physical systems quantum gas microscopes have been very successful in the analysis of correlation functions and quantum magnetism [29, 34–51]. Besides the success of quantum gas microscopes it should be mentioned that spin-resolved single-atom imaging of fermionic ^6Li atoms has also been realized in free space in 2018 [52].

2.2.2 High-resolution microscope objective

The central element of a quantum gas microscope is a high-resolution objective. The numerical aperture (NA) of the objective sets the limit for the achievable optical resolution. Among several existing conventions the Rayleigh criterion is the one that is most often used in the cold atoms community. It defines the minimum distance d_{min}

between two objects such that they can still be resolved as

$$d_{min} = \frac{0.61 \lambda}{NA} \quad , \quad (2.1)$$

with λ being the wavelength of the imaging light. The range of NAs used in quantum gas microscopes starts at 0.5 and goes up to effective values of 0.87 by minimizing the distance between the atoms and the objective as much as technically possible and by adding a hemispherical immersion lens [16, 25, 27]. To build an objective that enables nearly diffraction-limited imaging becomes technically very challenging with increasing NA. Hence the objective for a quantum gas microscope typically is a custom-made product of a specialized company. The lenses of the objective have an anti-reflective (AR) coating, especially for the imaging light to avoid loss of signal but often also for other laser wavelengths that pass through the objective. Depending on the NA, the imaging wavelength, the lattice wavelength and the lattice geometry the resulting theoretical resolution of the imaging system is above or below the lattice constant which is the size that needs to be resolved. The finite signal-to-noise ratio in the actual experiment usually prohibits the direct distinction between occupied and unoccupied lattice sites, especially for highly occupied lattices. Therefore reconstruction algorithms are employed to realize a reconstruction fidelity that is at least better than 95%. Moreover the number of atoms on a lattice site undergoes a parity projection during the imaging process because two atoms get lost pairwise due to light-assisted collisions. In consequence an even number of atoms on a lattice site appears as an empty lattice in the final image and an odd number of atoms on a lattice site appears as a single atom.

2.2.3 Optical pinning lattices

Even though, the objectives in quantum gas microscopes have high NAs they still can collect only a small proportion of the fluorescence light which is scattered isotropically by the atoms. An objective with a NA of 0.5 for example has a collection efficiency of only 6.7%. Hence it is necessary to hold the atoms as long as possible in the optical lattice on the same lattice site such that they scatter enough photons to be resolved. One ingredient to realize this are very deep optical lattices to pin the atoms on their respective lattice site. Hence, these lattices are called pinning lattices. The common measure to describe how strongly atoms are pinned to one site is the recoil energy E_r of the lattice:

$$E_r = \frac{\hbar^2 k_L^2}{2m} \quad , \quad (2.2)$$

with $k_L = 2\pi/\lambda_L$ being the wavenumber of the lattice laser, m being the mass of the atom that is trapped in the lattice and \hbar being the reduced Planck constant. We directly see that for otherwise same lattice parameters an optical lattice is deeper

in terms of the recoil energy for a light atom like ${}^6\text{Li}$ than for a heavier atom like fermionic ${}^{40}\text{K}$ or bosonic ${}^{87}\text{Rb}$. Hence, it is more difficult to create sufficiently deep lattices for a quantum gas microscope with ${}^6\text{Li}$ and significant effort has already been invested to realize very deep lattices [53, 54].

An objective with a high NA unavoidably has a small depth of focus. Hence the objective can only be focused to a single plane of the optical lattice along its axis. Simultaneous focusing of several lattice planes would be a problem anyway because the signal of atoms on adjacent planes of the vertical lattice would overlap and in this way hinder the reconstruction of individual atoms [55, 56]. The necessity to precisely focus the objective to a single plane of atoms usually restricts the physics, that can be studied with a quantum gas microscope, to one-dimensional (1D) and two-dimensional (2D) systems. The physics of three-dimensional (3D) systems might begin to become accessible by subsequent imaging of several lattice planes [57–59]. Even though, the physics of ultracold atoms in optical lattices continues to be one of the most fruitful branches of research in the quantum gases community, in the special case of quantum gas microscopes optical lattices are a priori a part of the detection setup and not necessarily an ingredient of the physical system that shall be studied. This is especially true for the vertical lattice which is used to freeze out the motion of the atoms along the axis of the objective. The vertical lattice can also be used to prepare the 2D sample with only a single layer of atoms along the vertical direction. This can be done with a so-called accordion lattice [60] which we choose for our experiment and which is described in section 2.2.4. Other ways to create 2D samples are very elliptical dipole traps, so-called light sheets, RF sweeps in combination with magnetic field gradients or combinations of these methods.

Many quantum gas microscopes use a square lattice as their horizontal pinning lattice [16, 17, 27, 28]. By creating a square lattice with a single retro-reflected beam 4-fold interference of this beam is realized which additionally increases the depth of the lattice [29]. For our experiment we want to use a triangular lattice as the pinning lattice which has been used just very recently in a new quantum gas microscope for bosonic ${}^{87}\text{Rb}$ atoms [61] and which we discuss in section 2.2.5. In many experiments the horizontal pinning lattice is also used as the physics lattice [17, 30, 32, 33]. There the atoms are first loaded into more shallow lattices to be in the regime where atoms have a significant probability to tunnel to other lattice sites. At the beginning of the imaging process the lattice depth is ramped up rapidly to freeze the atoms at their current position. However it is also possible to use two different lattices at the same experiment, for example one as the physics lattice and the other one as the pinning lattice [28]. Another possibility that has been implemented is a superlattice along one horizontal direction to realize spin-resolved imaging of 1D chains [43].

Most experiments with quantum gas microscopes up to now have focused on the physics of ultracold atoms in optical lattices but it is also possible to use them as a tool for single-atom resolved imaging of bulk physics [62]. In our experiment we want to use the technique of quantum gas microscopy to look at systems that

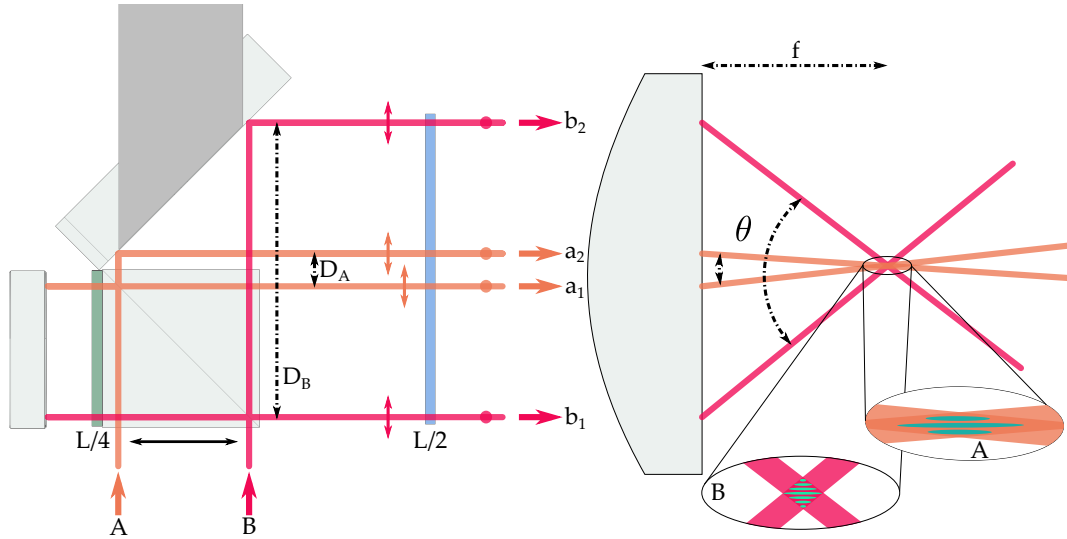


FIGURE 2.2: Working principle of the accordion lattice. The entrance point of the initial lattice beam on the cube determines the resulting lattice spacing. Path A (orange) results in a small distance between the beams, hence a small crossing angle and ultimately in a large lattice spacing. In contrast path b (purple) leads to large beam distance, a large crossing angle and therefore a small lattice spacing. Figure taken from [18].

contain only a small number of atoms. Here a small number means a maximum of ~ 10 atoms. In this regime it is necessary to deterministically prepare a specific number of atoms. This has been successfully demonstrated with fermionic ${}^6\text{Li}$ atoms by tilting a very small dimple trap with a magnetic field gradient, first in 1D [63] and recently also in 2D [64]. We mention some of the physical systems that we want to study in the outlook of this thesis (see chapter 7).

To use this technique in a quantum gas microscope we have to be able to apply a magnetic gradient after the preparation of the 2D sample. This gradient can not be created along the vertical direction because it would lead to the population of adjacent lattice planes. Hence, we have to create a magnetic field gradient along a horizontal direction which is important to consider during the design of the magnetic field coils (see chapter 4). A magnetic gradient along a horizontal direction is useful anyway because every method to create a 2D sample heats up the atomic cloud. Therefore, an additional evaporative cooling of the 2D sample is probably necessary to get back into the quantum degenerate regime [65, 66]. For such an evaporation step the magnetic field gradient along a horizontal direction can be crucial because evaporating by only lowering the power of the vertical lattice again has the risk of populating adjacent lattice planes.

2.2.4 Accordion lattice

An accordion lattice enables loading of a single lattice plane and subsequent squeezing of the lattice to bring the sample into the 2D regime. The working principle of the accordion lattice is displayed in figure 2.2. The incoming lattice laser beam is split into two beams of equal power using a polarizing beamsplitter (PBS) cube. The

resulting distance D between the two beams depends on the point where the initial laser beam enters the cube. The two resulting beams are focused by a lens with a focal length f and hence intersect in the focal plane of the lens if both beams hit the lens with no incident angle. The crossing angle θ of the beams behind the lens depends on their distance D in front of the lens via

$$\tan(\theta/2) = \frac{D}{2f} . \quad (2.3)$$

In the intersection area of the two coherent laser beams there is a lattice structure along the vertical direction. The spacing of this lattice a_{acc} depends on the crossing angle θ of the two beams via

$$a_{acc} = \frac{\lambda_L}{2 \sin(\theta/2)} , \quad (2.4)$$

with λ_L being the wavelength of the lattice laser. By combining the two equations we get the dependence between the lattice spacing a_{acc} and the distance D between the two beams in front of the lens:

$$a_{acc} = \frac{\lambda_L}{2} \sqrt{1 + 4 \left(\frac{f}{D}\right)^2} . \quad (2.5)$$

In consequence we can dynamically tune the spacing of the lattice by moving the position of the incoming laser beam on the cube. This is realized with a mirror that is mounted on a motorized translation stage (see section 3.4). Different combinations of optics can be used to create an accordion lattice [60, 67, 68]. We use a combination of one PBS and two mirrors as it is shown in figure 2.2 to enable independent adjustment of both lattice beams. A quarter-wave plate (QWP) is coated on one side of the cube to assure transmission of the respective laser beam when it re-enters the cube. A rectangular half-wave plate (HWP) between the cube and the lens assures full modulation of the interference pattern for all crossing angles of the beams.

2.2.5 Triangular lattice

A triangular lattice has been used only very recently as the horizontal pinning lattice in a quantum gas microscope [61] but triangular lattices and other 2D lattice structures from the family of hexagonal lattices have already enabled a long list of interesting experiments. To name only a small selection triangular lattices have for example been used for the simulation of classical [69, 70] and quantum magnetism [71]. Another interesting hexagonal lattice is the so-called honeycomb lattice which has a two-site basis [72, 73]. In this system Floquet engineering can be applied by using time-periodic lattice shaking to engineer topological quantum matter [74, 75]. We decide to use a triangular lattice as the pinning lattice for our experiment for reasons that are explained in this section but it also enables us to combine the rich physics

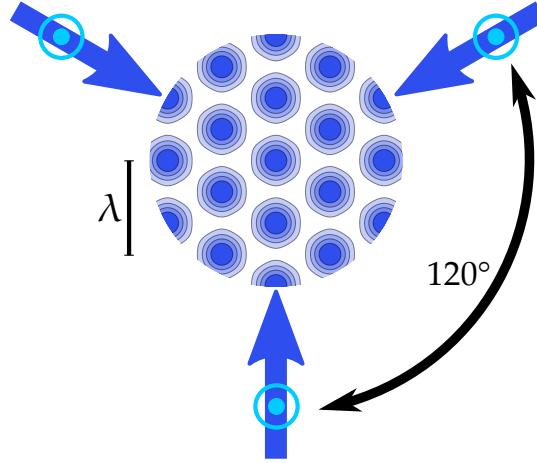


FIGURE 2.3: Setup and interference pattern of a triangular lattice. Three laser whose polarization is out of plane (*s*-polarization) interfere with an angle of 120° between each pair of lattice beams. Every lattice site has 6 nearest neighbors with a lattice spacing of $2\lambda_L/3$. Figure adapted from [18].

of hexagonal lattice structures with the single-atom and single-site sensitivity of a quantum gas microscope.

We now discuss some basics of the triangular lattice. An introduction to hexagonal optical lattices can for example be found in [76–78]. Hexagonal lattices are created by three interfering laser beams with an angle of 120° between each pair of beams (see figure 2.3). Hence the wavevectors of the three beams can be written as

$$\mathbf{k}_1 = k_L \begin{pmatrix} 0 \\ 1 \end{pmatrix}, \quad \mathbf{k}_2 = \frac{k_L}{2} \begin{pmatrix} \sqrt{3} \\ -1 \end{pmatrix}, \quad \mathbf{k}_3 = \frac{k_L}{2} \begin{pmatrix} -\sqrt{3} \\ -1 \end{pmatrix}, \quad k_L = \frac{2\pi}{\lambda_L}, \quad (2.6)$$

with k_L being the wavenumber and λ_L being the wavelength of the lattice laser. If the polarization of all three lattice beams is out of plane (*s*-polarization) the resulting potential

$$V_\Delta(\mathbf{r}) = -V_0 \left[\frac{3}{4} + \frac{1}{2} (\cos[(\mathbf{b}_1 - \mathbf{b}_2)\mathbf{r} - \phi_2] + \cos[\mathbf{b}_1\mathbf{r} - \phi_3] + \cos[\mathbf{b}_2\mathbf{r} + \phi_2 - \phi_3]) \right] \quad (2.7)$$

is called a triangular lattice. Here V_0 is the lattice depth, \mathbf{b}_i are the primitive reciprocal lattice vectors and ϕ_i are the phases of the lattice laser beams. ϕ_1 is set to zero without loss of generality because the structure of the lattice is uniquely defined by the phases of two beams. Hence phase fluctuations lead to a global movement of the respective lattice structure. From the wavevectors we can calculate the primitive

reciprocal lattice vectors:

$$\begin{aligned} \mathbf{b}_1 = \mathbf{k}_2 - \mathbf{k}_3 &= b \begin{pmatrix} 1 \\ 0 \end{pmatrix} , & \mathbf{b}_2 = \mathbf{k}_1 - \mathbf{k}_3 &= \frac{b}{2} \begin{pmatrix} 1 \\ \sqrt{3} \end{pmatrix} , \\ \mathbf{b}_3 = \mathbf{k}_1 - \mathbf{k}_2 &= \frac{b}{2} \begin{pmatrix} -1 \\ \sqrt{3} \end{pmatrix} , & b &= \sqrt{3}k_L . \end{aligned} \quad (2.8)$$

Two reciprocal lattice vectors are sufficient to span the reciprocal lattice in momentum space:

$$\mathcal{R} = \{ \mathbf{R} | \mathbf{R} = m_1 \mathbf{a}_i + m_2 \mathbf{a}_j, m_k \in \mathbb{Z}, i \neq j \} . \quad (2.9)$$

The primitive lattice vectors can be written as

$$\mathbf{a}_1 = \frac{a}{2} \begin{pmatrix} \sqrt{3} \\ -1 \end{pmatrix} , \quad \mathbf{a}_2 = a \begin{pmatrix} 0 \\ 1 \end{pmatrix} , \quad \mathbf{a}_3 = \frac{a}{2} \begin{pmatrix} \sqrt{3} \\ 1 \end{pmatrix} , \quad a = \frac{2}{3} \lambda_L . \quad (2.10)$$

Two of the primitive lattice vectors span the Bravais lattice in position space:

$$\mathcal{G} = \{ \mathbf{G} | \mathbf{G} = n_1 \mathbf{b}_i + n_2 \mathbf{b}_j, n_k \in \mathbb{Z}, i \neq j \} . \quad (2.11)$$

The primitive lattice vectors and the primitive reciprocal lattice vectors are connected via the relations

$$e^{i\mathbf{G}\mathbf{R}} = 1 \quad \text{and accordingly} \quad \mathbf{a}_i \cdot \mathbf{b}_j = 2\pi\delta_{ij} . \quad (2.12)$$

If only two of the three lattice beams are turned on a 1D lattice is created which has the potential:

$$V_{1D}(\mathbf{r}) = -\frac{V_0}{2} \cos [(\mathbf{k}_i - \mathbf{k}_j) \mathbf{r} + \phi_i - \phi_j] . \quad (2.13)$$

The spacing of this 1D lattice can be calculated via

$$a_{1D} = \frac{2\pi}{|\mathbf{k}_i - \mathbf{k}_j|} = \frac{\pi}{|k| \sin(\alpha/2)} , \quad (2.14)$$

with α being the full angle between the two lattice beams.

The spacing of a triangular lattice is $a_\Delta = 2\lambda_L/3$ which means that it is a factor of 4/3 larger than the spacing of a square lattice $a_\square = \lambda_L/2$. In [29] a square lattice with a lattice spacing of $a_\diamond = \lambda_L/\sqrt{2}$ is created by the 4-fold interference of a single laser beam. The larger lattice spacing of the triangular lattice compared to the square lattice is easier to resolve with a quantum gas microscope. In addition the interference factor in next-neighbor direction is 8/9 for a triangular lattice instead of 1/2 for the normal square lattice.

2.2.6 Cooling mechanisms for atoms in an optical lattice

Atoms must be excited to a higher internal state to be able to send out fluorescence light which can then be collected for imaging purposes. The excitation needs to be done with resonant or near-resonant laser light and the photon recoil during absorption and emission unavoidably heats up the atoms in the lattice. Even though the atoms are pinned in very deep lattices during the imaging process it is not sufficient to achieve single-atom and single-site resolution for the most atomic species that have been used in quantum gas microscopes up to now. Hence, a cooling mechanism needs to be implemented such that the atoms scatter enough photons without tunneling to other lattice sites. Only for heavy bosonic ^{174}Yb atoms quantum gas microscopy without a cooling mechanism has been demonstrated [22, 31].

For bosonic ^{87}Rb the sub-Doppler cooling mechanism of polarization-gradient cooling turned out to be sufficient for cooling the atoms in the lattice during the imaging process [16, 17]. The fluorescence of the atoms is automatically created in this cooling mechanism. Polarization-gradient cooling works much worse for the fermionic isotopes ^6Li and ^{40}K because the respective hyperfine structure of the excited $^2P_{3/2}$ state is too narrow. For the initial laser cooling of the atoms gray molasses cooling has been implemented as an alternative sub-Doppler cooling mechanism for many atomic isotopes [79–92]. For cooling the atoms in the optical lattice all existing quantum gas microscopes with ^6Li have implemented Raman sideband cooling [27–29]. Among the microscopes working with ^{40}K one applies Raman sideband cooling [25] and the other two work with electromagnetically-induced transparency (EIT) cooling [24, 26]. The combination of very deep pinning lattices with the implementation of alternative cooling mechanisms has enabled the realization of fermionic quantum gas microscopes. However, the number of collected photons per atom in fermionic quantum gas microscopes is significantly lower than in the microscopes working with bosonic ^{87}Rb . As our setup is designed to also implement Raman sideband cooling we shortly introduce it in the next section.

2.2.7 Raman sideband cooling

The natural linewidth Γ of all alkali atoms is approximately $2\pi \times 6$ MHz. This is much larger than the on-site trap frequency of even the deepest optical lattices that have been created up to now. Therefore resolved-sideband cooling is usually not possible for ultracold atoms using a single-photon transition. In contrast trapped ions are for example routinely cooled with resolved-sideband cooling [93]. The solution that is used in Raman sideband cooling is a two-photon Raman process that couples two spin states of the atomic ground state which is shown for the example of ^6Li in figure 2.4. The linewidth of the two-photon transition can be very small because no spontaneous decay with a natural linewidth is involved. All quantum gas microscopes working with ^6Li operate their Raman lasers with a red-detuning of 5 to 8 GHz [27–29] to the $2^2P_{1/2}$ excited state to minimize residual single-photon

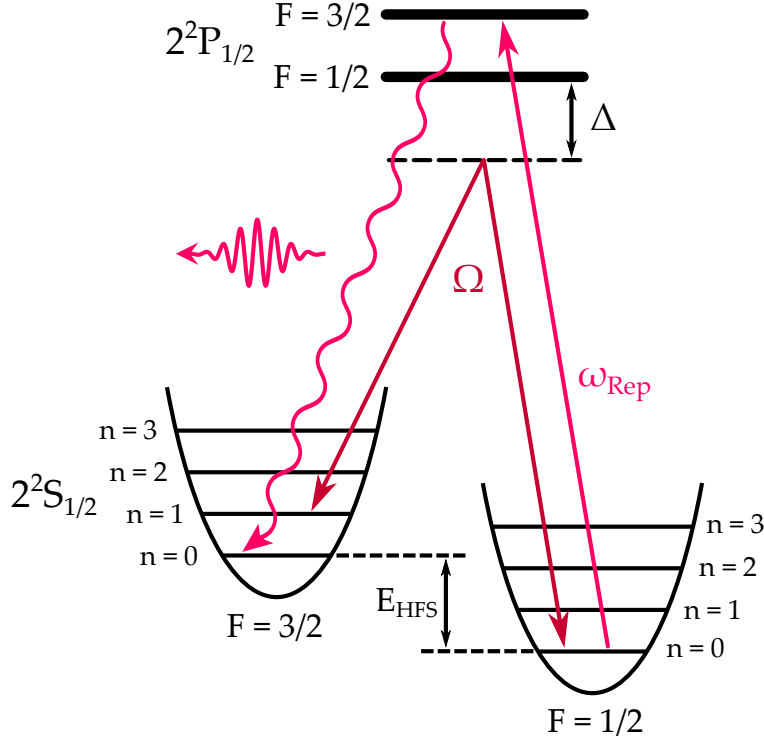


FIGURE 2.4: Principle of Raman sideband cooling for ${}^6\text{Li}$. The scheme is adapted from [21] but a similar scheme is used in all existing quantum gas microscopes that are working with ${}^6\text{Li}$ [27–29]. A coherent two-photon Raman process with Rabi frequency Ω brings the atoms from the $F = 1/2$ to the $F = 3/2$ hyperfine state of the $2^2S_{1/2}$ ground state while reducing the harmonic oscillator level of the atoms by one. Typical red-detunings Δ of the two Raman beams to the excited $2^2P_{1/2}$ state are in the range of 5 to 8 GHz. An additional beam at ω_{Rep} pumps the atoms back into their initial spin state. The emitted fluorescence light can be collected for imaging purposes in a quantum gas microscope.

excitations.

A two-photon transition that does not change the harmonic oscillator level of the atom is called the carrier transition and a two-photon transition that changes it is called a sideband transition. For Raman sideband cooling the two-photon detuning is typically adjusted such that the harmonic oscillator level of the atom is reduced by one oscillator quantum which corresponds to an energy of $\hbar\omega_0$, with ω_0 being the on-site trap frequency of the optical lattice. The two-photon transition is a coherent process and therefore leads to an oscillation of the atoms between the two coupled states with a Rabi frequency Ω . A repumper beam with frequency ω_{Rep} optically pumps the atoms back into their initial spin state. In the existing ${}^6\text{Li}$ quantum gas microscopes the repumper is either a bit blue-detuned ($\sim +3\Gamma$ [27, 28]) to the $F = 3/2$ hyperfine state of the $2^2P_{1/2}$ level or it is slightly red-detuned ($\sim -10\Gamma$ [68]) to the $F = 1/2$ hyperfine state of the same level. The incoherent repump process preserves the harmonic oscillator level if the Lamb-Dicke parameter η is much smaller than one:

$$\eta = \frac{E_r}{\hbar\omega_0} \ll 1 \quad , \quad (2.15)$$

with E_r being the recoil energy of a repumper photon and $\hbar\omega_0$ again being the on-site trap frequency of the optical lattice. This means that the recoil energy of a repumper photon has to be much smaller than the trap frequency. In consequence the atom ends up in its initial spin state but it loses one oscillator level and is cooled in this way.

Due to the continuous repetition of this process the atom can be cooled into the ground state of the optical lattice using Raman sideband cooling. This is for example used in experiments with optical tweezers [94]. For quantum gas microscopy Raman sideband cooling automatically provides fluorescence photons for imaging the atoms due to the repumping process while at the same time cooling the atoms such that they do not start to tunnel to other lattice sites.

Raman sideband cooling can be performed in a pulsed sequence, with alternating pulses of the two Raman beams and the repump beam, or continuously with all beams being on the whole time. The advantage of a pulsed sequence for quantum gas microscopy can be that the camera used for imaging or rather its intensifier can be turned off when the Raman beams are on to avoid background signal from the Raman beams [27].

There often is an inhomogeneity in trap frequency between different axes of the pinning lattice or even along one axes over the size of the sample. This leads to a variation of the red sideband transitions which can be addressed in different ways. In [27] a pulsed sequence with 5 μ s long Raman pulses is used. The Fourier broadening of this short pulses exceeds the inhomogeneity of the trap frequencies. In [28] the two-photon detuning is modulated sinusoidally to address on-site trap frequencies between 900 kHz and 1.3 MHz. Finally in [29] the trap-frequency in the x-y plane is 1.5 MHz and along the z-direction there is a confinement of only 70 kHz. Nevertheless they are able to successfully perform Raman sideband cooling. It has not been studied in detail up to now why this configuration also works but one possibility is that the Raman beams effectively couple the weakly confined direction with the strongly confined directions [95]. A very detailed discussion of Raman sideband cooling in the context of a quantum gas microscope with fermionic ${}^6\text{Li}$ can be found in [21].

Chapter 3

Experimental apparatus

In this chapter we provide an introduction to the central ingredients of our experimental apparatus. We begin with the vacuum chamber where the atoms are actually cooled, manipulated and imaged. Next we show the laser systems for the creation of near-resonant light and the setups for the optical dipole traps and lattices. Finally we discuss the setting for the realization of high-resolution imaging.

The design and setup of the experimental apparatus has been a process of several years with many people involved at different stages. In the order of joining the team, this were Klaus Sengstock, Christof Weitenberg, Benno Rem, Andreas Kerkmann, the author, Mathis Fischer, Justus Brüggjenjürgen and Tobias Petersen supported by various Bachelor students and student assistants. Further information on the experimental apparatus can mainly be found in [18, 96–98].

3.1 Vacuum chamber

We begin our discussion of the vacuum chamber with some principal design considerations. Then we show the resulting setup for the creation of the ultrahigh vacuum. The 2D-MOT for lithium atoms is realized in a compact steel chamber and the 3D-MOT and all subsequent experimental steps are performed in a glass cell. Two separate sections are dedicated to these central elements of the experimental setup.

3.1.1 Principal design considerations

The main design goal for our experimental apparatus is to achieve a compact setup enabling short experimental cycles. A short cycle time is essential for creating high statistics in reasonable long times. In addition high statistics are particularly important to analyze small quantum systems as we plan to do. The first cooling stage in our experiment is a two-dimensional magneto-optical trap (2D-MOT). A 2D-MOT has been used in the cold atom community for different atomic species in many experiments but experiments with lithium atoms have mostly used a Zeeman slower. It was shown for the first time in [99] that also for lithium atoms a loading rate for the three-dimensional magneto-optical trap (3D-MOT) can be achieved with a 2D-MOT that is similar to the loading rate if a Zeeman slower is used.

A Zeeman slower occupies a lot of space compared to a 2D-MOT. In addition we

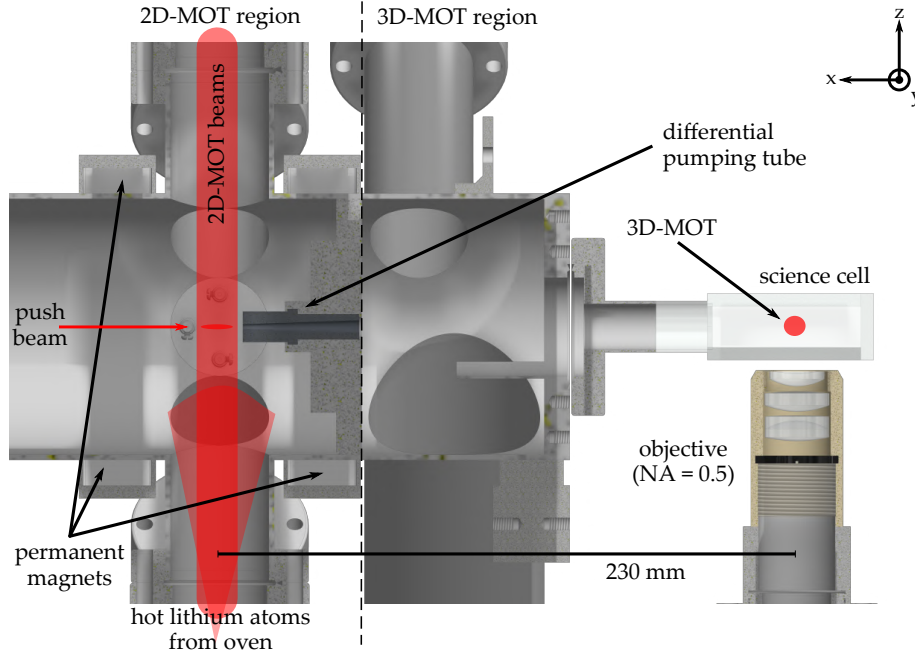


FIGURE 3.1: Vacuum chamber and science cell shown in a vertical cut along the axis of the push beam which supports the transfer of lithium atoms from the 2D-MOT to the 3D-MOT through the differential pumping tube. In addition the high resolution objective underneath the glass cell is displayed. Figure adapted from [18].

have no transport after the 3D-MOT to make the setup even more compact. In consequence all experimental steps beginning with the 3D-MOT take place at the same position. This does not only save a lot of space and material including additional vacuum components, magnetic field coils and lasers, but it also avoids particle losses and heating of the sample due to the transport of the atomic cloud. The drawback of such a compact design is that the space for all the things, that have to be placed around the vacuum chamber, is very limited. We discuss the resulting difficulties and our solutions for them in the respective sections of this thesis.

Our approach is to use a glass cell instead of a steel chamber to strive for site-resolved imaging of individual atoms in a deep optical lattice. Therefore, the 3D-MOT in our setup is already realized in the glass cell which would not be possible with a Zeeman slower because in this case the atomic beam coming out of the oven would be on the same axis as the loading axis of the MOT. Hence, the atomic beam of the Zeeman slower would need to be dumped in the glass cell and the lithium atoms would coat the inner surfaces of the cell. This would be a big problem because lithium sticks irreversibly on glass surfaces [100]. In consequence the glass cell and also all viewports of the steel chamber must be protected carefully against coating with hot lithium atoms.

3.1.2 Vacuum setup

Due to the very high chemical reactivity of lithium the 2D-MOT is realized in a compact steel chamber in contrast to the glass cell of the 3D-MOT. The line of sight of the

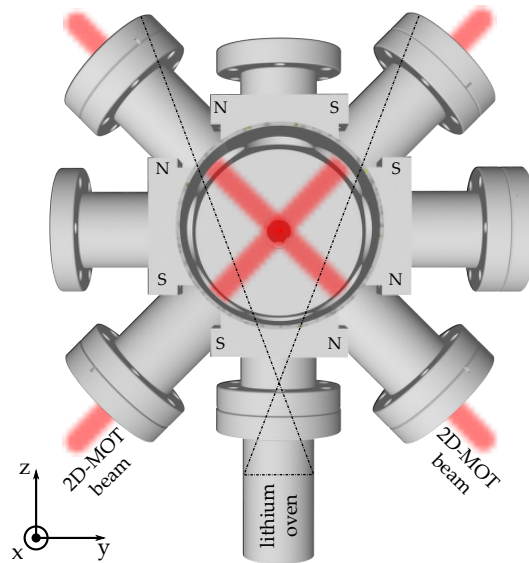


FIGURE 3.2: View into the 2D-MOT steel chamber through the viewport that is the entrance for the push beam. The black dotted line marks the line of sight of the atomic flux from the oven and hence the maximum possible filling of the oven. The 2D-MOT beams and the orientation of the permanent magnets are also shown. Figure adapted from [18].

lithium oven is perpendicular to the loading axis of the 3D-MOT (see figure 3.1). The distance between the positions of the 2D-MOT and the 3D-MOT is as small as possible (230 mm) to get efficient loading of the 3D-MOT. An additional push beam significantly enhances the loading rate from the 2D-MOT into the 3D-MOT. The 2D-MOT steel chamber and the 3D-MOT glass cell are connected via a differential pumping tube made out of graphite which is a good getter material for alkaline metals [101]. The pumping tube can keep up a pressure difference between the two areas of at least a factor 100. Hence we can realize a vacuum of $< 2 \times 10^{-11}$ mbar in the glass cell even if the pressure in the steel chamber rises into the 10^{-9} mbar regime because of the oven being heated up. Both areas have their own turbo pumps, ion getter pumps and gauges. The turbo pumps are only turned on during the initial evacuation of the chamber and the glass cell. The vibrationless ion getter pumps are always turned on to keep up the vacuum. The route to our working conditions, when we built up the chamber and evacuated it, is described in detail in the PhD thesis of Andreas Kerkmann [18].

3.1.3 Steel chamber

The beams for the 2D-MOT are sent into the steel chamber through viewports and subsequently they are retro-reflected. Their axis is shifted $\pm 45^\circ$ to the vertical z-axis and they are shaped elliptically (see figure 3.2). A magnetic gradient field of approximately 50 G/cm that is needed for the 2D-MOT is created using stacks of permanent magnets¹ which are attached to the steel chamber. 8 stacks in two groups of 4 stacks

¹Eclipse Magnetics: N750-RB

are placed according to [102] creating two overlapping octupole fields. Due to the short distance between the positions of the 2D-MOT and the 3D-MOT the permanent magnets of the 2D-MOT create a residual magnetic field at the position of the 3D-MOT which can not be turned off and which can also not be compensated completely due to the specific form of the field that is created by the two octupoles [98]. Lithium is a solid at room temperature and has a significant vapor pressure only at rather high temperatures. We therefore need an oven as our atom source which is connected via a flange at the bottom of the steel chamber and which emits hot lithium atoms along the z-axis. The oven is custom made by the company Pfeiffer Vacuum but has a rather simple design. It is a cup with a length of 83 mm and a diameter of 40 mm. No apertures for controlling the atomic flux of the oven are installed because we want to avoid that these apertures get stuck with lithium such that we would have to exchange the oven.

The oven is heated with heating wires and isolated with several layers of glass wool and aluminum foil. We monitor the temperature at several objects close to the oven because there is heat transport from the oven to the rest of the steel chamber and we want to avoid too much thermal drifting in the experiment or even damage to other components due to this heating by the oven. The permanent magnets of the 2D-MOT for example start to lose their magnetization when being heating above 100 °C. For safety reasons we therefore limit the maximum temperature of the oven to 470 °C but usually we operate it around 420 °C for sufficient flux of atoms.

The oven can not be filled completely with solid lithium because then its line of sight would hit the viewports of the 2D-MOT beams and the lithium would coat the viewports. We initially filled the oven with 3 g of a 50:50 mixture of fermionic ${}^6\text{Li}$ and bosonic ${}^7\text{Li}$ in March 2016 to be able to work with both isotopes. This lasted for three years but we had continuous struggle with the performance of the oven in the second half of this period. We had to open the vacuum chamber in March 2019 to refill the oven. This time we filled the oven with 20 g of the 50:50 lithium isotope mixture.

In addition to the lithium oven we also install a source for rubidium atoms in our steel chamber. Rubidium has a much higher vapor pressure at room temperature compared to lithium. Therefore, dispensers that are activated with electrical current create a directed high atomic flux without the need for high temperatures. The rubidium dispensers enable us to also work with ${}^{85}\text{Rb}$ or ${}^{87}\text{Rb}$ even though ${}^{87}\text{Rb}$ has been the more convenient choice for most experiments that work with ultracold rubidium atoms. In addition we could in principle work with different mixtures of the two lithium isotopes and the two rubidium isotopes. This is important to know for the design of the magnetic field coils (see section 4.2.1).

3.1.4 Science cell

The science cell is the place where all experimental steps after the 2D-MOT take place. Therefore, there are many demands on the properties of this glass cell and

TABLE 3.1: All wavelengths that the science cell has an AR coating for are listed together with the corresponding transmissions at incident angles of 0° and 28° . The relevance of the wavelengths for the experiment is also mentioned. Data taken from [98] where the measurement to characterize the coating is described. The measurement setup limited the accessible incident angles to values $< 30^\circ$.

λ_L (nm)	T(0°) (%)	T(28°) (%)	Relevance for the experiment
323	70.9	75.3	$2s \rightarrow 3p$ transition of ${}^6\text{Li}$
532	94.4	95.5	Repulsive dipole traps / Optical lattices
671	97.7	98.7	D1 and D2 line of ${}^6\text{Li}$ and ${}^7\text{Li}$
780	97.3	98.2	D1 and D2 line of ${}^{85}\text{Rb}$ and ${}^{87}\text{Rb}$
813	97.5	99.3	$2p \rightarrow 3s$ transition of ${}^6\text{Li}$
1064	98.1	98.0	Attractive dipole traps / Optical lattices
1070	98.0	98.0	Attractive dipole traps / Optical lattices

some compromises have to be made. The outer measurements of our glass cell² are $65 \text{ mm} \times 26 \text{ mm} \times 26 \text{ mm}$ and the walls of the cell have a thickness of 5 mm. These numbers are a trade-off between the numerical aperture (NA) and the size of the 3D-MOT beams. On the one hand a smaller length of the cell along the axis of the objective enables a higher NA. This results in a better resolution for site-resolved imaging because the microscope objective can be placed closer to the atoms. But on the other hand the 3D-MOT beams should not undercut a minimum size to make sure that enough particles can be trapped in the 3D-MOT which are needed for the subsequent experimental steps.

The objective has a working distance of 19 mm and is corrected for the transmission through one wall of the science cell. As a rule of thumb the surface flatness of the glass cell wall needs to be $< \lambda/4$ with λ being the wavelength of the imaging light to achieve nearly diffraction-limited imaging using the objective. We check the surface flatness of the four long cell walls to be sufficient using an interferometer before we install the glass cell [97]. After evacuation of the cell we repeat this measurement to check for additional bending of the cell walls due to the pressure difference arising from the vacuum inside the cell. We do not see significant bending and hence are optimistic that the thickness of the cell walls has been a good choice for our experiment.

A special feature of this glass cell is that the walls have a custom-made AR coating on both sides. A good AR coating is important to avoid reflections that lead to unwanted interference effects and to minimize the loss of laser power when the light is passing through the cell walls. The technique to coat both sides of the cell walls limits the choice of glass to a borosilicate glass³. This comes along with stronger thermal

²ColdQuanta: custom design product

³Schott: Borofloat 33

lensing effects compared to fused silica when it is subjected to high laser power. The wavelengths, for which the science cell is AR coated, the particular transmissions which were measured in [98] and the respective relevance for the experiment are listed in table 3.1.

The big magnetic field coils around the science cell, which are used for the 3D-MOT and for all further experimental steps, as well as the offset coils for compensation of magnetic stray fields are discussed in detail in chapter 4. The laser systems that create the light for the MOT, absorption and fluorescence imaging, optical dipole traps and optical lattices are discussed in the following sections of this chapter.

3.2 Laser system for near-resonant light

The laser system that we use for the 2D-MOT, 3D-MOT, gray molasses and low- and high-field imaging has initially been developed and built by Andreas Kerkmann in his master's thesis [98]. Since then it has continuously been improved and advanced further. A current status of these parts of the laser system is documented in more detail in the PhD thesis of Andreas Kerkmann [18]. For completeness their main features are mentioned in section 3.2.1 and 3.2.2. The part of the laser system for Raman sideband cooling, which has been developed more recently, is discussed in detail in section 3.2.3.

3.2.1 2D-/3D-MOT and gray molasses

The main source of resonant laser light is an external cavity diode laser (ECDL) with an integrated amplifier⁴. The light of this laser is used for the 2D-MOT, the 3D-MOT, the push beam and low field imaging of the upper hyperfine state of the lithium ground state. Hence we call this laser D2 laser because he drives transitions on the D2 line of lithium (see appendix A). The laser light for the 2D-MOT and the 3D-MOT is again amplified with a tapered amplifier⁵ (TA) before it gets distributed to the different MOT axes and coupled into 10 m long polarization-maintaining (PM) fibers⁶. The source of the laser light for the gray molasses also is an ECDL⁷ which is named D1 laser because gray molasses for lithium atoms is performed on the D1 line. The light for the gray molasses is overlapped with the light for the 3D-MOT in front of the corresponding TA using a non-polarizing 50:50 beamsplitter. The repumpers for the 2D-MOT, the 3D-MOT and the gray-molasses are created with a phase-modulating electro-optic modulator (EOM) which creates two frequency sidebands on the laser light. The laser power in one sideband becomes the repumper but the laser power in the other sideband is lost. Nevertheless, using an EOM to generate the repumper

⁴Toptica Photonics: TA pro

⁵Toptica Photonics: BoosTA

⁶Thorlabs: P3-630PM-FC-10

⁷Toptica Photonics: DL pro

saves a lot of space and money compared to using an additional laser for the repumper. In addition the EOM automatically provides phase coherence between the cooler and the repumper which is crucial for the Λ -enhanced gray molasses cooling on the D1 line.

Both lasers are sent into a vapor cell filled with lithium to perform saturated absorption spectroscopy and lock the lasers on the respective atomic transitions. The laser system is designed such that experiments with both lithium isotopes, fermionic ${}^6\text{Li}$ and bosonic ${}^7\text{Li}$, can be performed. For switching from ${}^6\text{Li}$ to ${}^7\text{Li}$ a double-pass acousto-optic modulator (DPAOM) in the D2 spectroscopy has to be turned on and a DPAOM in the D1 spectroscopy has to be turned off. Then the lasers need to be locked on the respective absorption lines for ${}^7\text{Li}$. In addition other EOMs are needed for the creation of the repumpers because of the different ground state hyperfine splitting of the two lithium isotopes.

An important part of a laser system is the ability to precisely switch laser beams on and off. Switching off a beam usually includes two steps. The first step is to set the rf-power that is sent into the corresponding single-pass acousto-optic modulator (SPAOM) to zero by either using a RF-switch or via a command of the experimental control to the digital AOM drivers (see the PhD thesis of Andreas Kerkmann for details on the experimental control and the digital AOM drivers that we use [18]). In general this is a fast and reliable way to switch off a laser beam.

The second step is to move a motorized shutter in front of the corresponding fiber of the beam on the optical table where the resonant laser light is prepared. In this way all residual light that still could get into the fiber is blocked. This residual light may result from non-perfect attenuation of the rf-power in the AOMs or from stray light on the optical table that is accidentally hitting the fiber.

In many cases turning off the rf-power in the AOM is sufficient to switch off a laser beam but for ultracold atomic clouds and single-atom sensitive imaging residual resonant or near-resonant light can be a significant disturbance. In such a case it can be necessary to also block the residual light with very precise timing. This is much more difficult to realize because of the finite quality of commercially available shutters.

Servo shutters which are rather affordable typically have a delay of several milliseconds between the incoming TTL signal and the moment when they actually begin to move. Such a delay can be characterized with a photodiode (PD) and then be incorporated in the experimental cycle if it is constant. But a jitter of this delay which also is on the timescale of milliseconds for servo shutters can of course not be corrected. In addition due to the finite velocity of servo motors the slope of the shutter is not very steep which can also be a problem in some cases.

Shutters with very small jitters and steep slopes often are way more expensive than servo shutters. Furthermore they are often limited in the available aperture. High quality shutters with larger apertures there again often cause unwanted vibrations

on the optical table when they open and close. Hence it is an important step in setting up a cold atom experiment to find out for which laser beams switching with precise timing and complete blocking of the light is necessary and install an appropriate shutter for these beams.

3.2.2 Low- and high-field imaging

A small part of the light of the D2 laser is used for imaging of the upper hyperfine state of the ground state of the respective lithium isotope at zero or low magnetic field. In addition a further ECDL is installed to realize imaging of the lower hyperfine ground state at low magnetic fields and also imaging of both hyperfine ground states at various higher magnetic fields.

This so called imaging laser is offset locked on the D2 laser. With this lock we can address a broad frequency range and dynamically tune the locking point. The imaging light of the D2 laser and the light of the imaging laser are both transported with PM fibers to another part of the same optical table. There they are overlapped and distributed to all four fibers of the 3D-MOT (X, Y, Z1, Z2) and three additional imaging directions. The frequency of both imaging beams can be tuned with separate DPAOMs. In addition a fast shutter with low vibration⁸ is installed for the imaging light.

3.2.3 Raman sideband cooling

Another ECDL named Raman laser is the source of the laser light that we want to use to perform Raman sideband cooling on the atoms during site-resolved imaging in a deep optical lattice (see section 2.2.7 and 7.1). This part of the laser system is shown in figure 3.3. The laser light is first amplified and then coupled into a short PM fiber⁹. The two couplers of this fiber are placed close to each other because we only use this fiber as a filter for the beam profile and not for transportation of the laser light. We have to do this because the beam profile of the light that comes out of this amplifier has a rather bad overlap with the fundamental gaussian mode. The amplification of the laser power is satisfyingly high but the coupling efficiency into the fiber that we can achieve after additional beam shaping never exceeds 40 %.

Behind the fiber a small portion of the laser light is separated to overlap it with the light of the D1 laser, which we use for the gray molasses, to create a beat signal of the interference between the two lasers that we want to use to offset lock the Raman laser to the gray molasses laser. The beat is measured with two fast photodiodes¹⁰. One photodiode is used for the offset lock and the other one monitors the beat signal. Another small portion of the laser light is separated to be coupled into a fiber that can be connected with a wavelength meter¹¹ to get the absolute value of the frequency

⁸Stanford Research Systems: SR474 (shutter driver), SR475 (shutter head)

⁹Thorlabs: P3-630PM-FC-2

¹⁰Hamamatsu Photonics: G4176-03

¹¹Toptica Photonics: HF-ANGSTROM WS/6-USB

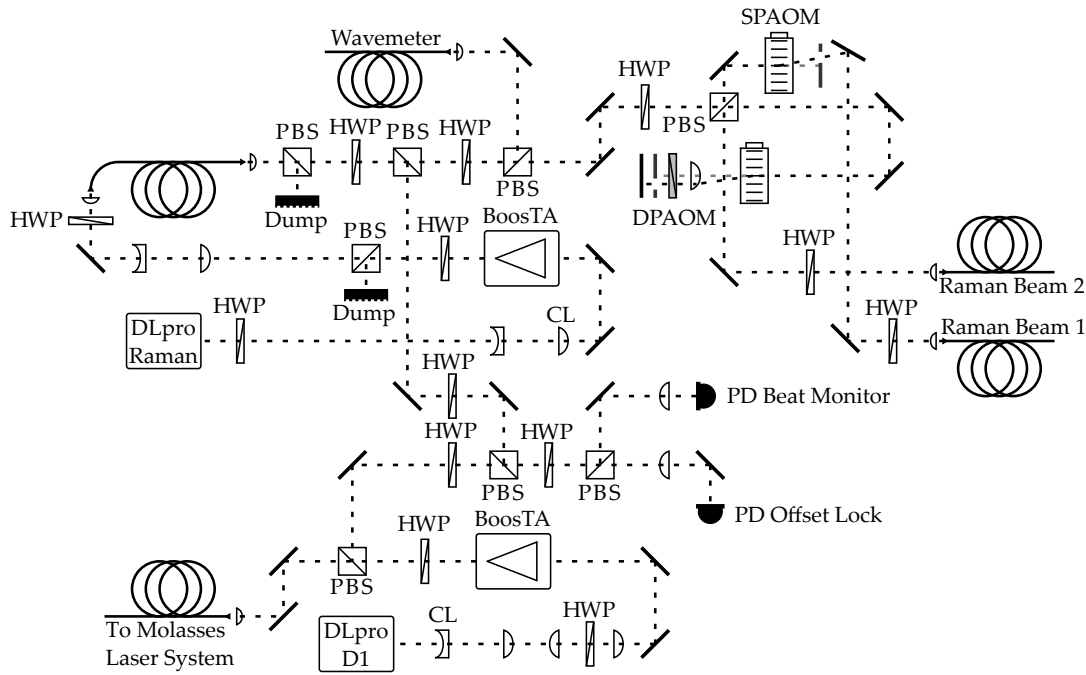


FIGURE 3.3: Part of the laser system that is relevant for the Raman laser and its offset lock on the D1 laser which is used for the gray molasses. The used abbreviations are explained in the main text and listed in the “List of Abbreviations” in the appendix of this thesis. As a design library for drawing the optics components the author uses [18, 103, 104].

of the laser light with an accuracy of at least ± 600 MHz.

The rest of the laser light behind the fiber is used to create the two Raman beams. Our first approach is that we use two separate fibers to bring the two Raman beams from the optical table, where the laser systems for resonant light are located, to the other optical table where the vacuum chamber is placed. Therefore, we split the light into two parts using a PBS and install a SPAOM for Raman beam 1 and a DPAOM for the Raman beam 2. Behind the AOMs both beams are coupled into a 10 m long PM fiber to be transported to the other optical table. In this way the power of each beam can be adjusted independently and each beam can be switched on and off separately. In addition the DPAOM can be used to tune the frequency difference between the two beams.

The just described setup is very flexible and practical but for the first experiments with the Raman beams we decide to use a different approach because we suspect that two separate fibers for the two Raman beams could lead to decoherence between the beams and hence limit the coherence time of the two-photon Raman transition. In this alternative setup we only use the path of Raman beam 1 with the SPAOM and hence only one fiber. The first Raman beam is sent through the glass cell at an angle of $\varphi \sim 20^\circ$ to the y -axis of the coordinate system that we defined for our experimental setup (see figure 3.4).

The second Raman beam is created by sending the first Raman beam into a DPAOM after it has passed the glass cell. Before the DPAOM we install a lens with a long focal length of $f = 750$ mm to recollimate the first Raman beam that is focused to

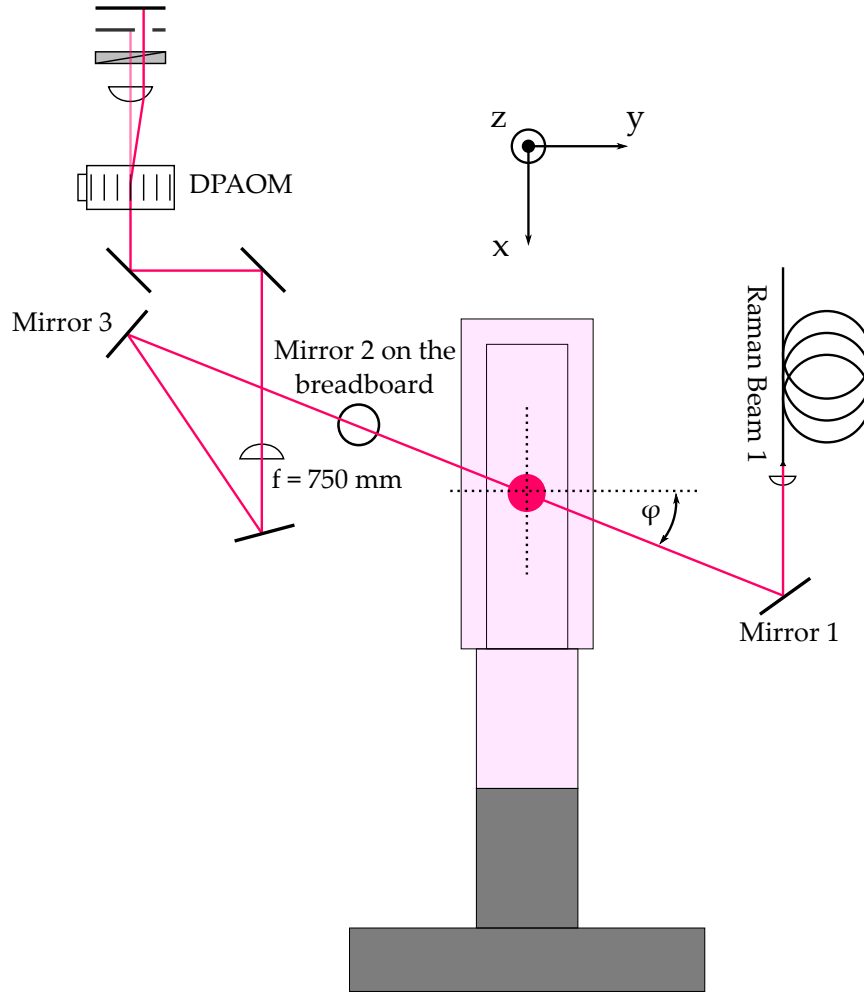


FIGURE 3.4: Top view of the Raman setup around the glass cell. The image is not to scale for better visibility of our approach. The Raman beam is sent through the glass cell at angle of $\varphi \sim 20^\circ$ to the y-axis.

the position of the atoms using the lens inside its outcoupler. Behind the DPAOM the second Raman beam is then automatically focused again to the position of the atoms by the recollimation lens. The polarization of the first Raman beam is out of plane (s-polarization) and the quarter-wave plate in the DPAOM is adjusted such that the polarization of the second Raman beam is in plane (p-polarization). We can again use the DPAOM to tune the frequency difference between the two Raman beams and to independently switch off the second Raman beam. The SPAOM on the optical table of the laser systems switches both Raman beams in this configuration. We can also tune the power in the second Raman using the DPAOM but the power is limited to $\sim 85\%$ of the power in the first Raman beam due to the limited efficiency of the DPAOM.

For Raman sideband cooling the difference vector of the two Raman beams needs to have a component along all axes of the pinning lattice. Hence we send the Raman beam through the glass cell at an angle of $\theta \sim 7^\circ$ to the horizontal x-y-plane to create a component along the vertical z-direction (see figure 3.5). We do this by the using

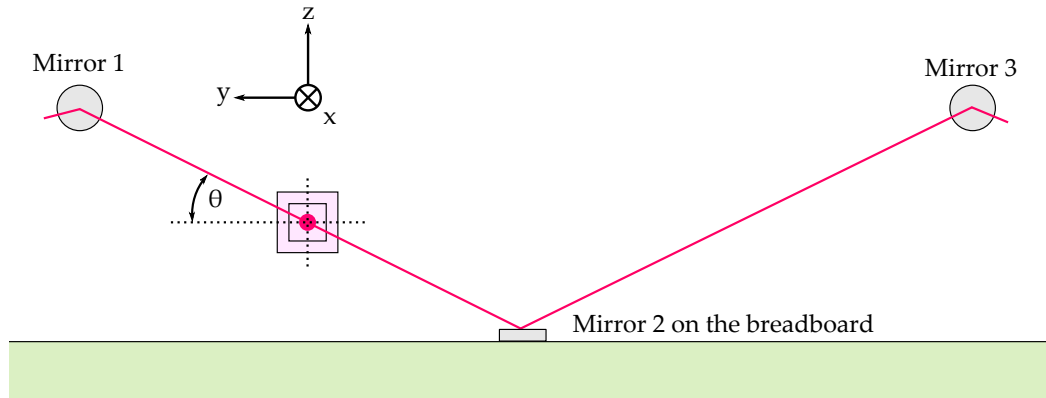


FIGURE 3.5: Side view of the Raman setup around the glass cell. The image is not to scale as for example the angle θ between the Raman beams and the horizontal x - y -plane is drawn much larger than its actual value of $\sim 7^\circ$ for better visibility of our approach with the mirror (“Mirror 2”) that is mounted directly on the breadboard.

the outcoupler of the Raman beam and the mirror that is labeled “Mirror 1” in both figures. Behind the glass cell the beam is reflected by “Mirror 2” that is mounted directly on the breadboard. Using this mirror and “Mirror 3” the Raman beam is aligned to the horizontal plane and then sent into the DPAOM.

For efficient Raman sideband cooling we need the Raman laser to be red detuned to the D1 transition of the respective lithium isotope in the range of 5 to 8 GHz (see section 2.2.7). This can be automatically realized by offset locking the Raman laser to the D1 laser that we use for the gray molasses. The scheme that we use to realize the offset lock has been around in the cold atom community for quite some time [105]. It makes use of the frequency-dependent phase shift of the beat signal of the two lasers when it runs through a coax cable. The electronics part of our offset lock was partially adapted from [103] and is shown in figure 3.6. All amplifiers, the bias-tee, the mixer, the power splitter, the phase detector and the low pass filter are from the company *Minicircuits*. The photodiode as mentioned before is from *Hamamatsu*, the frequency divider from *RF Bay*, sold in europe by *Nano-Giga*, and the frequency generator for the local oscillator is from *Hameg*.

The frequency divider divides the incoming signal by a factor of 6. This has the advantage that only the photodiode, the bias tee and the two amplifiers in front of the

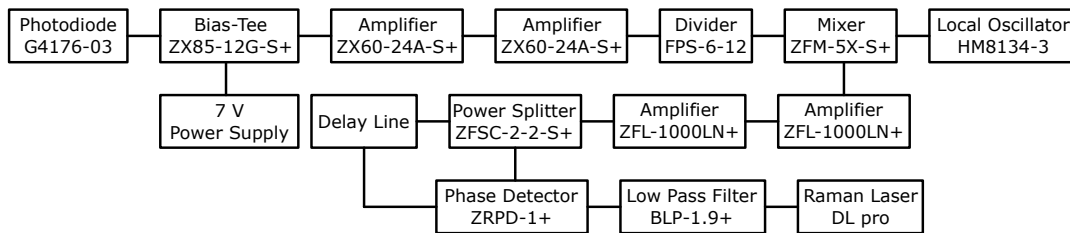


FIGURE 3.6: Electronic circuit for the offset lock of the Raman laser to the D1 laser.

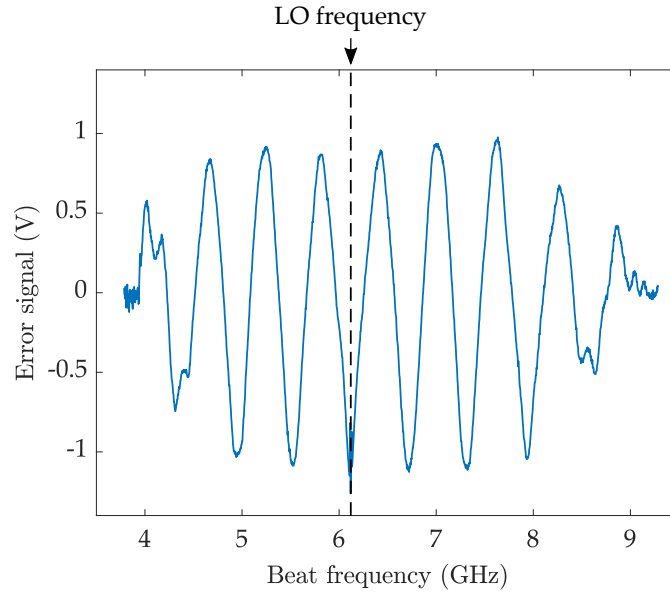


FIGURE 3.7: Resulting error signal of the offset lock setup. The real frequency of the local oscillator is a factor 6 smaller than the position of the black dotted line because the beat note of the two lasers is divided by 6 with a frequency divider before it is mixed with the local oscillator. Figure adapted from [106].

divider have to be suitable for several GHz. All elements behind the divider including the local oscillator only need to be specified for up to 2 GHz to realize an offset lock for a frequency of at most 12 GHz.

The amplified and divided signal of the beat between the two lasers is mixed with the local oscillator whose frequency is in the same range. The mixed signal is again amplified and then split into two equal parts using a power splitter. One part runs through a delay line of coax cables whose length can be changed by simply connecting several cables of different lengths. Then both parts of the signal are recombined on a phase detector. The mixer also has an output at twice the frequency which is blocked by a low pass filter with a cutoff frequency of 1.9 MHz. The resulting output voltage of the phase detector varies as $\cos(\theta)$. The phase shift θ results from the delay line and is given by $\theta = 2\pi(\nu_{beat} - \nu_{LO})\tau$, with ν_{beat} being the beat frequency of the two lasers, ν_{LO} being the frequency of the local oscillator and τ being the time delay created by the delay line.

The resulting error signal, which is fed back to the Raman laser, is shown in figure 3.7. It enables locking of the Raman laser using the proportional-integral-derivative (PID) controller that is integrated in the locking module¹² of the laser over a range of several GHz. Between 5 and 8 GHz every slope has a range of approximately 300 MHz. The signal can be shifted by changing the frequency of the local oscillator and for locking on the negative slopes the signal can be inverted by the locking module. If we want to go to higher beat frequencies we just have to install a frequency generator for the local oscillator with a higher maximum frequency than 1.2 GHz.

¹²Toptica Photonics: DigiLock 110

The offset lock works the same for blue detuned and red detuned locking of the Raman laser to the D1 laser. In addition the mode hop free tuning range of the ECDL lasers is typically limited to 10 GHz. Both aspects can lead to confusion during the interpretation of the error signal. The wavelength meter that was mentioned before is very helpful and more than precise enough to lock on the right error signal in a large enough mode hop free range.

We try to measure the linewidth of the offset locked laser by looking at the beat signal on the monitor photodiode. Deviations of the beat note on time scales which are slow compared to the beat frequency limit the linewidth that can be stated to 4.7 MHz [106]. But we do not expect this to be a problem because the linewidth does not affect the frequency difference between the two Raman beams which is created with AOMs and this linewidth is still very small compared to the large detuning of the Raman beams. Therefore, the laser system and the offset lock for the Raman laser should be sufficient for Raman sideband cooling.

3.3 Crossed dipole trap

The advance in available laser power for optical dipole traps in combination with the successful implementation of gray molasses cooling has enabled faster and more effective production of quantum degenerate samples of both ^6Li [83] and ^7Li [107]. For our experiment we implement a crossed dipole trap of two beams intersecting at the position of the atoms to increase the trap depth and to compensate for the weak confinement along the propagation axis of a single-beam dipole trap.

The laser source for our setup which is shown in figure 3.8 is a ytterbium fiber laser¹³ with an output power of 100 W and a wavelength spectrum of $\lambda = 1070(3)$ nm. The laser can be switched on and off completely within $\sim 8 \mu\text{s}$ using a TTL signal [96]. In addition the laser power can be controlled with an analog voltage signal but the smallest possible output power is 4 W which is way to high for evaporative cooling to quantum degeneracy.

For further dynamic control of the laser power we do not follow the usual approach of using an AOM because an AOM would create additional thermal lensing effects. We instead use a combination of a Glan-laser polarizer¹⁴ and a zero-order half-wave plate¹⁵ in a motorized rotation mount¹⁶. After initial cleaning of the polarization of the laser light with a first Glan-laser polarizer the power that transmits through the second polarizer is dynamically controlled by rotating the half-wave plate in front of the polarizer using the motorized mount. The cleaning of the polarization is critical for achieving a good extinction ratio of the laser power at the end of the evaporation ramp.

¹³IPG Photonics: YLR-100-LP-AC

¹⁴Thorlabs: GL15-C26

¹⁵Thorlabs: WPH10M-1064

¹⁶OWIS: DRTM 40-D25-HiDS

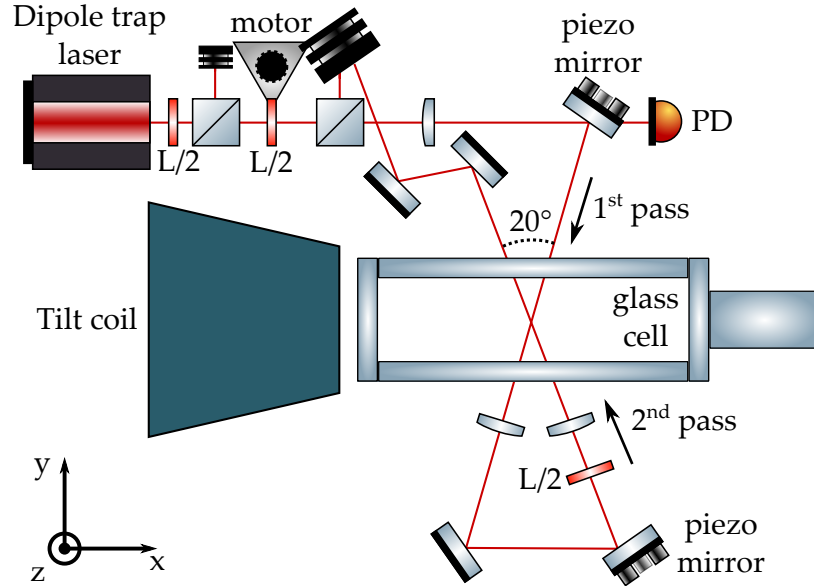


FIGURE 3.8: Setup of the crossed dipole trap. After cleaning of the polarization the power of the dipole trap beam is controlled using a half-wave plate in a motorized rotation mount. The beam is focused into the glass cell twice and overlapped on the atoms. The position of the beams is controlled with piezo mirrors, an additional half-wave plate avoids residual interference and a photodiode monitors the power of the dipole trap. The Tilt coil is also shown schematically for orientation. Figure adapted from [18, 96].

The internal driver of the rotation mount has a jitter that is way too high for reproducible experimental sequences. We therefore have to build our own driver using another drive unit¹⁷ in combination with a BeagleBone Black. The BeagleBone Black is addressed via a TCP/IP connection by the experimental control and the PID parameters of the drive unit are adjusted with a corresponding software¹⁸. The orientation angle of the rotation mount is controlled with a calibrated analog voltage from the experimental control. The development and characterization of this setup is described in detail in [18, 96, 108, 109]. We realize a very good extinction ratio of $(0.4 \pm 3.0) \cdot 10^{-5}$ for the power of the dipole trap laser, a standard deviation of the final trap depth of 0.86 % for a typical evaporation ramp to create a quantum degenerate gas and a jitter of the self-built drive unit of $\sim 360 \mu\text{s}$ which is way better than the jitter of the internal drive of the rotation mount. Although we avoid the thermal lensing of an AOM with this setup we face significant thermal lensing effects that come from the walls of the glass cell which we have to deal with when adjusting the dipole trap (see section 5.2.1).

Behind the second polarizer the dipole trap beam is focused ($f = 750 \text{ mm}$) to the position of the atoms in the glass cell resulting in a waist of $w_{0,fp} = 110(2) \mu\text{m}$. After its first pass through the glass cell the beam is collimated with a second lens ($f = 250 \text{ mm}$) before a third lens ($f = 200 \text{ mm}$) focuses it again to the same position during its second pass through the glass cell resulting in a waist of $w_{0,sp} = 92(1) \mu\text{m}$ [18]. Before the second pass of the beam through the glass cell an additional half-wave

¹⁷Technosoft: iPOS3602 MX

¹⁸Technosoft: EasyMotion Studio

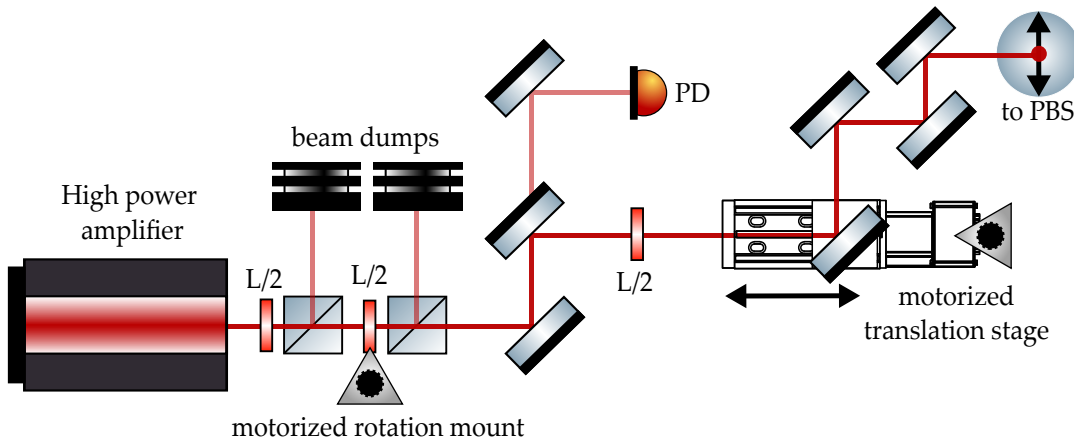


FIGURE 3.9: Setup of the accordion lattice. Polarization cleaning and power control via rotation mount are similar to the setup of the dipole trap (see figure 3.8). Dynamical tuning of the lattice spacing is achieved with a motorized translation stage. The half-wave plate in front of the translation stage balances the power splitting of the two beams that happens on the large PBS. In addition a photodiode is installed for power monitoring. Figure adapted from [18, 96].

plate is installed to make the polarization of the two beams orthogonal to each other to avoid effects of residual interference of the two beams. After the second pass the beam is sent into a water-cooled beam dump.

The fine adjustment of the two dipole trap beams is done with a piezo mirror¹⁹ for each beam. A photodiode behind the first piezo mirror is used for monitoring the dipole trap power and calibrating the rotation mount. The advantage of using the same laser beam for both arms of the crossed dipole trap is the recycling of the laser power. The disadvantage is that the adjustment of the first pass is always coupled to the adjustment of the second pass which can only be adjusted independently. In addition the effect of the first pass alone on the atoms can be observed by blocking the second pass but it is not possible to observe the effect of the second pass alone.

3.4 Accordion lattice

As already discussed in section 2.2.4 our choice for creating a 2D sample for quantum gas microscopy is the so-called accordion lattice [60]. The laser source for our setup is a distributed feedback (DFB) fiber laser²⁰ with an output power of 10 mW at a wavelength of 1069.8 nm. After a first preamplifier the output power is 250 mW which can then be distributed to four different amplifiers. All amplifiers are from the company *Azurlight Systems*. Up to now we use one amplifier with an output power of 40 W for the accordion lattice and another 40 W amplifier for the triangular lattice in the horizontal plane (see section 3.5).

The first part of the accordion lattice setup that is displayed in figure 3.9 is placed on the optical table of the vacuum chamber underneath the breadboard around the

¹⁹Radiant Dyes Laser & Accessories: MDI-HS-2-3025-M6

²⁰NKT Photonics: Koheras ADJUSTIK POWER Y10

science cell. As for the dipole trap (see section 3.3) the polarization of the laser is cleaned with a half-wave plate and a Glan-laser polarizer. The power of the laser beam is again controlled with the combination of a half-wave plate in a motorized rotation mount and a second glan-laser polarizer. A photodiode detects the light that is transmitted by one mirror to monitor the power and another half-wave plate balances the power between the two accordion lattice beams.

The dynamical tuning of the lattice spacing for the realization of the accordion effect is created with a mirror that is mounted on a motorized translation stage²¹. The motor controller²² has a jitter of $\sim 400 \mu\text{s}$ [96] which is close to the jitter of the drive unit that we built for the rotation mount. Therefore we can directly use the motor controller of the translation stage which is again controlled by a Beaglebone Black that can be addressed by the experimental control via a TCP/IP connection.

After additional mirrors for adjustment of the accordion lattice the laser beam is sent upwards through a hole in the breadboard around the science cell into a home-built holder. This holder contains the large PBS²³ with the coated quarter-wave plate on one side and the two mirrors in mirror holders with high-precision screws for independent fine adjustment of the two beams. The beams are sent onto a large aspheric lens²⁴ made out of fused silica to avoid thermal lensing effects of the high power lattice beams. This asphere has an effective focal length of $\sim 87.6 \text{ mm}$ for the lattice wavelength of 1069.8 nm [18, 96]. We cut it into a rectangular shape to have free space for the dipole trap beams around the aspheric lens. The rectangular lens is fixed in a home-built holder which is connected to a very small XYZ translation stage²⁵.

3.5 Triangular lattice

We use another 40 W amplifier of the laser source that was mentioned in section 3.4 as the starting point for the triangular lattice. It is designed for pinning the atoms during site-resolved fluorescence imaging but it can also be used as a physics lattice as we already discussed in section 2.2.5. We get the most stable performance of the laser when the final amplifier is constantly tuned to maximum output power. We therefore install a half-wave plate, a Glan-laser polarizer and a water-cooled beam dump directly behind the amplifier to enable manual tuning of the laser power for safe adjustment of the lattice laser system. This laser system as well as all other high power lasers is placed on the same optical table as the vacuum chamber to avoid long fibers and long beam paths for high laser powers.

The laser power is equally distributed to three different but equally designed paths for the three lattice beams using half-wave plates and PBS. Each beam is sent into a

²¹Zaber: ZAB-LSQ075D-E01T3-MC03

²²Zaber: ZAB-X-MCB1-KX13B

²³Bernhard Halle: BHN 2016.0077.0003

²⁴asphericon: AFL50-80-S-C

²⁵Elliot Scientific: MDE261, MDE262

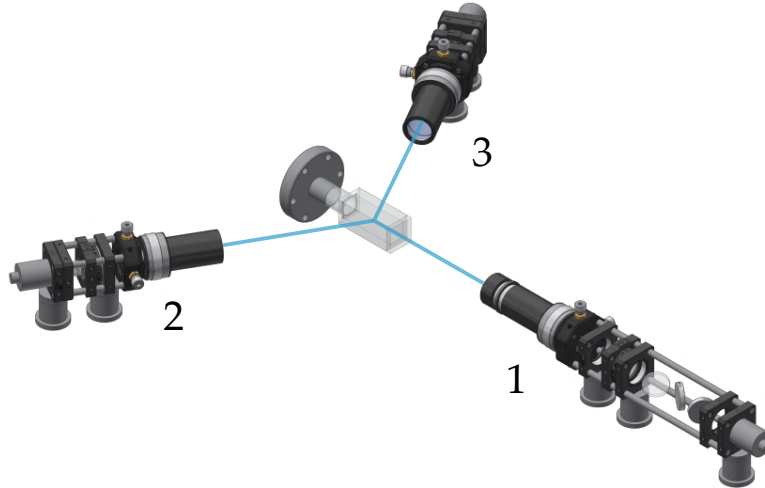


FIGURE 3.10: Telescopes behind the fibers for the beams of the triangular lattice. For a clear assignment throughout this thesis we label the telescopes with numbers. Figure adapted from [18].

slow shear AOM²⁶ for independent switching and power control of the beams. Slow shear AOMs have very good thermal properties but also slower timescales which is not limiting us so far as they are still $< 1 \mu\text{s}$. Behind the AOMs the beams are coupled into 5 m long high power single mode PM fibers²⁷. A photodiode, that detects the residual transmitted light of one of the mirrors behind the AOMs, is installed for each beam to monitor the power in front of the fibers.

The telescopes for the lattice beams behind the fibers, which can be seen in figure 3.10 and which are labeled with numbers for a clear assignment, are designed as compact as possible to assure a high stability of the three lattice beams. Behind the outcoupler²⁸ of the fiber, which is the same model as the incoupler, a PBS is installed for polarization cleaning. The polarization axes of the fibers and a half-wave plate directly in front each fiber are aligned such that the transmission through the PBS behind the fibers is maximized and that the polarization of the light matches the polarization axes of the fibers. A half-wave plate behind each PBS enables changing of the lattice geometry.

Due to the fact that no additional mirrors for adjustment of the beams are installed behind the fibers the coarse adjustment of the lattice beams has to be done by positioning the telescopes as precisely as possible on the breadboard (see section 6.2.1). The fine adjustment is then done by adjusting the achromatic lens²⁹ ($f = 150 \text{ mm}$), that focuses the lattice beams on the position of the atoms, with a XY translator³⁰ and a zoom housing³¹. The lens tube in the telescope that is labeled with number 1 couples out the lattice beam along the axis of the push beam. It has to be longer

²⁶Gooch & Housego: I-M080-3S2G-3-LV11

²⁷NKT Photonics: Photonic crystal fiber, aeroGUIDE POWER-15-PM

²⁸Schäfter + Kirchoff: 60FC-SMA-T-23-M25-03

²⁹Thorlabs: AC254-150-C

³⁰Thorlabs: CXY1

³¹SM1ZM

because the Tilt coil (see section 4.2) sets a lower limit for the distance between the telescope and the science cell.

In addition a dichroic long pass mirror³² and two beam samplers³³ are installed in telescope 1. The dichroic mirror couples out the light of the imaging beam at 671 nm in this direction and the beam samplers couple out a small portion of the lattice beam for locking the intensity and phase of the lattice beam. This is necessary because, after traveling through the science cell, the laser beam is dumped in the vacuum chamber. The telescope is actually slightly tilted so that the beam does not hit the differential pumping tube which would lead to a rapid increase of pressure in the chamber. For the other two lattice beams the light for intensity and phase locking can be picked up with beam samplers after they have passed the science cell. The main part of their power is then sent into water-cooled beam dumps.

The light for the intensity control of each beam is split into two parts and detected by two photodiodes. For low powers of the lattice a relatively fast photodiode³⁴ is the starting point for a self-built intensity control setup addressing the slow shear AOMs in front of the fibers. For ramping up the full power we simply set the intensity control to a fixed value where we calibrated the diffraction of the respective AOM into the used order to be at its maximum. A second photodiode³⁵ is installed for monitoring the laser power in this regime.

The installation of a phase lock could decrease blurring of the interference pattern of the triangular lattice during the fluorescence imaging. If one beam, which would be the lattice beam along the direction of the push beam in our case, is locked to each of the two other beams, these two beams would then automatically be also locked to each other. An analysis of the optical phase noise of our triangular lattice, the plans for the potential phase lock and a description of the intensity control of the lattice beams can be found in the PhD thesis of Andreas Kerkmann [18].

3.6 High resolution imaging setup

The central element of our setup for achieving site-resolved fluorescence imaging of ultracold lithium atoms in a deep pinning lattice is a custom-made high resolution objective³⁶ with a numerical aperture of $NA = 0.5$. This enables a collection efficiency of $\sim 6.7\%$ for the photons that are isotropically scattered by the atoms. According to the Rayleigh criterion this results in a diffraction-limited resolution of $d_{min} = 1.22 \lambda / 2NA \approx 819$ nm when fluorescence imaging is performed on the D2 line of lithium at $\lambda = 671$ nm. In addition to 671 nm the objective is also diffraction-limited for 532 nm, 780 nm and 1064 nm. It is infinity corrected including the 5 mm thick wall of the science cell in the optical path between the atoms and the

³²Thorlabs: DMLP900

³³Thorlabs: BSF10-C

³⁴Thorlabs: PDA10A

³⁵PDA36A

³⁶Special Optics: item 1-21992

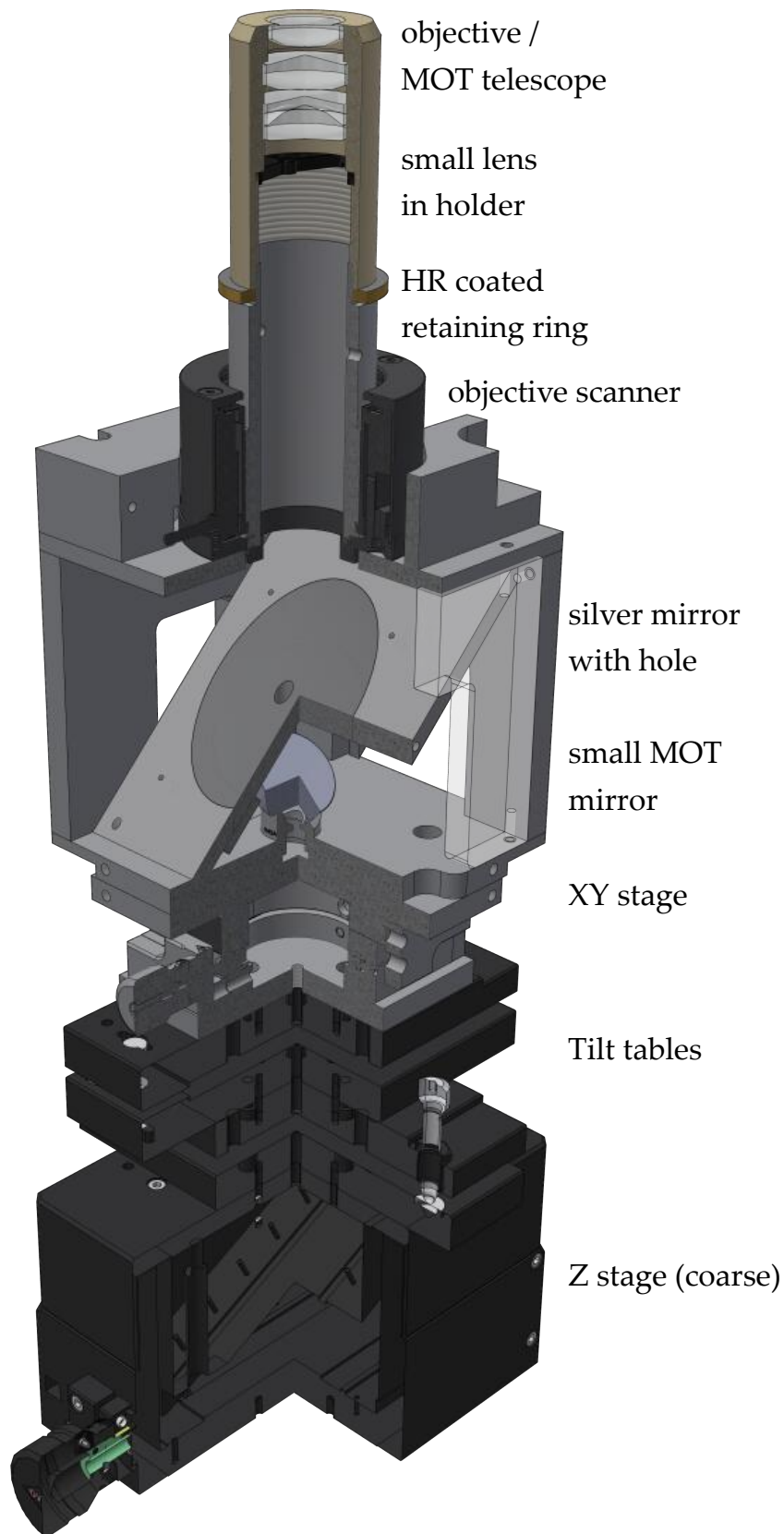


FIGURE 3.11: Optomechanics for the adjustment of the objective and the integration of the MOT beam through the objective. Figure adapted from [18].

objective. The aperture of the objective is 25 mm, the working distance 19 mm and the effective focal length 24.7 mm. It has an AR coating between 532 nm and 1064 nm whose maximum residual reflection is always smaller than 0.5 % in this wavelength range and its achromatic focal shift is smaller than 80 μm .

Due to the infinity correction of the objective we need an additional tube lens to image the picture of the atoms in the lattice onto the EMCCD camera³⁷. We decide for a 2" lens³⁸ with a focal length of $f = 2000$ mm. The correct adjustment of the tube lens is also critical for achieving a nearly diffraction-limited imaging setup. It is therefore mounted in a precision lens positioner³⁹. When the objective is treated as a single lens with an effective focal length of 24.7 mm, this results in a magnification of the image of $M \approx -80$ which is a suitable choice for our experimental setup in order to on the one hand resolve the structure of the optical lattice on the camera chip but on the other hand avoid too much photonic shot noise by distributing the signal to too many pixels. Numerical simulations that have been performed by Jan Mika Jacobsen during his Master's thesis [110] additionally confirmed that the choice of the magnification is reasonable for our experiment.

Due to the high NA the field of view of the objective is only 150 μm and the depth of focus is only $\Delta z = \lambda/\text{NA}^2 \approx 2.7$ μm in case of a diffraction-limited imaging setup. Therefore, a very precise adjustment of all spatial degrees of freedom of the objective is necessary to achieve nearly diffraction-limited imaging. We seek to realize this with the combination of optomechanics that is displayed in figure 3.11 for mounting the objective directly underneath the glass cell. The base is an elevator stage⁴⁰ for coarse alignment of the height of the objective. Two tilt stages⁴¹ enable alignment of the axis of the objective before an XY stage⁴² is installed for the adjustment of the field of view. It is practical to install the tilt tables underneath the XY stage because an adjustment of the tilt automatically affects the adjustment of the field of view. Finally a precision objective scanner⁴³ enables fine tuning of the focus position. The HR coating on the retaining ring could be used to reflect a laser beam for an adjustment setup for the objective that is independent of the signal coming from the ultracold atoms.

We have two of the described objectives so that we could install a second one opposite to the first objective above the glass cell. Initial experiments up to the production of a molecular BEC of ${}^6\text{Li}$ atoms (see chapter 5) have been performed without an objective being installed. As discussed before there is no transport of the atoms after the 3D-MOT. In consequence the 3D-MOT and site-resolved imaging in the optical lattice take place at the same position. This is a technical challenge because a collimated MOT beam can not be easily created when it has to pass through the objective

³⁷Oxford Instruments: Andor iXon Ultra 897

³⁸Melles Griot: PLCX-50.8-999.4-UV-633-1064

³⁹Newport: LP-2A

⁴⁰OWIS: HT 100-30

⁴¹OWIS: NT 65x120-FGS

⁴²OWIS: KT 65-STA-UM

⁴³Physik Instrumente: P-726 PIFOC

because such a laser beam is very divergent after passing the objective. Hence, very large optics would be needed to realize this MOT beam and to separate it from the imaging light.

To avoid such an impractical setup we instead install an additional small lens ($f = 4$ mm) with a diameter of only 4 mm inside the objective to create the collimated MOT beam. The mount for this lens was built with a 3D printer. The beam is guided onto the lens using the small MOT mirror to send it through the hole in the big silver mirror (see figure 3.11) while $\sim 96\%$ of the fluorescence light for imaging the atoms is reflected by the silver mirror and therefore separated from the path of the MOT light. The small lens is set off by 6 mm from the axis of the objective to avoid complete blocking of a specific part of the information in the imaging light. This offset creates a MOT beam that is angled by $\sim 14^\circ$.

With this setup we again realize a performance of our experiment that is comparable to before the installation of the objective. In addition we check in a separate test setup for the objective before it is installed that the small lens does not reduce the possible NA of 0.5 in the case of diffraction-limited imaging for our setup. This is done by measuring the point spread function (PSF) of our imaging system and getting the effective NA from a fit to the data. A more detailed discussion of the optomechanical setup for the objective and the analysis of our imaging system in the test setup can be found in [18, 111]. The installation of the objective directly under the science cell and the creation of the MOT beam using the small lens is discussed in [18, 96].

Chapter 4

Magnetic field coils

This chapter is dedicated to the magnetic field coils which are an essential part of the experimental apparatus. They have to be precisely planned and manufactured to realize the needed magnetic fields without blocking valuable space. After a short introduction to the possibilities of using magnetic fields in experiments with ultracold atoms we discuss in detail the central coils for our experiment for the creation of homogeneous and gradient magnetic fields. In addition we show the offset coils for the compensation of magnetic stray fields. In the last section of this chapter we describe the infrastructure for supplying high currents and efficient water cooling. In addition we exemplarily analyze the switch-on behavior of one of the large coil pairs.

The design and setup of the central magnetic field coils and the corresponding infrastructure has mainly been carried out by the author with support of Andreas Kerkmann and Benno Rem under the supervision of Klaus Sengstock and Christof Weitenberg. The author started the design of the coils and the simulation of the coil properties during his Master's thesis [97]. In the course of his PhD thesis the author further elaborated the design and setup of the coils and the corresponding infrastructure and managed to put the coils into operation in the experiment.

4.1 Magnetic fields for ultracold atoms

Magnetic fields have always been a crucial ingredient for experiments with ultracold atoms. A variety of magnetic field configurations has been developed to trap, cool and manipulate atoms in many different ways. There are basically two ways to generate the desired magnetic fields:

- **Permanent magnets** are space saving, affordable and a reasonable amount of bar magnets can already create useful magnetic fields. But there is a severe disadvantage: Their magnetic field is static and can not be turned off or modulated without moving the magnets.
- **Coils** are the more complex but also much more versatile approach to creating magnetic fields. Coils are usually made out of between one and several hundred windings of copper wire. Usually they have to be home-built or a

specialized company produces them custom made for the specific needs of the respective experiment. In addition suitable power supplies, water cooling and electronics are needed for applying and switching the high currents that run through the coils.

The higher flexibility of coils makes them more common in experiments with ultra-cold atoms compared to permanent magnets but the latter ones can still be found in several experiments today. In our experiment for example they are used to create the magnetic field for the 2D-MOT. We now have a look at the different types of magnetic fields that are often used in cold atom experiments and how they can be created. The mentioned applications of the different types of fields are not a complete list but include the configurations that we consider to be relevant for our experiment when we design the coils. There are also more complex coil configurations than single coils and coil pairs [112, 113] but we do not discuss them here because we do not have such coil configurations in our experiment.

Homogeneous fields

Magnetic fields that are very homogeneous in all three spatial directions can be created with a coil pair in the so called Helmholtz configuration. Helmholtz configuration means that the radius of both coils is equal to the distance between the coils and that the current in the two coils is of the same strength and flowing in the same direction. A coil pair in perfect Helmholtz configuration creates a completely homogeneous field in a small area around its center. Deviations from the Helmholtz configuration lead to a residual curvature of the magnetic field around a saddle point in the center of the coil pair. Homogeneous magnetic fields can be used to address the Feshbach resonances of atoms to tune their scattering length, to break the energy degeneracy of different spin states and to compensate the geomagnetic field and other homogeneous stray fields in the lab.

Gradient fields

A magnetic quadrupole creates a field with a constant gradient along all three spatial directions in a region around its center. The gradient along the axial direction of the quadrupole is of opposite sign and twice as high as the gradient in the radial plane. Such a field is an essential ingredient for a MOT. It can be realized with permanent magnets or with a coil pair in anti-Helmholtz configuration where the difference compared to the Helmholtz configuration is that the current in the two coils is flowing in opposite directions. However, for the anti-Helmholtz configuration the geometric configuration of the coil pair is not very critical for creating a quadrupole field in the center of the coils. Quadrupole fields are also used to realize for example magnetic traps, additional gradients to enforce evaporation in optical dipole traps, separation of different spin states in Stern-Gerlach experiments and compensation of gravity to levitate atoms. In general the same coil pair can be used

in Helmholtz and anti-Helmholtz configuration but in many experiments there are at least two pairs of coils if both configurations are required.

Field of a single coil

The magnetic field of a single coil has its maximum in the center of the coil and it falls down along its axis. In some cases also a single coil can be useful to shift the position of the atomic cloud or to break the radial symmetry of the magnetic field of a coil pair. We want to make use of an additional single coil to evaporatively cool in a single plane of our vertical optical lattice. In addition the combination of a single coil and a coil pair can be used for the realization of a magnetic trap that incorporates the quadrupole and the Ioffe configuration (QUIC trap) [114].

Radio frequency coils

Coils are also used to address atoms with a single frequency in the MHz to GHz regime to drive inner atomic transitions in this frequency range. These coils are designed and manufactured such that the outcoupling of radio frequency (RF) power by the coil is maximized at a specific frequency. RF coils with a variety of sizes, forms and winding numbers have been developed to achieve a good impedance matching in the desired frequency ranges and to match the spatial constrictions of the respective experiment.

4.2 MOT coils, Feshbach coils and Tilt coil

The design of the magnetic field coils happens in an early stage of a cold atom experiment because they are usually placed close to the atomic cloud so that they occupy a lot of space which can not be used to for example propagate laser beams. The design process is a continuous interplay between the properties that the coils shall have to satisfy the needs of the experiment and the spatial and technical restrictions of their actual realization. We profit of course from the knowledge of some of the experiments with ultracold lithium that already exist when we design the coils [115–119]. This section is dedicated to the central coils of our experiment: two coil pairs that we call the “MOT coils” and the “Feshbach coils” and an additional single coil named “Tilt coil”. In section 4.2.1 we mention some of the requirements and restrictions for the coils in our experiment, section 4.2.2 describes the simulation of the coil properties that we do during the design process, section 4.2.3 deals with the fabrication of the coils and section 4.2.4 covers the characterization of their actual properties. In section 4.2.5 we discuss in detail the magnetic field configurations which can be realized with the coils and how they can be used in the experiment.

4.2.1 Requirements and restrictions for the design of the coils

One of the useful features of both lithium isotopes is the existence of a very broad Feshbach resonance [15] which enables precise adjustment of the interaction strength between the atoms. The magnetic field range of those resonances tells us which field strength has to be created with the coils to be able to completely scan across the respective resonances.

In addition to the lithium oven we also have dispensers filled with ^{85}Rb and ^{87}Rb in the vacuum chamber of our experiment. So in principal we could work with ^6Li , ^7Li , ^{85}Rb , ^{87}Rb or different mixtures of these four isotopes. When we look up the Feshbach resonances for all these configurations in the literature [15], we find that the Feshbach resonance of a mixture of ^6Li and ^{87}Rb has the highest center value which is $B_0 = 1067\text{ G}$ and it has a width of $\Delta = 10.6\text{ G}$. For good control over the scattering length of the atoms we want the magnetic field of the coils to be as homogeneous as possible. To create magnetic fields with such a big strength includes some technical challenges, among other the dissipation of a lot of electrical power.

We know from other experiment working with lithium atoms that the 3D-MOT requires a gradient field of at least 50 G/cm in the axial direction of the respective coil pair. This is a doable task compared to the high offset fields that we just have mentioned. But as we discuss in section 4.2.5 gradients of up to 250 G/cm can be useful in some situations. So we keep in mind that the coils should also be able to realize such high magnetic gradients.

These are only the basics of all the magnetic field configurations that we take into account when we design the coils. We discuss them and the possibilities that arise from combining different coils and coil pairs with each other in more detail in section 4.2.5.

A more technical challenge in designing the coils is the limited space that can be used to place the coils without blocking all the laser beams that are typically needed in a modern quantum gas experiment. In addition we already have to take care in the design process that efficient cooling of the coils is possible considering the dissipated power. When the infrastructure to supply and cool the coils is planned all components have to match the requirements for sufficient power supply and efficient water cooling of the coils.

4.2.2 Simulation of the coil properties

When we want to estimate the quality of a draft for the coil setup we have to be able to calculate all the relevant properties that these coils approximately have. These include the realized magnetic field strength, the inductance, the required electrical power and the resulting ohmic heating. For efficient cooling of the coils we use a square wire with a round hole in its center for the cooling water. Therefore, we also discuss how to assure the water flow rate through the coils to be sufficient.

Magnetic field

We first show how we calculate the resulting magnetic field of a specific number of windings in a respective geometric configuration. We use a code written with the software *Mathematica*¹ for this task. In this code each winding is assumed to be a perfect circle with no spatial extent. This is of course a simplification but the calculation becomes much easier in this way and the deviation of the simulation from reality is reasonably small. Then we can calculate the resulting magnetic field $\mathbf{B}(\mathbf{r})$ by using the Biot-Savart law:

$$\mathbf{B}(\mathbf{r}) = \frac{\mu_0}{4\pi} I \int_C \frac{d\boldsymbol{\ell} \times \mathbf{r}'}{|\mathbf{r}'|^3} . \quad (4.1)$$

The magnetic field is generated by a current I along a path C with μ_0 being the vacuum permeability. This integral can be solved analytically only in special cases. Therefore, we solve it numerically in our simulation.

A coil pair with several windings and hence a finite spatial extent can not match the geometric configuration of a perfect Helmholtz coil. Thus, the magnetic field of our coil pairs in Helmholtz configuration have a residual curvature. This curvature can be approximated as a harmonic oscillator close to the center of the coil pair. It leads to an additional confining or anti-confining potential for the atoms which can be quantified in terms of a trap frequency ω of a harmonic oscillator via

$$E(z) = \frac{1}{2} m_{atom} \omega^2 z^2 = \mu_B \cdot |\mathbf{B}| = \mu_B a z^2 \quad \iff \quad \omega = \sqrt{\frac{2\mu_B a}{m_{atom}}} , \quad (4.2)$$

with μ_B being the Bohr magneton. We get the parameter a from a parabolic fit to the results of simulated magnetic field strengths of a coil pair. With this parameter we can then directly calculate the corresponding trap frequency of the residual curvature along the respective direction. We mostly work with the respective low-field seeking ground states of both lithium isotopes in our experiment (see appendix B). Therefore, we discuss the influence of created magnetic offset fields only on low-field seeking states. In addition the resulting trap frequency of a residual curvature depends on the mass m_{atom} of the trapped atom. We always consider ⁶Li when trap frequencies are discussed because the work in this doctoral thesis was completely done with ⁶Li. Moreover, the trap frequencies for ⁷Li are only 7.4% lower than the trap frequencies for ⁶Li.

According to Earnshaw's theorem there are no maxima but only saddle points of the magnetic field. This means for example: If the residual curvature of a coil pair in Helmholtz configuration is trapping for high-field seekers along the axial direction of the coil pair then it has to be anti-trapping for high-field seekers along the radial direction. This has important consequences when we for example want to combine

¹Wolfram Research, Inc., www.wolfram.com

imaging at high magnetic fields with Time-of-Flight (ToF) measurements (see section 5.2.1). In addition the axial trap frequency of a coil pair is a factor of $\sqrt{2}$ larger than the radial trap frequency due to symmetry reasons.

Inductance

The inductance of the coil drafts is evaluated with a program called *FEMM*² that is available for free on the internet. *FEMM* is an abbreviation for *Finite Element Method Magnetics* which is the numerical method that is used in this program. The coil setup can be inserted into this program in an intuitive way and it returns the inductance of the coils among other electrical properties.

Required electrical power

We again assume the windings of the coils to be perfect circles. So the complete wire length l of a coil draft simply becomes the sum of the length of all windings. Then the required voltage U for a needed current I is

$$U = \frac{Il\rho_{Cu}}{A} \quad , \quad (4.3)$$

with A being the conducting cross-sectional area and ρ_{Cu} being the electrical resistivity of copper. The resulting electrical power P is

$$P = \frac{I^2 l \rho_{Cu}}{A} \quad . \quad (4.4)$$

Water flow through the wire

Fluid dynamics offer different equations to calculate the flow of a fluid through a tube. But it is not trivial to answer the question whether one of these equations is suitable for our situation where we pump water with a pressure of several bar through the small hole of a copper wire that is wound many times with a small bend radius. We tried to do some calculations but the results turned out to be not very accurate compared to the actual flow rates.

We instead compared the plan for our coils with the coils used in other experiments working with lithium atoms. Compared to these experiments our coils are placed very close to the atomic cloud which reduces the number of windings that is needed to realize the desired magnetic fields. Both aspects reduce the final length of the wire for a coil and therefore the resistance, the required voltage and finally the dissipated power of the coils. Less dissipated power leads to less heating and hence the demands on the water cooling decrease. In addition a shorter wire length results in higher water flow rates which of course increases the cooling efficiency. In conclusion the benefit concerning water cooling is disproportionately high when the length of the wire for a coil can be reduced. Thus, we can use cooling infrastructure with

²<http://www.femm.info/wiki/HomePage>

specifications that are comparable to what is used in other lithium experiments and expect even better working conditions for our experiment.

4.2.3 Fabrication of the coils

We now discuss the concrete plan for the coils and how they are manufactured. When a coil is designed there is always a trade-off between the number of windings and the maximum current. Both factors increase the realizable magnetic field strength but they are also conflicting at the same time. If a smaller wire is used more windings can be placed in the available space. But if a wire with a higher conducting cross-section is used, higher currents can be achieved before the resulting ohmic heating becomes impractical.

It turns out that the choice of the wire often differs with the required magnetic field strength. Experiments working for example with ultracold potassium or rubidium usually do not need magnetic fields that are as high as in experiments working with lithium atoms. In these experiments coils are often made out of a wire with a smaller diameter and no hole in its center and cooling water is flowing around the copper wire in the coil holder. The maximum current in such experiments is often limited to values between 100 A and 130 A.

Experiments working with ultracold lithium typically require currents of up to 200 A or even higher. These experiments often use thicker, square- or rectangular-shaped wires with a round hole in their center. The cooling water is pumped directly through this hole. These wires have a larger conducting cross-section even though the area of the hole in the center has to be subtracted from the conducting cross-section. The larger measurements of these wires limit the number of possible windings but as mentioned before a higher number of windings disproportionately increases the demands on water cooling while the created magnetic field is scaling only linearly with the number of windings.

The MOT coils, the Feshbach coils and the Tilt coil are manufactured by the company *Oswald* but the coil holders made out of aluminum are designed by Andreas Kerkmann [18] and manufactured at our workshop. The coil holders are sent to *Oswald* and they wind the coils on the holders according to our draft.

The used wire is square shaped with an edge length of 4 mm. The hole in the center has a diameter of 2.5 mm and the edges are rounded with a radius of 0.5 mm. This results in a conducting cross-section of 10.9 mm². The wire is isolated with *Kapton* and the windings are fixed onto the holder using *Araldite* during the winding process. This results in a distance of 0.8 mm to 1 mm between each layer and each winding which we incorporated in the simulation of the drafts. We also have to take into account in the design process that it must be technically possible to actually wind a theoretical coil design in a single continuous winding process without interruptions. The current connectors and water connectors are soldered on the wires. The current connector is a copper plate with a hole in its center with a diameter of 11 mm. The water connector is a *Swagelok SS-8M0-1-2W*.

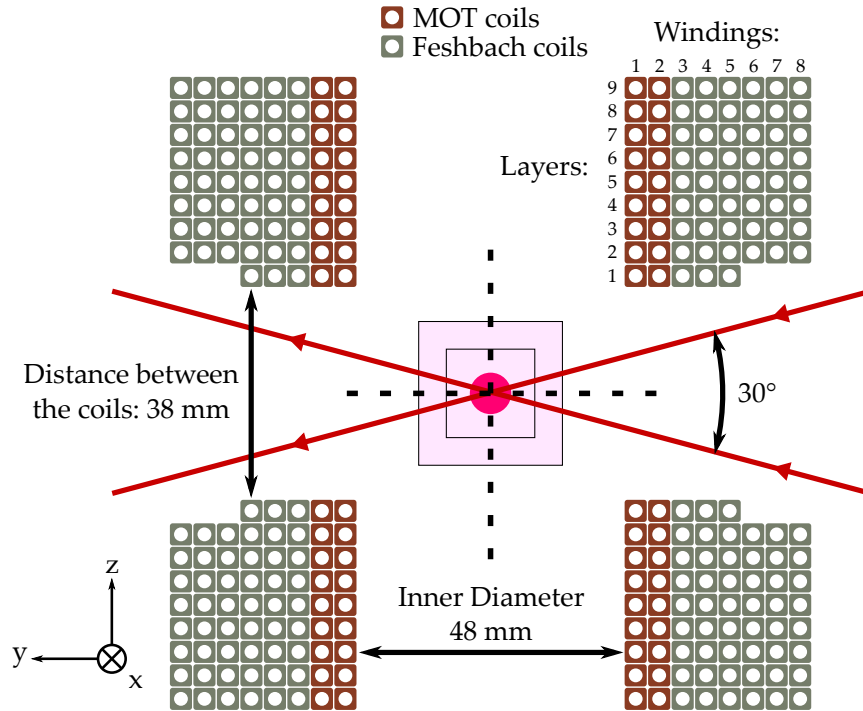


FIGURE 4.1: Draft for the simulation and production of the MOT coils and Feshbach coils. In addition we display the glass cell, the 3D-MOT and the two laser beams of the accordion lattice along the z-axis. The center of both coil pairs which is marked with the two black dotted lines must overlap with the position of the atomic cloud. The missing windings 6, 7 and 8 of the first layer guarantee a full crossing angle between the lattice laser beams of at least 30°.

Figure 4.1 shows the draft of the MOT coils and the Feshbach coils. The windings of the Feshbach coils are positioned such that they fulfill the geometric condition for a Helmholtz coil as good as possible while creating enough magnetic field and matching the given spatial restrictions. The windings 6, 7 and 8 are left out for the first layer so that a full opening angle of at least 30° for the two laser beams of the accordion lattice without clipping at the coils is assured.

The MOT coils are placed closer to the atoms which results in a higher magnetic field per winding. Naturally their windings differ more from the geometry of a Helmholtz coil than the windings of the Feshbach coils. In consequence their homogeneous magnetic field created in Helmholtz configuration has a higher residual curvature than the field of the Feshbach coils. In anti-Helmholtz configuration both coil pairs create a gradient field at the position of the atoms.

In figure 4.2 the draft of the Tilt coil is displayed. The first layer of the Tilt coil can only be placed in a relatively large distance to the atoms of 70 mm because it otherwise would collide with the MOT coils and the Feshbach coils. This results in a rather low offset field and gradient per winding which can only be compensated with a higher number of windings. Luckily there is enough room at this position of the experimental setup to place there a large coil with 98 windings. The stair like arrangement of the outer windings assures enough place for the MOT beams and their optomechanics. The windings 1 and 2 are left out for the layers 7 to 11 to keep

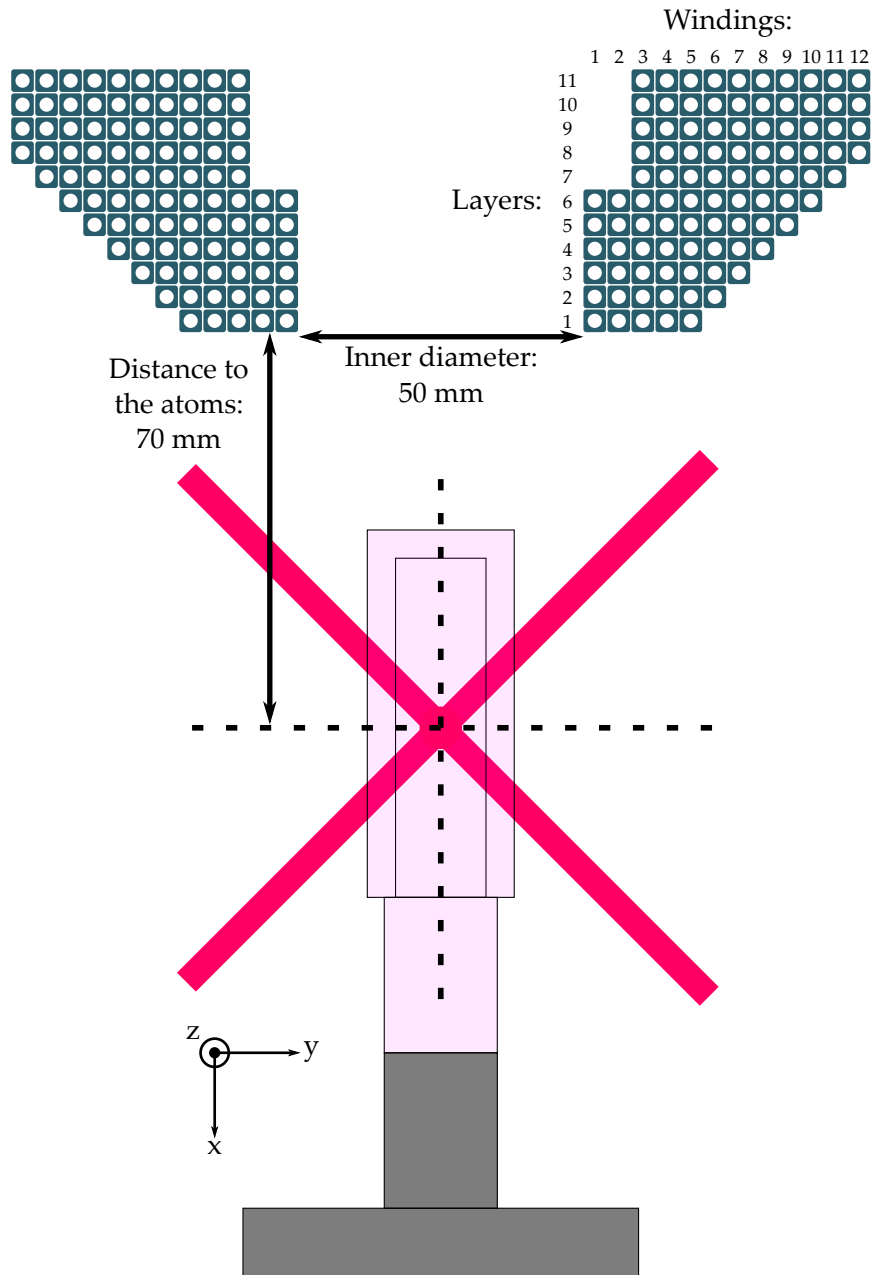


FIGURE 4.2: Draft for the simulation and production of the Tilt coil. The Tilt coil is placed on the opposite site of the flange that attaches the glass cell to the vacuum chamber. A higher number of windings is needed for this coil because it is relatively far away from the position of the atoms. The arrangement in stair form of the outer windings avoids clipping of the horizontal 3D-MOT beams at the Tilt coil and the missing layers 7 to 11 of the first two windings enable that the outcoupler of the triangular lattice laser beam along the x-axis can be placed closer to the glass cell.

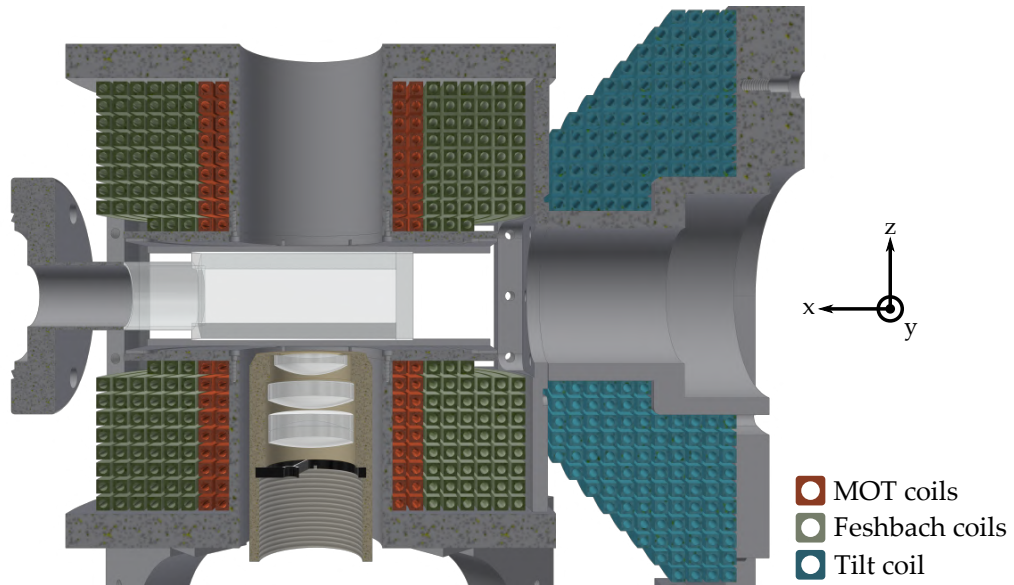


FIGURE 4.3: A vertical cut through a part of the experimental setup to show the MOT coils, the Feshbach coils and the Tilt coil in their final position at the experiment. The glass cell and the high-resolution objective that needs to be placed very close to the glass cell are also displayed. Figure adapted from [18].

free the space for the optomechanics of the triangular lattice laser beam on this axis. All coils in their final position in the experiment can be seen in the mechanical drawing in figure 4.3. The holder of the MOT coils and Feshbach coils leaves enough space for the glass cell and the high-resolution objective which must be placed directly underneath the glass cell. The holder of the Tilt coil is attached to the holder of the two coil pairs.

4.2.4 Measurement of the coil properties

The company *Oswald* that builds the coils also characterizes some of their properties namely for each individual coil the resistance, the inductance at 1 kHz and the water flow rate at a pressure of 4.5 bar. In addition they check the electrical isolation at 500 V and water leak tightness at 15 bar.

These mechanical and electrical properties of the coils are shown in table 4.1. The resistance of the coils and the resulting voltage drop and power consumption match our calculations as expected. The water cooling of the coils should be sufficient because the power consumption is comparably low and the water flow rate is relatively high compared to other experiments working with ultracold lithium.

The measured inductance is slightly lower for each individual coil than the values that we calculated with *FEMM* but in qualitatively good agreement. The calculated inductance of a coil pair is slightly higher than the sum of the inductance of the single coils due to mutual inductance between the coils but this does not significantly change the achievable switching times of the coils.

We check the accuracy of our simulation for the resulting magnetic field of the coils with a Hall sensor before the coils are installed. This measurement is not very precise

TABLE 4.1: Mechanical and electrical properties of the two coil pairs and the single coil.

	MOT coils	Feshbach coils	Tilt coil
Windings	18	52	98
Resistance	6.2 m Ω	24.1 m Ω	50.1 m Ω
Voltage drop at 200 A	1.2 V	4.8 V	10.0 V
Power consumption at 200 A	250 W	960 W	2000 W
Inductance at 1 kHz	12 μ H	160 μ H	500 μ H
Water flow rate at 4.5 bar	0.91/min	0.41/min	0.21/min

because the Hall sensor can have a systematic error and we can not determine the exact position of the sensor but we are able to see that simulation and measurement agree at least within 1 % which is more than good enough to install the coils without any concerns. A precise characterization of the magnetic fields can be done at a later point by performing RF spectroscopy on the atoms.

We are able to observe an oscillation of a molecular BEC of ^6Li atoms in the residual curvature of the magnetic field of the Feshbach coils along the radial direction in a ToF measurement when the final position of the optical dipole trap at the end of the evaporative cooling stage differs from the position of the center of the Feshbach coils (see section 5.2.1). The frequency of this oscillation agrees with the simulated trap frequency of the residual curvature of the Feshbach coils within $\sim 10\%$ [96].

4.2.5 Magnetic field configurations

After describing the process of designing and building the two coil pairs named MOT coils and Feshbach coils and the single coil named Tilt coil we now discuss in more detail the configurations that can be realized with on the one hand a single coil or coil pair and on the other hand by combining the single coil and the coil pairs in different ways. The electromagnetic properties of the MOT coils and Feshbach coils which are listed in table 4.2 and which we consider from now on are the results of our simulation because up to now we have only done some tests to assure the validity of the simulations but we did not map out the different configurations experimentally.

MOT coils

The MOT coils as their name suggests are used in anti-Helmholtz configuration to create the gradient field for the 3D-MOT. The maximum gradient that can be created with them is 180 G/cm which is far more than is needed for the normal 3D-MOT. Homogeneous magnetic fields around 300 G are often used to evaporative cool fermionic ^6Li atoms and create a degenerate Fermi gas in this way. In Helmholtz configuration the MOT coils produce a homogeneous field of up to 362 G. Therefore,

TABLE 4.2: Magnetic field strength in Helmholtz and anti-Helmholtz configuration and residual curvature in Helmholtz configuration of the MOT coils and the Feshbach coils. The trap frequency of the residual curvature scales with the square root of the magnetic field which has to be inserted in units of gauss.

	MOT coils	Feshbach coils
Homogeneous field in Helmholtz mode	1.81 G/A	5.86 G/A
Gradient field in anti-Helmholtz mode	0.90 G/(cm A)	1.71 G/(cm A)
Curvature in Helmholtz mode along z	$2\pi \times 2.39 \text{ Hz} \cdot \sqrt{B}$	$2\pi \times 1.25 \text{ Hz} \cdot \sqrt{B}$
Curvature in Helmholtz mode along x,y	$2\pi \times 1.69 \text{ Hz} \cdot \sqrt{B}$	$2\pi \times 0.89 \text{ Hz} \cdot \sqrt{B}$

they could also be used for this task. At a magnetic field of 300 G they create a trapping residual curvature of $\omega_r = 2\pi \times 29.3 \text{ Hz}$ for high-field seekers in the radial direction of the coil pair and in the axial direction they create an anti-trapping residual curvature of $\omega_z = 2\pi \times 41.4 \text{ Hz}$ for high-field seekers.

Feshbach coils

The Feshbach coils can address all Feshbach resonances that are imaginable in our experiment. In Helmholtz configuration they create a magnetic field of up to 1172 G which is 100 G more than the benchmark of 1067 G that we discussed in section 4.2.1. The Feshbach coils produce less residual curvature per magnetic field strength than the MOT coils. Hence the most homogeneous magnetic field is created by using only the Feshbach coils. We often perform evaporative cooling of fermionic ${}^6\text{Li}$ atoms at 810 G. At this magnetic field, which is shown in figure 4.4, the trapping residual curvature for high-field seekers in the radial direction is $\omega_r = 2\pi \times 25.3 \text{ Hz}$ and the anti-trapping residual curvature for high-field seekers in the axial direction is $\omega_z = 2\pi \times 35.6 \text{ Hz}$.

In anti-Helmholtz configuration the maximum gradient of the Feshbach coils is 342 G/cm. In [63] a highly compressed MOT with a gradient of 250 G/cm is used to collect the fluorescence of an ensemble with 1 to 10 fermionic ${}^6\text{Li}$ atoms and determine the number of atoms in the sample by the amount of fluorescence that is detected. If we want to implement this detection method for the atom number in a system with only a few particles in our experiment, our MOT coils might not be able to create a sufficiently high gradient but the Feshbach coils are suitable for this task.

Combination of the MOT coils and Feshbach coils

The highest magnetic bias fields and gradients can be realized by combining the MOT coils and Feshbach coils in the same configuration. In Helmholtz configuration the maximum magnetic field is 1534 G and in anti-Helmholtz configuration the maximum gradient is 522 G/cm. But it can also be beneficial to run both coils in

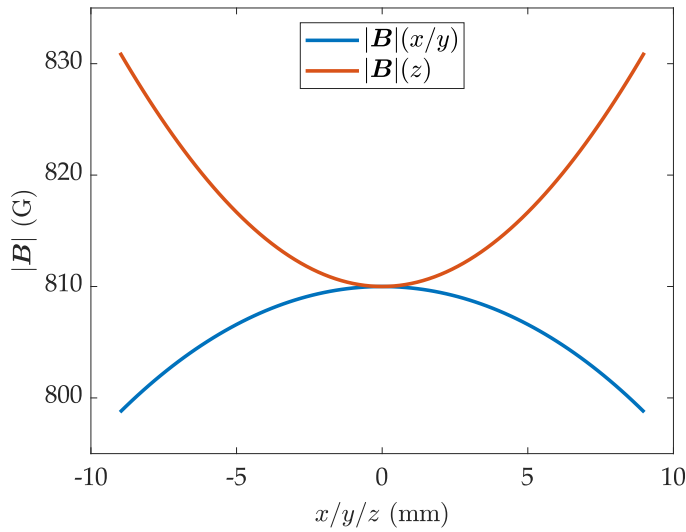


FIGURE 4.4: Simulated magnetic field of 810 G created by running the Feshbach coils in Helmholtz configuration with a current of 138.2 A. Around the center of the coil pair the magnetic field is reasonably homogeneous for such a high value. The residual curvature is trapping for high-field seekers along the x - and y -axis (blue) which corresponds to the radial plane of the coil pair and it is anti-trapping for high-field seekers along the z -axis (orange) which is the axial direction of the coil pair. The curvature in the axial direction is twice as high as in the radial direction due to symmetry reasons which leads to a trap frequency in the axial direction that is a factor of $\sqrt{2}$ larger than in the radial direction.

different modes. When we for example run the Feshbach coils in Helmholtz configuration and the MOT coils in anti-Helmholtz configuration during evaporation in the optical dipole trap both coils can improve the efficiency of the evaporation [107, 120]. The Feshbach coils address the Feshbach resonance to enhance the scattering length of the atoms and the MOT coils create an additional gradient which enforces the hottest atoms to fall out of the trap. The resulting magnetic field is shown in figure 4.5 (a).

Another possibility is the so called anti-curvature mode. In this case both coil pairs are run in Helmholtz configuration but the current is flowing in opposite directions in the two coil pairs. The advantage of this mode is that the residual curvature of the magnetic field of the coil pairs compensate each other. The disadvantage is that the field strength of one coil also gets compensated by the other coil in this case. Therefore, we now show how to adjust the two coil pairs to get a resulting magnetic field of 810 G with no significant curvature using the anti-curvature mode. As there is a fixed factor of $\sqrt{2}$ between the axial and radial trap frequency of the curvature for both coil pairs (see section 4.2.2) we only have to consider one direction to get compensation of the curvature along all directions. We set the condition that the axial trap frequency shall be the same for MOT coils (MC) and Feshbach coils (FC) and insert the corresponding values from table 4.2:

$$\omega_{z,MC} = \omega_{z,FC} \iff 2.39 \text{ Hz} \cdot \sqrt{B_{MC}} = 1.25 \text{ Hz} \cdot \sqrt{B_{FC}} \quad . \quad (4.5)$$

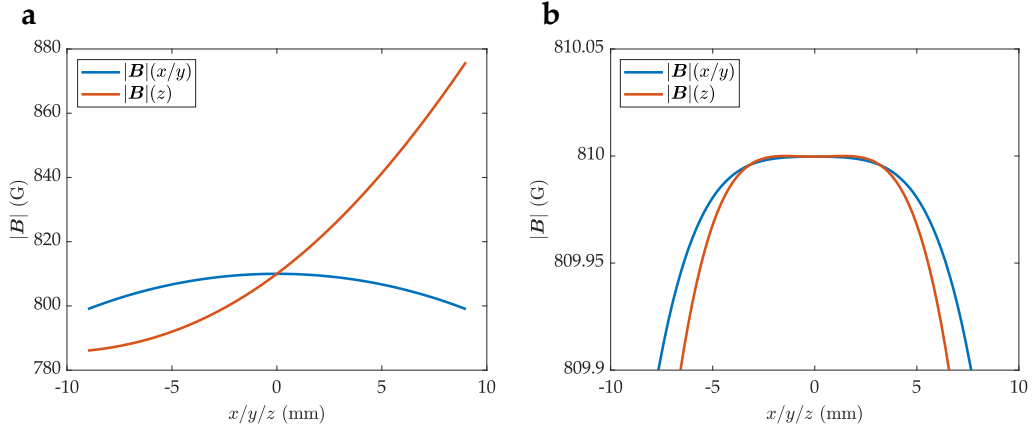


FIGURE 4.5: Combining Feshbach coils and MOT coils in different configurations. (a) The Feshbach coils in Helmholtz configuration create a bias field of 810 G and the MOT coils in anti-Helmholtz configuration create an additional gradient of 50 G/cm. The field of the Feshbach coils only has a component in z-direction. Thus, the resulting field of both coil pairs has a gradient of 50 G/cm along the axial direction and along the radial direction there still is only a residual curvature. The bias field in the center of the coil pairs remains at 810 G. (b) Anti-curvature mode: With the Feshbach coils again in Helmholtz configuration the MOT coils are also run in Helmholtz configuration but the current flows in the opposite direction than in the Feshbach coils. The current through both coil pairs is chosen such that the resulting field at the position of the atoms is 810 G but the residual curvature vanishes for a rather large area around the center along all directions.

As the magnetic fields of the two coil pairs are compensating each other we have to add the field of the MOT coils to the 810 G that shall be the resulting field to get the field that the Feshbach coils have to realize:

$$2.39 \text{ Hz} \cdot \sqrt{B_{MC}} = 1.25 \text{ Hz} \cdot \sqrt{810 \text{ G} + B_{MC}} \quad . \quad (4.6)$$

Now we can solve this equation for the magnetic field of the MOT coils B_{MC} :

$$B_{MC} = \frac{810 \text{ G}}{\left(\frac{2.39 \text{ Hz}}{1.25 \text{ Hz}}\right)^2 - 1} = 305 \text{ G} \quad . \quad (4.7)$$

We now also get the needed field of the Feshbach coils B_{FC} directly via

$$B_{FC} = 810 \text{ G} + B_{MC} = 810 \text{ G} + 305 \text{ G} = 1115 \text{ G} \quad . \quad (4.8)$$

When we calculate a needed magnetic field we always get the corresponding currents that we have to send through the coils from table 4.1. When we insert the calculated values for the magnetic field of the MOT coils and the Feshbach coils into our simulation we get the resulting field that is shown in figure 4.5 (b). The value in the center is 810 G and there is practically no residual curvature around the center as we expect it from the shown calculation.

TABLE 4.3: Magnetic field of the Tilt coil at the position of the atoms. The trap frequency of the residual curvature along y - and z -direction at the position of the atoms scales with the square root of the magnetic field which has to be inserted in units of gauss.

Tilt coil	
Offset field	1.13 G/A
Gradient field along x	0.27 G/(cm A)
Curvature along y,z	$2\pi \times 0.72 \text{ Hz} \cdot \sqrt{B}$

Tilt coil

If current is flowing through the Tilt coil it always creates both a gradient and an offset field at the position of the atoms. The simulated electromagnetic properties of the Tilt coil are shown in table 4.3. At a maximum current of 200 A the offset field of the Tilt coil is 225.7 G and the gradient is 54.5 G/cm at the position of the atoms. In the experimental sequence we shortly turn on the Tilt coil during the compressed MOT phase to shift the atomic cloud into the direction of the vacuum chamber (see section 5.1.2). This leads to a better overlap between the gray molasses and the optical dipole trap.

But the Tilt coil was added initially to be able to break the radial symmetry of the two coil pairs. As discussed in section 2.2.3 creating an ultracold 2D sample for quantum gas microscopy requires to be able to evaporatively cool the sample again after it was loaded into a single plane of the vertical optical lattice. In addition to lowering the power of the optical lattice a magnetic field gradient needs to be added in the radial direction to make this evaporation work. This is exactly what the Tilt coil does.

Combination of the Tilt coil and a coil pair

For the evaporation of a single plane of the vertical optical lattice an offset field that is high enough for efficient evaporation needs to be generated in addition to the gradient along a horizontal direction. If the offset field of the Tilt coil is not high enough we can add for example the Feshbach coils in Helmholtz configuration to increase the offset field. Unfortunately this also leads to a decrease of the resulting magnetic gradient along the x -direction at the position of the atoms.

To exemplify this we now discuss three realistic cases: We first consider the situation that we want to evaporate at an offset field of 300 G to create a degenerate Fermi gas in a single plane of the vertical optical lattice. When a homogeneous bias field of the Feshbach coils in Helmholtz configuration of 197.6 G is added to the Tilt coil at the maximum current of 200 A the result is an offset field of 300 G and a gradient of 40.4 G/cm along the x -direction at the position of the atoms. This case is shown in figure 4.6. Secondly we look at the situation that we want to completely turn off the

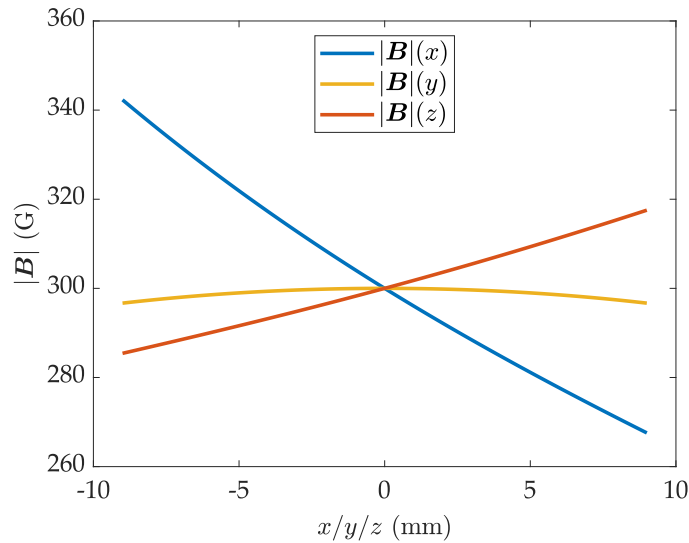


FIGURE 4.6: Resulting magnetic field of the combination of the Feshbach coils in Helmholtz configuration and the Tilt coil. The Tilt coil is supplied with the maximum current of 200 A and the bias field of the Feshbach coils is chosen such that the resulting offset field at the position of the atoms is 300 G. The Tilt coil breaks the radial symmetry of the Feshbach coils which results in a residual curvature of the magnetic field along the y -axis and a gradient of 40.4 G/cm along the x -axis. Even though neither the Feshbach coils in Helmholtz configuration nor the Tilt coil create a gradient along the z -axis, the resulting field of both actually has a gradient of 17.7 G/cm along the z -axis. However, for the application discussed in the main text this gradient is negligible compared to the strong confinement of the accordion lattice in this direction.

interaction between the particles by tuning the offset field to the zero crossing of the Feshbach resonance of ${}^6\text{Li}$ at 523 G. With the Tilt coil again at maximum current a bias field of 471.8 G must be created with the Feshbach coils to realize a total field of 523 G and a remaining gradient of 23.2 G/cm along the x -axis is achieved. In [63] a magnetic field of 523 G and a gradient of 18.9 G/cm are used for the deterministic preparation of small atom numbers. So we are able to realize the same configuration for spilling a single plane of the vertical optical lattice. And finally to realize again evaporation near the Feshbach resonance at 810 G, an offset field of 777.9 G has to be added with the Feshbach coils. The gradient along the x -axis becomes 15.0 G/cm in this case.

In addition to a homogeneous bias field by one of the coil pairs the magnetic field of the Tilt coil can also be combined with the magnetic gradient field of a coil pair in anti-Helmholtz configuration to modify the magnetic trap that is created by the coil pair. Even though we probably do not need a magnetic trap for ${}^6\text{Li}$ they are still common in experiments working with ${}^7\text{Li}$ [107] to be able to create large BECs without having very long experimental cycle times. For this setup the resulting magnetic field depends on the direction of the current through the Tilt coil. Both cases are shown in figure 4.7. For all displayed curves the MOT coils in anti-Helmholtz configuration are creating a gradient of 100 G/cm along the z -direction and accordingly a gradient of 50 G/cm along the x - and y -direction.

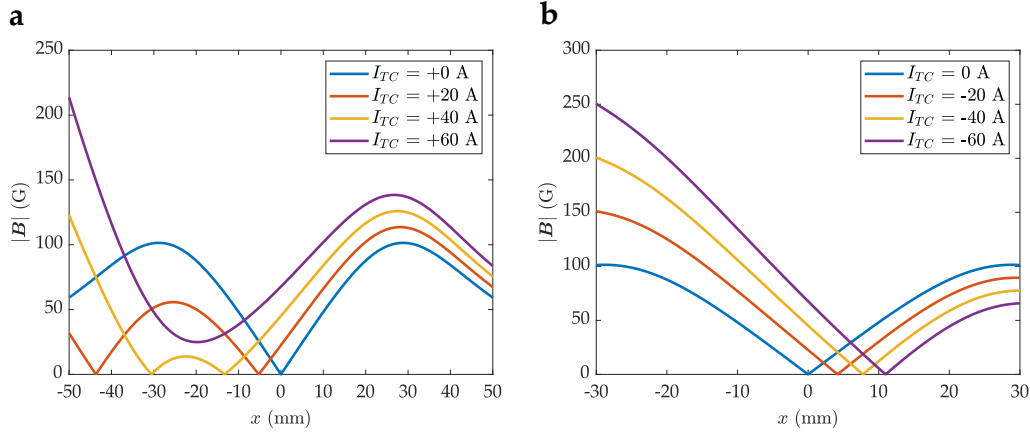


FIGURE 4.7: Combining the Tilt coil with a gradient field of 50 G/cm along the horizontal x -direction created by the MOT coils in anti-Helmholtz configuration. The resulting magnetic field is shown for increasing (a) positive and (b) negative currents through the Tilt coil. (a) A QUIC trap with a non-zero minimum develops which is shifted along the negative x -direction from the center of the MOT coils. (b) The minimum of the magnetic trap which stays at zero magnetic field gets shifted along the positive x -direction. In addition both resulting magnetic fields are slightly asymmetrical because the Tilt coil breaks the radial symmetry of the MOT coils.

For positive currents through the Tilt coil a magnetic field configuration can be created that is called QUIC trap [114] because it incorporates the quadrupole and the Ioffe configuration. Figure 4.7 (a) shows the onset of a QUIC trap for increasing current through the Tilt coil. For $I_{TC} = 60$ A a new magnetic trap with a non-zero minimum has developed. The atoms could be initially captured in the magnetic trap that is created by only the MOT coils and could then be transferred into the QUIC trap by ramping up the current through the Tilt coil. In the QUIC trap they can be evaporatively cooled without suffering from Majorana losses which occur in magnetic traps with a magnetic field zero [121]. A disadvantage of the QUIC trap is that the atoms move significantly along the x -direction during the transfer to the QUIC trap. In our setup the minimum of the QUIC trap is created ~ 20 mm away from the center of the coils. So we would have to transfer the atoms back to the center of our setup after the evaporation.

If we send a negative current through the Tilt coil the magnetic trap of the MOT coils in anti-Helmholtz configuration stays a trap with a magnetic zero in its center but the center of the trap is shifted. As it can be seen in figure 4.7 b a negative current of 60 A through the Tilt coil already creates a shift of more than 10 mm along the x -direction. This might be a useful feature in some situations. The shift in this configuration is along positive x -direction while the minimum of the QUIC trap is shifted in negative x -direction compared to the center of the MOT coils. If we create a magnetic gradient field with opposite sign by changing the current direction in both MOT coils we get the described configurations along the respective opposite x -direction.

TABLE 4.4: Magnetic field of all offset coil pairs at the position of the atoms in Helmholtz and anti-Helmholtz configuration. These values were measured in a separate test setup [122]. Data taken from [18].

	anti-Helmholtz (mG / (cm A))	Helmholtz (mG / A)
x-axis		
yellow	76	260
red	72	206
black	74	292
y-axis		
yellow	98	488
red	100	496
black	108	494
z-axis		
yellow	260	840
red	300	1040
black	320	1300

4.3 Offset coils

Magnetic stray fields at the position of the atomic cloud are in general a disturbing factor in experiments with ultracold atoms. Some of the experimental steps, for example the gray molasses, are sensitive to even small deviations of the magnetic field. For a gray molasses with a good performance all magnetic stray fields must be compensated to zero as good as possible. This can be done with pairs of so called compensation or offset coils in all spatial directions. They are used to compensate magnetic offset and gradient fields by running them in Helmholtz and anti-Helmholtz configuration. The need for at least one coil pair in all three spatial directions and the typical spatial restrictions of a cold atom experiment often limit the possibility of building these coils in the geometric configuration of a Helmholtz coil which would be favorable because a Helmholtz coil creates the most homogeneous field for compensation. Some experiments face these challenge by building very large offset coils with a lot of windings that are quite far away from the position of the atoms.

Our offset coils are placed very close to the glass cell with the compromise of less control over their geometric shape. Their making and characterization is described in more detail in [18]. There are three coil pairs in each spatial direction labeled with the colors black, red and yellow. All pairs can be supplied independently in Helmholtz and anti-Helmholtz configuration which is important for compensation of offset fields and gradients in one direction at the same time. They are supplied by a programmable power supply that is addressed by our experimental control for

dynamical tuning of the offset fields. In addition MOSFETs are implemented for fast switching of the offset fields. The magnetic field of all offset coils at the position of the atoms in both configurations was measured with a Hall sensor in a separate test setup. The results are shown in table 4.4. We limit the maximum current for each coil pair to 5 A to avoid too much ohmic heating.

There are different sources of magnetic stray fields in the laboratory. An omnipresent stray field is the geomagnetic field. It is of course very homogeneous on our length scales and can therefore be compensated well. In central Europe its absolute value is approximately 500 mG which can easily be compensated with our offset coils. Some devices in the laboratory also create stray fields, for example current transducing cables or the magnets of the ion getter pumps that are attached to the vacuum chamber and hence quite close to the atoms. The permanent magnets that create the magnetic field for the 2D-MOT also lead to a stray field at the position of the 3D-MOT. This stray field can not be compensated with the offset coils because of its specific form [98].

A magnetic gradient field that is created by the offset coil pairs along the vertical direction can also be used to compensate gravity and levitate the atoms in this way. For simplicity we consider again only high-field seeking states in the Paschen-Back regime to calculate the magnetic gradient that is needed to levitate the atoms:

$$E(z) = m_{atom} g z = \mu_B \frac{dB}{dz} z \iff \frac{dB}{dz} = \frac{m_{atom} g}{\mu_B} , \quad (4.9)$$

with m_{atom} being the mass of the respective atom, μ_B being the Bohr magneton and g being the gravity of earth. The needed gradients for levitation of the atomic isotopes that could be cooled in our vacuum chamber, are 1.06 G/cm for ${}^6\text{Li}$, 1.23 G/cm for ${}^7\text{Li}$, 14.91 G/cm for ${}^{85}\text{Rb}$ and 15.26 G/cm for ${}^{87}\text{Rb}$. Hence the lithium isotopes can be levitated using the offset coils. For the rubidium isotopes we would have to use the MOT coils or the Feshbach coils in anti-Helmholtz configuration to create the required gradient. In our experiment we did not notice the influence of gravity on the lithium atoms so far because of the fast time scales of lithium due to its light mass. In experiments with the much heavier rubidium atoms the influence of gravity is clearly visible in ToF measurements.

4.4 High currents and water cooling

In this section we describe how to supply currents of up to 200 A and sufficient water cooling for our coils. We start with some of the basic infrastructure for high currents including suitable power supplies, cables and connectors. Then we discuss the components and the circuits that are needed to switch the high electrical power that is running through the inductive coils fast and safely. Finally we specify the infrastructure that we set up for efficient water cooling of the coils which would otherwise heat up enormously and cause vast damage to the experimental apparatus.

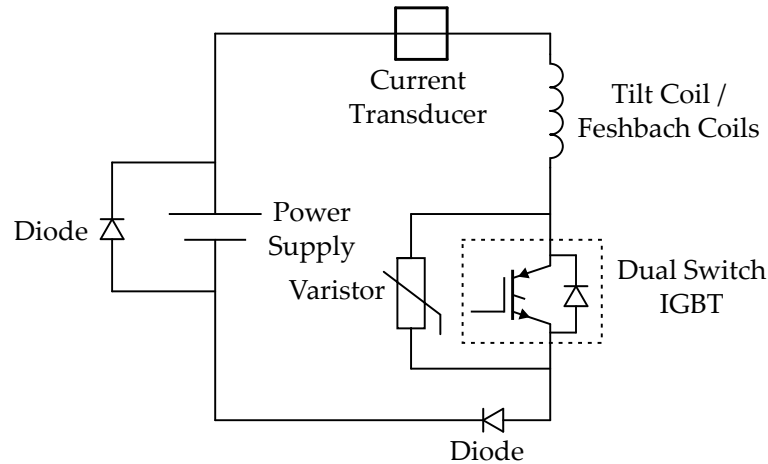


FIGURE 4.8: Circuit for switching the current through the Feshbach coils and the Tilt coil. For the Feshbach coils both coils are connected in series with the same current direction to realize the Helmholtz configuration.

4.4.1 Infrastructure for high currents

We now have a look at some of the basic infrastructure for supplying high currents before we describe in detail the circuits for switching these currents. The power supplies³ that we use have a maximum voltage of 30 V and a maximum current of 200 A and hence a total electric power of 6 kW. There are three of these devices in our experiment to independently supply the MOT coils, the Feshbach coils and the Tilt coil. The power supply that is connected to the Feshbach coils has a built-in option to actively control the current ramps of the power supply with a feedback loop. The feedback is provided by a current transducer that measures the current in the circuit and feeds it back to the power supply. We show the influence of the active control on the switch-on behavior of the Feshbach coils in section 4.4.3.

We use very flexible cables⁴ that are molded with silicone to connect the power supplies with the coils. They have a large conducting cross-section of 120 mm², consisting of 15,435 litz wires with a diameter of 0.1 mm each, to avoid too much ohmic heating and loss of electric power in the cables. The connectors are tinned tube crimping lugs made out of copper with a through boring for either a M6, M8 or M10 screw. We use tubes with a flat flange⁵ or a 90° angled flange⁶ to match the given spatial restrictions for placing the connectors. Current transducers⁷ are implemented in the circuits of all three power supplies to monitor the current and to analyze the switching times of the coils without disturbing the circuits.

4.4.2 Switching high currents

The electronic components that are used for switching the currents and for protection against high induction voltages are placed on an aluminum board underneath the optical table of the vacuum chamber. The board is cooled with water running through copper tubes that are integrated into the aluminum board. We now discuss the purpose of all components by explaining the circuit for the Feshbach coils and the Tilt coil that can be seen in figure 4.8. The circuit is in principal the same for both but for the Feshbach coils both coils are connected in series to realize the Helmholtz configuration. This means that we are not able to switch the Feshbach coils between Helmholtz and anti-Helmholtz configuration at the moment but we could implement this at any time.

All diodes⁸ in all circuits are the same model which is suitable for currents of up to 600 A and which has a voltage drop of at most 1.5 V. They are installed to protect the power supplies against high voltages in the opposite direction that can build up when a high current through an inductive coil is switched off.

We use insulated-gate bipolar transistors (IGBTs) to switch the currents. All IGBTs are the same model which is a dual switch IGBT⁹. Dual switch IGBTs are more common than single switch IGBTs and therefore less expensive but they also have more possible applications. This dual IGBT has a maximum emitter current of 450 A, the maximum voltage drop over of the IGBT is 2 V and the damage threshold voltage between collector and emitter is 1200 V. In such a dual switch IGBT there is one channel for each current direction. Both channels are protected with an internal diode connected in parallel. Hence two dual IGBTs are sufficient to build an H-bridge for switching the polarity of the current that is flowing through a coil. In the circuits of the Feshbach coils and the Tilt coil we only use one channel of the dual IGBT to switch the currents through the coils on and off.

The housing of the IGBT is designed such that a corresponding commercial IGBT gate drive unit¹⁰ can be soldered directly onto the IGBT. The gate resistors have to be added by the user. Although according to the data sheet a 2 Ω resistor should be sufficient we made the experience that we destroyed either the gate or the protection diode inside the IGBT when we switched off a high enough current with such a low gate resistance implemented in the gate drive unit. We ended up using 1 k Ω resistors to be able to safely switch currents on and off without destroying the IGBT. We also had to insert two optional capacitors on the gate drive unit to be able to switch the IGBT when the full 30 V of the power supply are already turned on before the start of switching the IGBT.

³Delta Elektronika: SM30-200

⁴Druseidt Elektrotechnik: order number 03972

⁵Druseidt Elektrotechnik: order numbers 10866 (M6), 10867 (M8), 10868 (M10)

⁶Druseidt Elektrotechnik: order numbers 03972 (M6), 03973 (M8), 03974 (M10)

⁷LEM: HTA600-S

⁸Semikron: SKKE 600

⁹Mitsubishi Electric: CM450DX-24T

¹⁰Isahaya Electronics Corporation: VLA536-01R

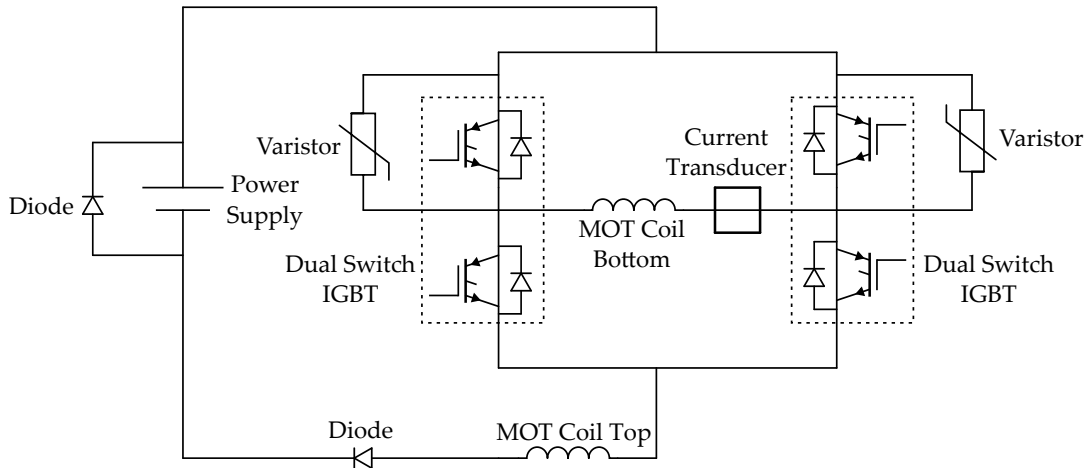


FIGURE 4.9: Circuit for switching the current through the MOT coils. An H-bridge for the bottom MOT coil enables dynamical switching between Helmholtz and anti-Helmholtz configuration.

A varistor¹¹ is connected in parallel to every dual IGBT. Varistors are voltage-dependent resistors without a preferred current direction. Varistors have a very high resistance under their respective threshold voltage and therefore nearly no current is flowing through them. At the threshold voltage their resistance drops down and current begins to flow through them. The varistor that we use has a threshold voltage of 550 V and at a current of 200 A the voltage drop over the varistor is a bit above 800 V.

The varistor protects the IGBT against the induction voltage that is created by the inductive coil when the IGBT is switched to turn off the current. The coil keeps up the voltage that is necessary to let the remaining current in the coils flow through the varistor until there is no electrical energy left in the coil. Therefore a higher varistor voltage allows faster switching of the current because the electrical energy is removed faster from the coil. At the same time the varistor voltage at the maximum possible current has to be lower than the damage threshold voltage of the IGBT of 1200 V. These constraints lead to the choice of the varistor that we use in the circuits for the coils.

The circuit for the MOT coils that is displayed in figure 4.9 has an H-bridge to switch the direction of the current through the bottom MOT coil. Hence, we are able to switch the MOT coils dynamically between Helmholtz and anti-Helmholtz configuration. In the present configuration the MOT coils in Helmholtz configuration would enhance the magnetic field of the Feshbach coils in Helmholtz configuration instead of realizing the so called anti-curvate mode (see section 4.2.5) but we can change this quickly any time. We could also add an H-bridge for the top MOT coil. Then we would be able to dynamically switch between all possible magnetic field configurations of the MOT coils.

¹¹TDK Electronics: B40K320

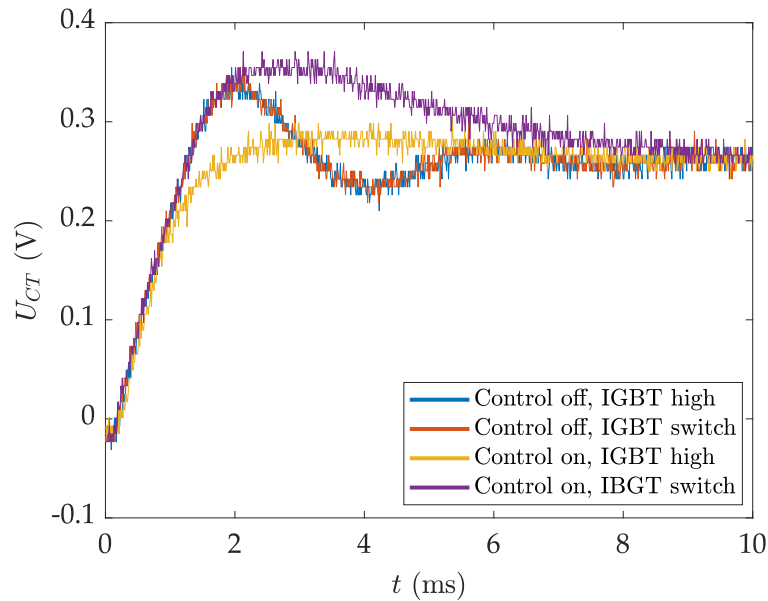


FIGURE 4.10: Switch-on behavior of the Feshbach coils when a current of 80 A is ramped up. The current in the coils is measured with a current transducer. We analyze the influence of the active control inside the power supply and of the moment when the IGBT is switched on. The smoothest switch-on behavior can be observed if the control is activated and the IGBT is switched on before the power supply starts to ramp up the current.

4.4.3 Active current control

We now discuss the influence of the active current control that is implemented in the power supply of the Feshbach coils when we switch on a current of 80 A. The active control is adjusted to this current and to the inductivity of the Feshbach coils but the parameters of the control can be adjusted to also get the best possible result for other current values. As we just described the inductive coils can be turned off quite fast using the high voltage values of varistors but the needed time to switch on a coil is limited due to the maximum voltage of 30 V that can be created by the power supply that we use. The switch-on time can be reduced by using the power of charged capacitors for a short moment during the switching process but we have not implemented this method in our setup so far.

In figure 4.10 we show the switch-on behavior of four different scenarios. For this purpose we monitor the current in the Feshbach coils with the mentioned current transducer on an oscilloscope. “IGBT high” means that the IGBT of the Feshbach coils is already switched on before the power supply starts to ramp up the current. “IGBT switch” means that the power supply is already tuned to the aspired current value and that the switch-on process starts by switching the IGBT. We combine this two setups with the current control being activated and being not activated.

When the active control is turned off we see no influence of the IGBT on the switch-on behavior. The current in the Feshbach coils clearly oscillates for several milliseconds before it reaches a stable state after roughly 6 to 8 ms. When the current control is turned on and the switch-on process is started by the IGBT the current overshoots its desired value and it takes even longer until the final value is reached even though

there are no oscillations. The best result is achieved when the active control is turned on and the IGBT is switched on before the current ramp is started by the power supply. The overshoot is significantly smaller than in all other configurations and if small deviations from the final value are acceptable, then the current through the Feshbach coils can be considered to be relatively stable already after ~ 3 ms.

4.4.4 Infrastructure for water cooling

Several devices in our experiment have to be cooled actively. Fans often cool not efficient enough and moreover they create noise and vibrations. Therefore, water cooling is implemented on several occasions even though it is always accompanied by the risk of leaks and resulting water damages.

Two different approaches of water cooling are implemented for our experiment. The first is direct cooling of several devices using the closed cooling water cycles that are available in every laboratory of the facility. In this way beam dumps for high power lasers, the aluminum board for the IGBTs and the vacuum turbo pumps can be cooled. A custom made water distributor¹² with five channels is used to dispose the cooling water to the different devices. For every channel the water flow rate can be adjusted and monitored with floaters. In addition the floaters can act as the sensors for electrical flow sensors.

Secondly we use a custom made cooling unit¹³ to cool the MOT coils, the Feshbach coils and the Tilt coil. The cooling unit is placed in the soldering room of the research group next to our laboratory to avoid the vibrations of the cooling unit in the laboratory. The soldering room and the laboratory are connected via a hole in the wall. The cooling unit exchanges the heat between a closed secondary water circuit, where the water is pumped through the coils, and the house water.

The cooling unit has a tank volume of 100 l as a reservoir for the secondary circuit. It automatically controls the heat exchange to reach the desired temperature of the water in the tank which can be adjusted. The cooling power of the cooling unit is 6 kW, the pump power is 7 l/min at a pressure of 6.0 bar and the maximum pump pressure is 12.0 bar. In the secondary water circuit the water is again disposed with a custom made water distributor¹⁴ between the five coils. For this water distributor the floaters can not be used as flow sensors. Hence, additional flow sensors are installed in series.

In addition we install a filter in series¹⁵ in the secondary water circuit to avoid the growing of algae in the water. For the water we use a mixture of 70 l distilled water and 30 l tap water which should be exchanged from time to time. Especially the first filling of the tank gets contaminated with some dirt that resides from the manufacturing and installation process in different components of the secondary circuit. Up

¹²Van der Heijden Labortechnik: order number 99-100280

¹³Van der Heijden Labortechnik: order number 3-100626

¹⁴Van der Heijden Labortechnik: order number 99-100250

¹⁵Van der Heijden Labortechnik: order number 00500, 00501

to now a pump pressure of 3 bar has always been sufficient to keep a temperature of 21.0 °C in the secondary water circuit.

Chapter 5

Creation of ultracold lithium gases

This chapter is dedicated to the production of ultracold samples of ${}^6\text{Li}$ atoms either in the form of a molecular BEC or a degenerate Fermi gas. We first describe the initial experimental steps 2D-/3D-MOT, compressed MOT and gray molasses which are identical in both cases. Afterwards we discuss the different evaporative cooling and imaging steps that we implement to create either a molecular BEC or a degenerate Fermi gas. The ability to create quantum-degenerate samples is an important milestone in the process of building up the apparatus and the starting point for the following experimental steps.

The described experimental sequences were planned and implemented by a team consisting of Andreas Kerkmann, Mathis Fischer, Benno Rem and the author under the supervision of Klaus Sengstock and Christof Weitenberg. The displayed data were taken by the same team.

5.1 Initial laser cooling

The first step of the experimental cycle is the 2D-/3D-MOT phase. Before the start of the MOT the experimental sequence is initialized with a short timestep of 0.5 s to make some devices of the apparatus listen to the experimental control and to get the AOMs heated up quickly by the incoming laser power in order to reach a stable state for the start of the experimental run. Hence, the laser beams of the 2D-MOT, the 3D-MOT and the push beam are already turned on in this first timestep. The permanent magnets that create a magnetic field of 56 G/cm for the 2D-MOT can not be turned off and hence the 2D-MOT is running already. After this first step the MOT phase is actually started by rapidly ramping up a gradient of 41 G/cm for the 3D-MOT using the MOT coils in anti-Helmholtz configuration.

5.1.1 2D- and 3D-MOT

The two 2D-MOT beams, which are retro-reflected after their first pass through the steel chamber, are shaped elliptically with beam waist radii of 3 mm and 6 mm. The light of the cooler is red-detuned with -7.3Γ and the repumper is red-detuned with -3.4Γ , with $\Gamma = 2\pi \cdot 5.87\text{ MHz}$ being the natural linewidth of the D1 line and the

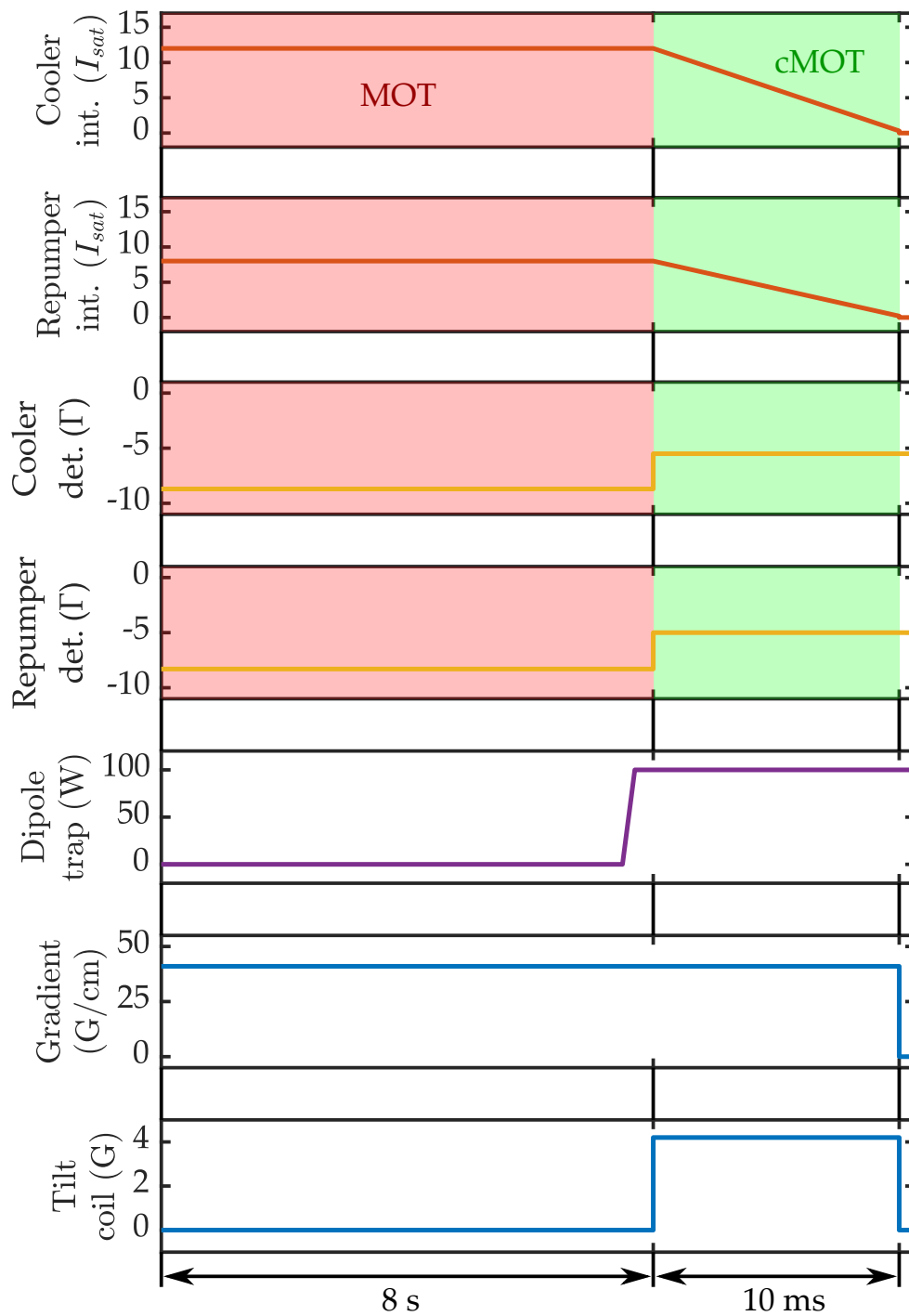


FIGURE 5.1: Timeline of the MOT and the compressed MOT phase. The traces show the intensities and the detunings of the 3D-MOT cooler and repumper light, the dipole trap power, the 3D-MOT gradient field and the magnetic field of the Tilt coil.

D2 line of ${}^6\text{Li}$. The peak intensities per 2D-MOT beam are $28 I_{sat}$ on the cooling transition and $20 I_{sat}$ on the repumping transition, with $I_{sat} = 2.54 \text{ mW/cm}^2$ being the saturation intensity of the D2 line of ${}^6\text{Li}$. Over time we have observed that the optimal detunings for the 2D-MOT cooler and repumper depend on the performance of the oven due to the changing temperature and location of the lithium inside the oven. When the performance of the first oven filling began to continuously decrease over time we were able to improve the loading rate a bit by changing the detunings. After refilling the oven we had to adjust the detunings again significantly to optimize the performance of the 2D-MOT.

The push beam, which supports the transport of the lithium atoms from the 2D-MOT in the steel chamber through the graphite tube to the 3D-MOT in the glass cell, has a peak intensity of $4.7 I_{sat}$ and a red-detuning of -3.9Γ . The addition of the push beam increases the loading rate of the 3D-MOT by approximately an order of magnitude. Adding a repumping transition to the push beam does not increase the loading rate for our experiment. In contrast we are not able to achieve the same loading rate using a repumper compared to the one that we get when we omit the repumper.

In the horizontal plane of the 3D-MOT the MOT beams are also retro-reflected after their first pass through the glass cell. Their beam waist radius is 5 mm and their peak intensity is $12 I_{sat}$ for the cooler and $8 I_{sat}$ for the repumper. Along the vertical direction there are two separate MOT beams. The intensity of cooler and repumper of the upper beam, which has a similar beam waist radius as the horizontal MOT beams, is approximately half as much as the intensity of the horizontal beams because the magnetic gradient of the MOT coils in anti-Helmholtz configuration is twice as high along the vertical direction compared to the horizontal plane. The lower oblique beam that passes through the objective (see section 3.6) is just slightly larger than the other MOT beams but it needs roughly as much power as the horizontal MOT beams to compensate for the incident angle and thus get a relatively round MOT again. All 3D-MOT beams have the same red-detunings which are -8.7Γ for the cooler and -8.3Γ for the repumper.

An analysis of the 3D-MOT loading rate in [18] shows that we get $\sim 3 \cdot 10^7$ atoms/s and a saturation of the particle number at $\sim 5 \cdot 10^8$ atoms. For our experimental cycles we typically have a MOT phase of 8 s (see figure 5.1) and end up with $\sim 10^8$ atoms.

The dipole trap laser is already switched on 0.5 s before the end of the MOT phase using the fast TTL switch of the laser. The power is ramped directly from minimum to maximum in 200 ms with a linear slope using the motorized rotation mount (see section 3.3). The presence of the dipole trap does not disturb the MOT or the gray molasses [83] due to the low differential polarizability of lithium atoms in the wavelength spectrum of the dipole trap [123]. By switching on the dipole trap already during the MOT phase we improve the overall loading efficiency of the dipole trap.

5.1.2 Compressed MOT

After the MOT phase we implement a short so-called compressed MOT (cMOT) phase, which is also displayed in figure 5.1, to increase the phase space density and reduce the temperature of the cloud. At the begin of the cMOT the detunings of the 3D-MOT beams immediately jump closer to resonance. The cooler is shifted to a red-detuning of -5.5Γ and the repumper to a red-detuning of -5.0Γ . The cMOT lasts for 10 ms and during this time the intensity of the cooler and repumper is reduced in a linear ramp to 2.5 % of their initial intensities. At the end of the cMOT the atomic cloud has a temperature of roughly $650\mu\text{K}$.

At the begin of the cMOT the 2D-MOT beams and the push beam are switched off. Simultaneously the Tilt coil is switched on using the corresponding IGBT. By sending a current of 3.75 A through the Tilt coil we shift the center of the atomic cloud $\sim 2\text{ mm}$ closer to the vacuum chamber. In this way we enhance the overlap of the cMOT and the following gray molasses with the dipole trap. The position of the dipole trap is fixed by the following condition: At the end of the evaporative cooling stage the dipole trap shall be located at the center of the residual curvature of the homogeneous field that we create with the Feshbach coils to enhance the interaction between the atoms during the evaporation. This enables ToF measurements at high magnetic fields without getting additional oscillations of the atomic cloud in the residual curvature of the homogeneous magnetic field. This shift results from the fact that the center of the magnetic field of the MOT coils is not perfectly overlapped with the center of the magnetic field of the Feshbach coils.

5.1.3 Gray molasses

At the end of the cMOT the gray molasses (GM) phase begins which is shown in figure 5.2. In this moment the light of the 3D-MOT is turned off and the light of the GM is turned on simultaneously. In addition the 3D-MOT gradient field and the magnetic field of the Tilt coil are switched off using the corresponding IGBTs. The dipole trap stays at maximum power during the complete gray molasses phase. The GM beams come from the same fibers as the 3D-MOT beams and hence have the same beam waist radii. The cooler has a peak intensity of $23 I_{sat}$ and the repumper has $3 I_{sat}$. Both beams are blue-detuned with $+7.2\Gamma$ to the $D1$ -transition.

As expected we find the minimum temperature of the GM at a two-photon detuning of the Raman transition formed by the cooler and the repumper that is equal to the hyperfine splitting of the ground-state. For this detuning the so-called Λ -enhancement leads to additional dark states in the system resulting in a lower achievable temperature [80]. A measurement of this lambda-enhancement for our system

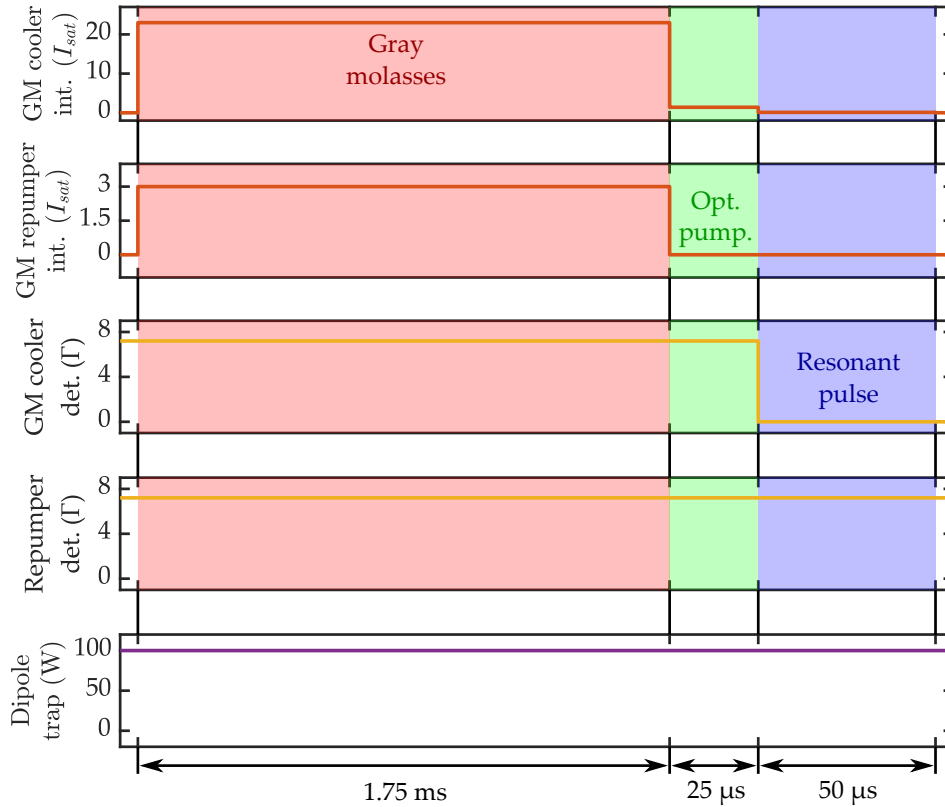


FIGURE 5.2: Timeline of the gray molasses phase. The traces show the intensities and the detunings of the cooler and repumper of the gray molasses light and the power in the dipole trap.

and a characterization of the dependence of the GM performance on the compensation of residual magnetic fields can be found in [18]. We achieve a minimum temperature of $72 \mu\text{K}$ and a phase space density of $5 \cdot 10^{-6}$. At the detuning of the Λ -enhancement we get a capture efficiency of roughly 80% compared to the maximum particle number that we can get with a different detuning.

We apply the GM for 1.75 ms at the described parameters. For the evaporative cooling in the dipole trap we want to start with all atoms in the $F = 1/2$ state. Therefore we rapidly switch off the repumper and set the peak intensity of the cooler to $\sim 1.4 I_{\text{sat}}$ at the end of the GM to optically pump all ${}^6\text{Li}$ atoms into the $F = 1/2$ state which we do for $25 \mu\text{s}$. To remove all residual atoms in the $F = 3/2$ state we then apply a resonant pulse for $50 \mu\text{s}$ by jumping to zero detuning and a peak intensity of $\sim 0.1 I_{\text{sat}}$ of the cooler. After the optical pumping pulse and the resonant pulse the temperature and the phase space density are just slightly worse than directly after the gray molasses and we still have on the order of 10^8 atoms. After the resonant pulse all laser light on the atoms except for the dipole trap is turned off and we end up with roughly 3% of the atoms in the dipole trap for the upcoming evaporative cooling step.

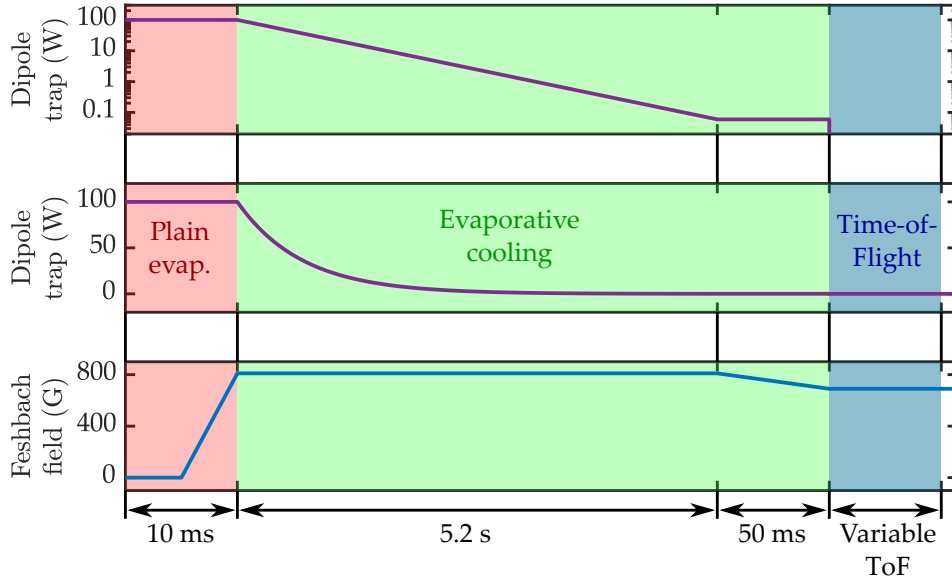


FIGURE 5.3: Timeline of the evaporative cooling phase in the optical dipole trap for the creation of a molecular BEC. The traces show the power in the dipole trap and the homogeneous magnetic field of the Feshbach coils. The dipole trap is displayed twice, once with a linear y-axis and once with a logarithmic y-axis. The logarithmic scale uncovers the behavior of the dipole trap at the end of the evaporation.

5.2 Evaporative cooling

The evaporative cooling begins with a so-called plain evaporation where we keep the dipole trap power at its maximum value for 10 ms (see figure 5.3 and 5.6) so that the hottest atoms can already escape from the trap before we begin with the forced evaporation. During the last 5 ms of the plain evaporation we linearly ramp the homogeneous magnetic field of the Feshbach coils in Helmholtz configuration from 0 to 810 G. This sets the scattering length a between the Paschen-Back states $|1\rangle$ and $|2\rangle$ of ${}^6\text{Li}$ to a value $a > 6000 a_0$, with a_0 being the background scattering length. This enables fast and effective evaporative cooling of the atoms. The plain evaporation is the same in the experimental cycles to create both a molecular BEC and a degenerate Fermi gas. The forced evaporation has to be executed differently between the two cases which we describe in detail in the following sections.

5.2.1 Molecular BEC

For the forced evaporation we lower the power P_{ODT} of the dipole trap in an exponential ramp according to the equation

$$P_{ODT} = 100 \text{ W} \cdot e^{-t/\tau} \quad , \quad (5.1)$$

with 100 W being the maximum power of our dipole trap laser, t being the duration of the forced evaporation and the time constant τ defining the steepness of the evaporation ramp. Minimizing the experimental cycle time without losing efficiency of

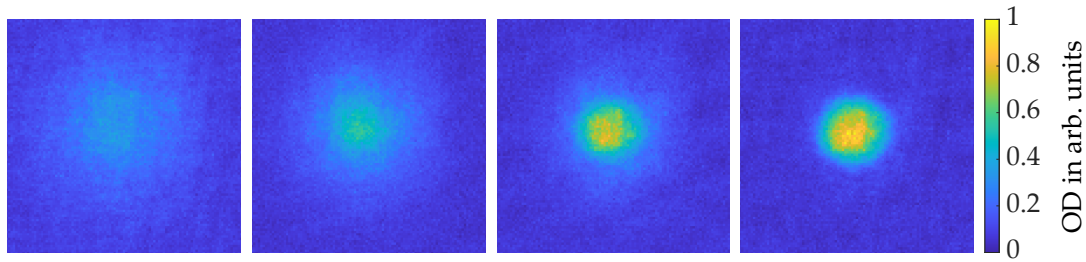


FIGURE 5.4: Onset of Bose-Einstein condensation of the molecular ${}^6\text{Li}$ dimers. From left to right the atoms are always cooled a bit further in the optical dipole trap. All images are taken after a ToF of 4 ms.

the forced evaporation leads to a optimized τ of 0.7 s for our experiment. Such fast evaporative cooling is only possible because the very large scattering length of the lithium atoms, which we get in the vicinity of the Feshbach resonance, leads to a short thermalization time.

The positive sign of the scattering length at 810 G leads to the formation of molecules, consisting of one atom in state $|1\rangle$ and another atom in state $|2\rangle$ [13]. The formation of molecules begins when the temperature of the atomic cloud becomes lower than a critical temperature during the evaporation. The arising molecules are bosons because the combination of two fermions with half-integer spin automatically results in a boson with integer spin. These bosonic molecules can then undergo the phase transition to a Bose-Einstein condensate (BEC) which happens at even lower temperatures than the formation of the molecules.

Figure 5.4 shows the onset of Bose-Einstein condensation in a cloud of bosonic ${}^6\text{Li}$ dimers at the end of the evaporation. The images are taken for a constant ToF of 4 ms. In the first picture on the left side the cloud is still completely thermal but with further evaporation the molecules begin to macroscopically occupy the ground state of the trap. In the last picture on the right side the molecular BEC seems to be quasi-pure. Nevertheless, we have to evaporate a bit further to get the largest condensate fraction. For the creation of the purest possible BEC we stop the evaporation when further reduction of the dipole trap power only leads to a loss of atoms without reducing the temperature anymore. This happens after 5.2 s in our experiment when there is only ~ 60 mW laser power left in the dipole trap. A systematic analysis in [18, 96] showed that the condensate fraction that we can achieve is limited to 55(9) % which results from the strong interaction between the molecules [13, 124].

At the end of the evaporative cooling stage we linearly ramp the homogeneous magnetic field of the Feshbach coils to 690 G within 50 ms. This reduces the scattering rate of the atoms and enables direct imaging of the molecules [125]. After the magnetic ramp the molecular BEC can either be imaged in situ in the dipole trap or ToF measurements can be performed by switching off the trap and letting the cloud expand for various times. For the imaging of the cloud after the expansion the magnetic field has to stay at 690 G during the expansion. If the dipole trap is not overlapped with the center of the residual curvature of the homogeneous magnetic field,

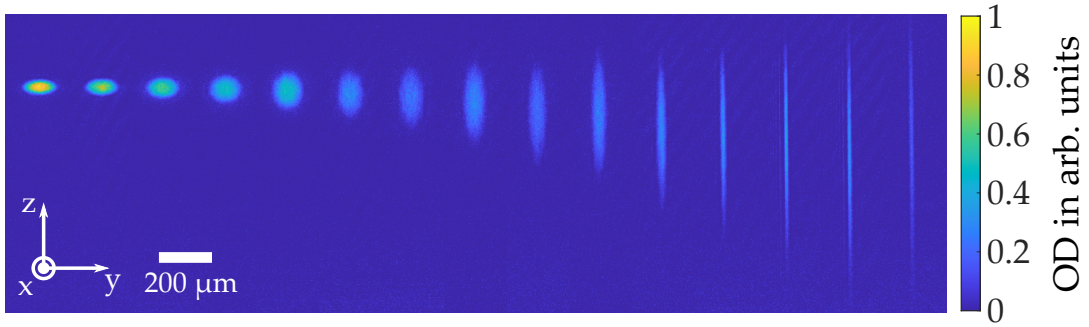


FIGURE 5.5: Time-of-Flight series of a molecular BEC from 0 to 14 ms expansion time in steps of 1 ms. The high-field seeking atoms are confined along the horizontal x - and y -direction and anti-confined along the vertical z -direction by the residual curvature of the homogeneous magnetic field of the Feshbach coils. This leads to a strong elongation of the cloud along the z -direction during the end of the displayed expansion.

we see additional oscillations of the cloud during the expansion.

The high laser power of the optical dipole trap leads to significant thermal lensing on the walls of the glass cell which results in a movement of the focus position of the two dipole trap beams. Hence the trapped atoms also move because they follow the position of the foci. It is therefore not possible to realize a crossed dipole trap, where the atoms are trapped in the intersection area of the two beams, during the complete evaporative cooling step. We adjust the dipole trap beams such that they are overlapped with each other and with the center of the residual magnetic curvature at the end of the evaporation. Typical intended variations of the evaporation time usually do not affect the position of the dipole trap because at a laser power of 10 W per beam we already do not see thermal lensing anymore. Anyhow the second pass beam of the crossed dipole trap seems to be a significantly deeper trap than the first pass beam at the end of the evaporation. Hence we observe that we end up with an effective single-beam dipole trap because all atoms accumulate in this beam. Further discussion of the thermal lensing dynamics during the evaporation and a measurement of the trap frequencies of the single-beam dipole trap at the end of the evaporation can be found in [18].

If the dipole trap is overlapped with the center of the residual curvature of the homogeneous magnetic field we expect no oscillations of the atomic cloud along this curvature during an expansion. Nevertheless, the curvature of the magnetic field also affects the expansion of the cloud in this case. A ToF series of a molecular BEC with the maximum condensate fraction, which we can achieve, is shown in figure 5.5. From left to right the expansion time is varied between 0 and 14 ms in steps of 1 ms before the absorption image is taken. At zero ToF the cloud is elongated due to the asymmetry of the dipole trap. The behavior of the cloud during the first milliseconds of expansion could be interpreted as the typical inversion of the aspect ratio of the BEC which is a striking feature of a condensed cloud compared to a thermal sample. However, the further expansion of the cloud reveals that its behavior

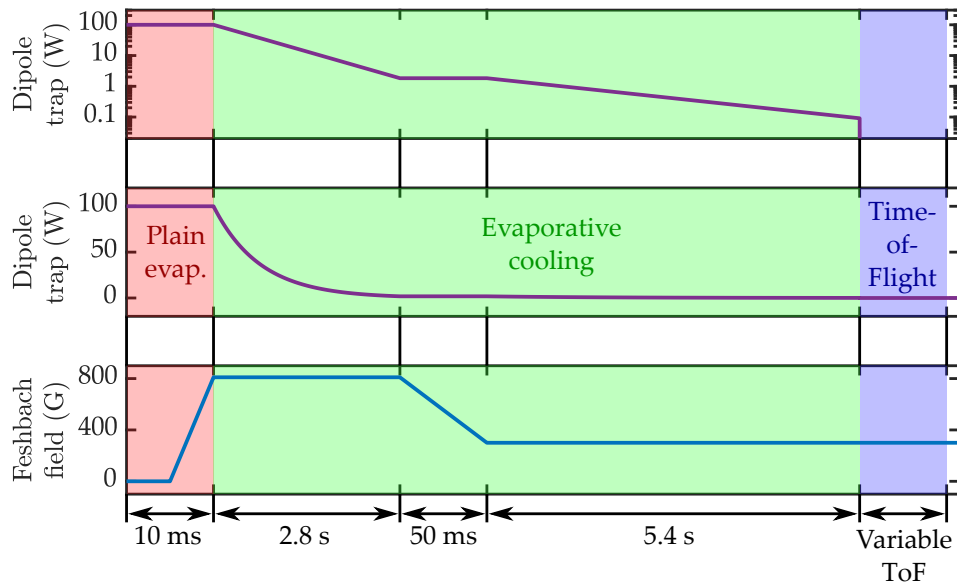


FIGURE 5.6: Timeline of the evaporative cooling phase in the optical dipole trap for the creation of a degenerate Fermi gas. The traces show the power in the dipole trap and the homogeneous magnetic field of the Feshbach coils. The dipole trap power is displayed a second time with a logarithmic y-axis to show the behavior of the dipole trap at the end of the evaporation.

seems to be dominated by the residual curvature of the magnetic field. The high-field seeking atoms are trapped in the radial plane and anti-trapped in the vertical z -direction by the residual curvature which leads to very strong elongation of the atomic cloud along the z -direction at the end of the expansion.

5.2.2 Degenerate Fermi gas

For the creation of a degenerate Fermi gas we have to avoid the formation of bosonic molecules during the evaporation that was described in the last section. Therefore, a typical evaporation procedure to create a degenerate Fermi gas works in the following way: After the plain evaporation we first perform again forced evaporation at 810 G to benefit from the high scattering length at this magnetic field. After an exponential ramp of 2.8 s with a time constant of 0.7 s we stop the evaporation at a dipole trap power of ~ 1.8 W before molecules begin to form (see figure 5.6). We then ramp the magnetic field linearly to 300 G within 50 ms. At this magnetic field the scattering length between the Paschen-Back states $|1\rangle$ and $|2\rangle$ is negative and hence no molecules form. During the magnetic ramp the power in the dipole trap stays constant.

At 300 G a second exponential evaporation ramp is performed. This ramp typically lasts for 5.4 s with a slower exponential time constant of 1.8 s. At the end of the second ramp the remaining laser power in the dipole trap is ~ 90 mW. The Fermi gas can be imaged at 300 G. So there is no need for an additional ramp of the magnetic bias field at the end of the evaporation. Instead the dipole trap can be turned off

directly to realize an expansion and subsequent imaging.

The determination of the degeneracy T/T_F of a Fermi gas becomes difficult for highly degenerate samples because the temperature only affects the wings of the cloud beyond the Fermi radius [13]. Hence, thermometry of very cold Fermi gases is often limited by the signal-to-noise ratio in the low-density wings. When we created a Fermi gas for the first time in our experiment we optimized as usual the experimental sequence to get the slowest possible expansion of the cloud at the end of the evaporation combined with a reasonably high particle number. We measured several ToF series for different evaporation schemes to extract the respective particle number and degeneracy of the samples. The absorption images were taken with the imaging setup where the imaging beam is sent through the aspheric lens of the accordion lattice. During the analysis of the data we realized that the signal-to-noise ratio in this auxiliary imaging setup is not sufficient to extract the degeneracy of the Fermi gas from its wings.

During the writing of this thesis the experimental sequence for the creation of degenerate Fermi gases has been improved further. An RF antenna is implemented to transfer all atoms in the Paschen-Back state $|2\rangle$ to state $|3\rangle$ via a Landau-Zeener sweep. The sweep is implemented after the first evaporation ramp. In consequence the second evaporation ramp that takes place at 300 G is performed with a mixture of the states $|1\rangle$ and $|3\rangle$ instead of the states $|1\rangle$ and $|2\rangle$. For the $|1\rangle - |3\rangle$ mixture the scattering length at 300 G is $a_{13} \simeq -880 a_0$ which is almost three times larger than the scattering length of the $|1\rangle - |2\rangle$ mixture which is $a_{12} \simeq -290 a_0$ at 300 G (see appendix C). The higher scattering rate enables a more efficient evaporation which leads to a higher degeneracy of the Fermi gas [68, 83]. We already observed a significantly colder Fermi gas in our experiment by making use of this feature. The details of this realization of an ultracold $|1\rangle - |3\rangle$ Fermi gas will be described in the upcoming Master's thesis of Tobias Petersen.

Chapter 6

Optical lattices

After the creation of ultracold atomic samples we now turn to the implementation of the deep optical lattices as the next step towards the realization of quantum gas microscopy. For this purpose this chapter is divided into two sections. The first one deals with the accordion lattice for the vertical direction and the second one with the triangular lattice for the horizontal plane. For both lattices we first discuss the respective adjustment procedure and then we show first measurements with the lattices that we use to analyze their actual properties and compare them to our theoretical expectations.

The adjustment procedures for the optical lattices have been developed and implemented by a team consisting of Andreas Kerkmann, Mathis Fischer and the author under the supervision of Klaus Sengstock and Christof Weitenberg. The displayed data were taken by the same team. The analysis of the accordion lattice spacings has been done by Andreas Kerkmann and the presented analysis of the Kapitza-Dirac peaks has been carried out by the author.

6.1 Accordion lattice

We start with the implementation and characterization of the optical accordion lattice which shall enable the preparation of two-dimensional atomic samples and in addition serve as the pinning lattice along the vertical direction for site-resolved imaging. We begin with the description of the adjustment process to enable loading and compression of the optical accordion without inducing a movement of the interference pattern. Next we discuss how we measure the range of possible lattice spacings and then attend to the compression of the accordion.

6.1.1 Adjustment of the lattice beams

The coarse adjustment of the accordion lattice is relatively straightforward because at maximum power both lattice beams contain 20 W of laser power. In combination with a beam waist radius of $w_0 = 47.8(5) \mu\text{m}$ [96] they create two attractive single-beam dipole traps that are strong enough to load atoms directly from the gray molasses. Due to the relatively large size of the gray molasses, especially after some

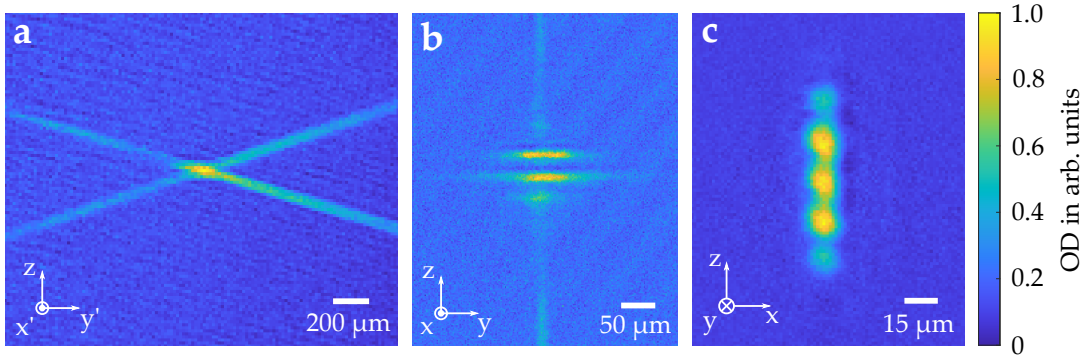


FIGURE 6.1: Absorption images of the accordion lattice with various intersection angles and hence lattice spacings taken with three different imaging setups. The color scales of the images are independent of each other. (a) Atoms are directly loaded from the gray molasses into the lattice beams. (b) A molecular BEC is partially loaded into lattice planes during expansion from the dipole trap. (c) The atoms are directly cooled evaporatively into the lattice planes. The intersection angle in (a), the lattice spacings in (b) and (c) and the resulting lattice spacings for all three images are mentioned in the main text.

ToF, a starting point for further adjustment is easily found. Optimization of the signal leads to images like in figure 6.1 (a).

To enable adiabatic loading of an ultracold cloud into the accordion lattice the intersection point of the two lattice beams has to be overlapped with the position of the atoms at the end of the evaporative cooling phase. This can be done with careful adjustment of the mirrors behind the PBS and with the small XYZ translation stage of the aspheric lens (see section 3.4). For a static position of the lattice beams this procedure can be routinely executed. A much bigger issue is to avoid movement of the intersection point when the accordion is compressed. During the compression the beams migrate along the aspheric lens and there is only point that they always pass behind the lens. This so-called pivot point is fixed to the focal plane of the aspheric lens but the pivot points of the two lattice beams are only overlapped if both beams hit the lens without any incident angle. The position of the pivot points in the focal plane can be adjusted very carefully with the mirrors in front of and behind the PBS but this is a very delicate procedure. More details on the adjustment of the accordion lattice can be found in [18, 96].

6.1.2 Analysis of the lattice spacings

Once the accordion lattice is aligned we can make use of the different absorption imaging setups in our experiment to analyze the actual lattice spacing for different positions of the linear translation stage. The corresponding absorption images are shown in figure 6.1. For figure 6.1 (a) the imaging beam propagates along the direction of one of the horizontal 3D-MOT beams. Here the atoms are loaded directly into the lattice beams from the gray molasses as it was already described in the last section. The intersection angle of the lattice beams can be measured and then the lattice spacing can be calculated via $a_{acc} = \lambda_L / (2 \sin(\theta/2))$. However the horizontal axis

of these images needs to be stretched by a factor of $1/\cos(45^\circ)$ to get the real intersection angle due to the 45° angle between the imaging beam and the lattice beams. These images are especially suited to measure large angles between the beams and hence small lattice spacings. The corrected intersection angle for the displayed image is $25.7(12)^\circ$ which results in a lattice spacing of $a_{acc} = 2.4(1) \mu\text{m}$.

The absorption image in figure 6.1 (b) is taken with the imaging beam that propagates along the axis of the push beam which corresponds to the x-axis in the coordinate system that we defined for our experimental setup. In this case the accordion lattice is turned on the whole time at a small depth during the creation of a molecular BEC as it was described in section 5.2.1. The shallow lattice does not affect the creation of the BEC but after the dipole trap is turned off many of the ultracold atoms are loaded into different planes of the accordion during their expansion. The shown absorption image is taken 15 ms after the dipole trap is switched off. From such an image the corresponding lattice spacing of the accordion can be extracted directly. The only information that is additionally needed is the magnification of the used imaging setup. In the shown image the lattice spacing is $a_{acc} = 31.3(15) \mu\text{m}$. For the determination of the range of possible lattice spacings we actually use images where the molecular BEC is loaded adiabatically into the accordion from the dipole trap instead of the type of image that is shown here. However, both approaches produce images that can be used in the same way to extract the lattice spacings.

The image in figure 6.1 (c) is taken with an imaging beam that propagates on the same axis as the accordion lattice beams. This corresponds to the y-axis in the coordinate system of our apparatus. In consequence the atomic signal is integrated along the weakest confinement of the pancake-shaped lattice sites in this imaging setup. In the experimental sequence for the creation of this image the dipole trap and the accordion lattice are both ramped up to full power at the end of the 3D-MOT phase. After the gray molasses the atoms are evaporatively cooled by simultaneously lowering the power in the dipole trap and the accordion lattice. The evaporation ramp for the accordion lattice beams is realized in the same way as for the dipole trap beams by using the motorized rotation mount (see section 3.4). In this way the atoms are cooled directly into several planes of the accordion lattice. Here the lattice spacing, which is $a_{acc} = 17.8(15) \mu\text{m}$ in the displayed image, can again be extracted directly from the absorption image if the magnification of the imaging setup is known.

By combining the results from the different imaging setups we can map out the range of lattice spacings that we can realize with our accordion lattice. The results are shown in figure 6.2. The data are adapted from [18] where more technical details of the analysis are also discussed. We can calculate the expected lattice spacings via

$$a_{acc} = \frac{\lambda_L}{2} \sqrt{1 + 4 \left(\frac{f}{D} \right)^2} . \quad (6.1)$$

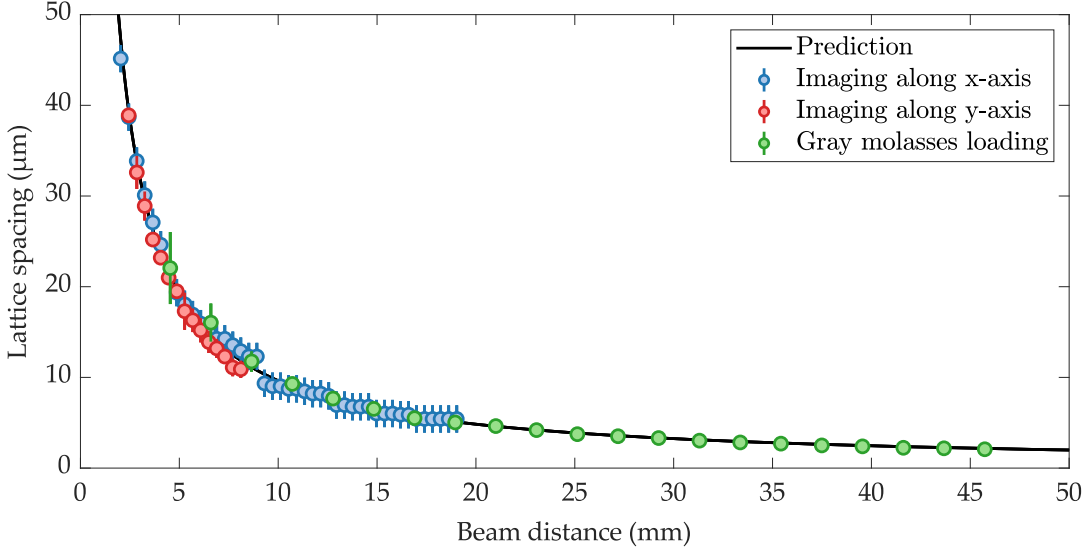


FIGURE 6.2: Realizable lattice spacings of the optical accordion which have been measured with three experimental cycles and corresponding imaging setups. The different methods and the calculation of the prediction curve are explained in the main text. The errorbars are calculated with gaussian error propagation from the uncertainty of the measured lattice spacing (imaging along x-axis and y-axis) or the measured intersection angle (gray molasses loading). Data taken from [18].

We know the wavelength $\lambda_L = 1069.8 \text{ nm}$ of the accordion lattice laser and the effective focal length $f = 87.6 \text{ mm}$ of the aspheric lens. We have to calibrate the distance D between the lattice beams in front of the aspheric lens as a function of the position of the translation stage (see section 3.9) to compare our results with the expected curve which is displayed as the solid black line in figure 6.2. The measured values nicely match this curve within their errorbars. From the measured values we can extract that we can tune the full intersection angle θ between the lattice beams in the range of $1.36(3)^\circ$ to $29.9(5)^\circ$. This corresponds to lattice spacings between $45(1) \text{ }\mu\text{m}$ and $2.07(3) \text{ }\mu\text{m}$. For the maximally compressed accordion lattice in combination with the already mentioned beam waist radius of $w_0 = 47.8(5) \text{ }\mu\text{m}$ we expect the axial trap frequency to be $\omega_z/2\pi = 460 \text{ kHz}$ for the maximum laser power of 20 W per beam.

6.1.3 Compression of the accordion

The compression of the accordion lattice is realized by moving the linear translation stage. An adiabatic compression of the atoms conserves the phase space density of the sample but the temperature unavoidably increases. As described in section 6.1.1 the intersection point of the two accordion beams moves during the compression if the pivot points of both beams are not at the same position. Such an additional movement of the lattice during the compression induces even more heating of the cloud. Moreover, it is generally favorable to have the compressed cloud at the same position as the molecular BEC. The integration of loading and compressing the accordion lattice into a typical experimental cycle is discussed in section 6.3.

There is the additional risk that atoms are loaded into adjacent lattice planes during the compression of the accordion. We can not check directly if after the compression still only one plane is filled with atoms because the resolution of all imaging setups described in the last section is not high enough to resolve the minimum lattice spacing of $2.07(3) \mu\text{m}$. After compression we can decompress the cloud again and see if there are any atoms in other lattice planes which is not the case. In the end atoms in adjacent lattice sites will unavoidably influence the signal, when single-site resolved imaging is performed, and become visible in this way [55, 56].

6.1.4 Next steps

Besides the measurement of the realized lattice angles a characterization of the created lattice depths for different angles and laser powers would be useful. This is not directly possible in our setup because there is no AOM for dynamical switching of the lattice beams to implement for example Kapitza-Dirac scattering (see section 6.2.4 for a short discussion of possible methods to calibrate our optical lattices). Even though the implementation of an AOM in the accordion lattice setup is worth to consider it is unavoidably accompanied by thermal lensing effects which would make the delicate adjustment of the accordion lattice even more difficult.

Adjusting the accordion lattice can be satisfyingly performed with our current setup with the pivot points being the unpleasant exception. Overlapping the pivot points with the position of the molecular BEC is possible in general but up to now it remains very difficult to find a repeatable procedure which enables us to do this in a reasonable amount of time. As a consequence we are even more dependent on the passive stability of the setup because readjusting it is so involved. Maybe we will have to consider to upgrade the optomechanical setup for the adjustment of the accordion lattice in the future. In addition we observe that the interference pattern of the accordion lattice is moving over a period of hours. Thus, we probably need to actively stabilize the interference pattern. This could for example be done with a piezo that is glued on one of the two mirrors that adjusts the final position of the corresponding lattice beam.

6.2 Triangular lattice

This section is dedicated to the implementation and a first characterization of the triangular lattice in the horizontal plane. We first describe the adjustment procedure for the three lattice beams. Then we show the realization of Kapitza-Dirac scattering and finally we use the positions of the created Bragg peaks to analyze the actual lattice angles that we have realized.

6.2.1 Adjustment of the lattice beams

For a coarse adjustment of the three lattice telescopes lines are marked on the breadboard as a guidance for their correct position. Along these lines the telescopes are placed such that the focusing lens, which has a focal length of $f = 150$ mm, roughly has this distance from the position of the atoms. As described in section 3.5 there are no additional mirrors behind the telescopes and the only tool to adjust the position of the focused lattice beams is fine-tuning of the lens position. In consequence the positioning of the lattice telescopes on the breadboard has to be precise enough to be able to adjust the foci of the lattice beams to the position of the atoms.

For the lattice beams with the numbers 2 and 3 (see section 3.5) which are not dumped in the vacuum chamber the coarse adjustment can be improved by using a charge-coupled device (CCD) camera. These two lattice beams are recollimated after they have passed the glass cell to avoid strong divergence of this high power beams and to guide them into water-cooled beam dumps. The recollimation lenses can also collect fluorescence light of the 3D-MOT. Therefore, we turn on the MOT and one lattice beam at very low power at the same time and send them onto the CCD camera. By overlapping the lattice beam and the 3D-MOT fluorescence signal on the camera we are able to adjust the lattice beam closer to the atoms. Only a small part of the 3D-MOT fluorescence, which is naturally distributed over the complete solid angle, is collected by the recollimation lens. Hence, its signal on the CCD camera is very weak and all filters have to be removed from the camera to make it visible. This procedure has to be done very carefully because too much laser power in the lattice beam can easily destroy the CCD camera when no filter is installed that protects the camera chip.

This procedure is not employable for lattice beam 1 that propagates nearly parallel to the axis of the push beam. The telescope of this beam is slightly tilted such that the beam is dumped in the vacuum chamber and not in the graphite tube. This fact and the additional demand, that this lattice beam must not hit the graphite tube, hinder the coarse adjustment of this lattice beam.

For further adjustment of the lattice beams we already need to be able to observe their influence on the atomic cloud. We start with a molecular BEC of ${}^6\text{Li}$ dimers (see section 5.2.1) and then switch on one lattice beam at full power for a short time using the corresponding slow shear AOM. If the focus position of the corresponding lattice beam is already close enough to the position of the molecular BEC, we can see that the atoms have disappeared after the lattice beam has been switched on. The atoms disappear because the dipole force of the high power lattice beam pulls them out of the dipole trap which is very shallow at the end of the evaporation. If we see that the atoms disappear, the position of the lattice beam can be tuned such that we reduce the switch on time and the power of the beam that is needed to still let the atoms disappear. In this way we bring the focus of the lattice beam closer to the atoms.

At some point we can observe that the lattice beam does not only pull the atoms out

of the dipole trap but that the atoms begin to accumulate in the single-beam dipole trap that is formed by the lattice beam. This elongated trap can then be overlapped with the center of the BEC which enables adiabatic loading of the atoms into the triangular lattice by ramping up all three lattice beams slow enough at the same time. For this final adjustment step the atoms are held in the lattice beam for enough time such that no oscillations remain from the transfer of the atoms from the dipole trap to the lattice beam which could falsify the actual position of the lattice beam. Alternatively the power in the lattice beam can be ramped up and held at the final value for some time to further reduce the dynamics that is induced in the atomic cloud during the transfer from the dipole trap.

This adjustment procedure has to be done for all three lattice beams individually. For the two beams, whose position has been overlapped with the fluorescence signal of the 3D-MOT, an influence of the laser beam on the molecular BEC is often visible directly and a starting point for the further adjustment is given in this way. That is usually not the case for the lattice beam that is dumped inside the vacuum chamber. For this beam we just can try to scan the position of the lattice beam by moving its telescope and by tuning the position of the focusing lens. While doing this we have to take care that we do not hit the graphite tube with the beam. With this trial and error method we sooner or later observe the desired effect of the lattice beam on the molecular BEC.

The described way of adjusting the three beams of the triangular lattice works relatively well for the radial position of the focus of each beam and a more precise adjustment requires a precise determination of the realized lattice depth. The adjustment is not as sensitive for the longitudinal position of the focus because the trap frequency of each individual beam is much smaller along its propagation axis compared to the radial trap frequency. Thus, the atoms are widely elongated along the lattice beam and the position of the focus can not be determined appropriately. This is not a big problem for the first realization of the triangular lattice because the change of the intensity of the lattice beam along its propagation axis is rather small due to its Rayleigh range of $z_R = \pi w_0^2 / \lambda = 4.7$ mm. For a precise adjustment of the longitudinal focus position of each lattice beam we again have to be able to precisely measure the actual lattice depth.

6.2.2 Kapitza-Dirac scattering

After the coarse adjustment of the three lattice beams described in the last section we can now try to make the triangular lattice structure visible. We do this by performing Kapitza-Dirac scattering as it is for example described in [126, 127]. For this purpose we let the molecular BEC expand from the dipole trap for a ToF of 2 ms. At the begin of the expansion we switch on the three lattice beams for 5 μ s using the AOMs. This timestep needs to be shorter than the inverse recoil energy of the triangular lattice $1/E_r = 1/29.0$ kHz = 34.5 μ s.

The resulting image is shown in figure 6.3 (a). Due to the limited signal-to-noise

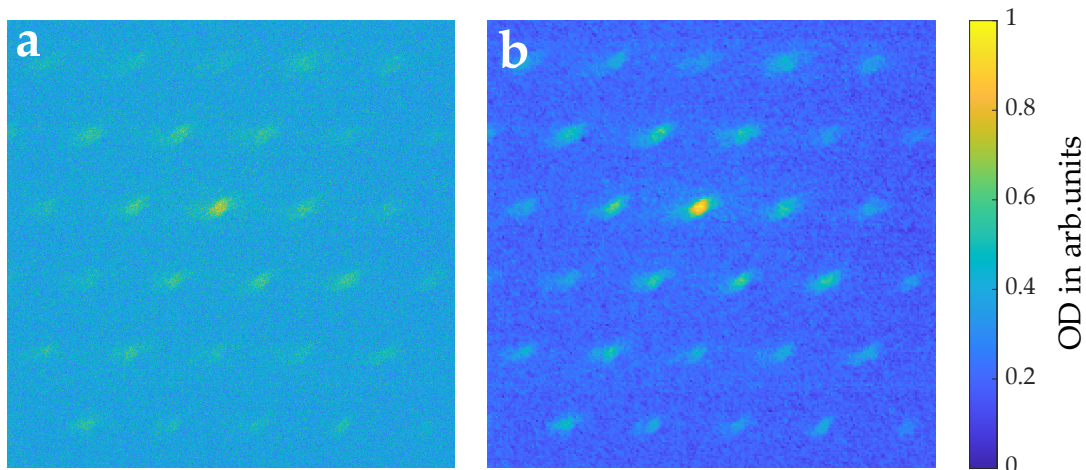


FIGURE 6.3: Kapitza-Dirac scattering of the atoms by the transient triangular optical lattice. (a) Raw data average of 40 iterations. (b) 4×4 pixel binning and a 2D Wiener filter are applied to increase the signal-to-noise ratio such that the hexagonal structure of the Bragg peaks becomes more visible. The color scales of the two images are independent of each other.

ratio we have to average 40 images to get the displayed signal. In general the signal quality seems to be restricted for a molecular BEC due to its limited condensate fraction. We can increase the visibility of the hexagonal lattice structure by applying 4×4 pixel-binning and a 2D Wiener filter which is shown in figure 6.3 (b). The distribution of the atoms to the different lattice peaks is very isotropic which means that the created lattice depth has to be quite similar for all three axes of the lattice. In addition the occupation of so many peaks is a hint that the lattice is relatively deep. The elliptical shape of the Kapitza-Dirac peaks seems to be an artifact of the original form of the molecular BEC in the dipole trap at the begin of the expansion when it is shaped elliptically along the horizontal direction.

6.2.3 Analysis of the lattice structure

We now want to use the described measurement of Kapitza-Dirac scattering to analyze the actual lattice angles that we have created with the adjustment of our setup which was described in section 6.2.1. Our analysis is based on a similar analysis that is described in [128]. The measured Kapitza-Dirac peaks display the momentum space distribution of the molecular BEC in the triangular lattice. Hence the distances between the central peak and its 6 nearest neighbors are equal to the primitive reciprocal lattice vectors. In general two reciprocal lattice vectors are sufficient to completely describe the created triangular lattice by calculating the wave vectors, the primitive lattice vectors and the lattice angles. We discuss most of the obtained results here but for completeness all derived values are listed in appendix D.

We define the position of the central peak to be at $\mathbf{p}_0 = (0,0)$ such that the coordinates of the reciprocal lattice vectors are defined in respect of the central peak position. To determine the positions of the 6 nearest neighbor peaks we first sum

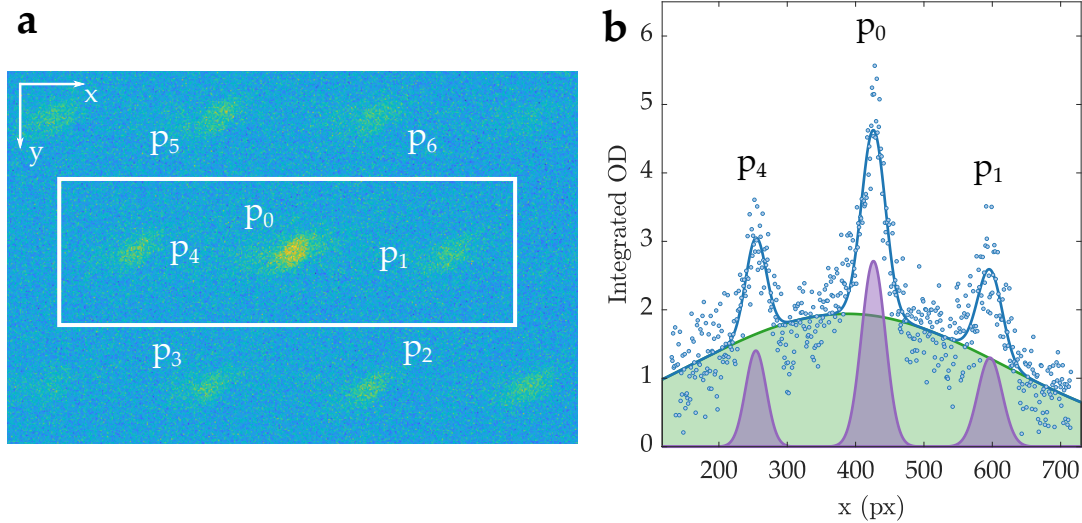


FIGURE 6.4: Analysis of the positions of the Kapitza-Dirac peaks for the determination of the lattice structure. (a) We show the central peak and the numbered 6 nearest neighbors peaks that are used for the evaluation. The OD inside the white rectangle is integrated along the y-direction for the fit in (b). (b) We fit a gaussian for every peak and an additional gaussian for the background signal to determine the position of the peaks along the x-direction in this example.

the OD along the rows and the columns. Then a gaussian is fitted for every peak to determine their position. An additional gaussian is fitted to subtract the background signal. For the analysis described in this section we use the unfiltered data that is shown in figure 6.4 (a). Even though the signal-to-noise ratio is rather low it is sufficient to precisely determine the positions of the peaks with the gaussian fits as it is exemplarily shown in figure 6.4 (b).

The three pairs of primitive reciprocal lattice vectors are expected to be of the same length but of opposite sign such that $\mathbf{p}_1 = -\mathbf{p}_4$, $\mathbf{p}_2 = -\mathbf{p}_5$ and $\mathbf{p}_3 = -\mathbf{p}_6$. We therefore define the three reciprocal lattice vectors for the subsequent analysis as the component-by-component average of each pair of vectors:

$$\begin{aligned}
 b_{1,x} &= \frac{(p_{1,x} - p_{4,x})}{2} , & b_{1,y} &= \frac{(p_{1,y} - p_{4,y})}{2} , \\
 b_{2,x} &= \frac{(p_{2,x} - p_{5,x})}{2} , & b_{2,y} &= \frac{(p_{2,y} - p_{5,y})}{2} , \\
 b_{3,x} &= \frac{(p_{3,x} - p_{6,x})}{2} , & b_{3,y} &= \frac{(p_{3,y} - p_{6,y})}{2} .
 \end{aligned} \tag{6.2}$$

As the lattice is completely defined by two primitive reciprocal lattice vectors already, we can choose for example \mathbf{b}_1 and \mathbf{b}_2 to set up a system of equations for the

determination of the three wave vectors:

$$\begin{aligned}
 k_{1,x} - k_{3,x} &= b_{2,x} \\
 k_{1,y} - k_{3,y} &= b_{2,y} \\
 k_{2,x} - k_{3,x} &= b_{1,x} \\
 k_{2,y} - k_{3,y} &= b_{1,y} \\
 \sqrt{k_{1,x}^2 + k_{1,y}^2} &= \sqrt{k_{3,x}^2 + k_{3,y}^2} \\
 \sqrt{k_{2,x}^2 + k_{2,y}^2} &= \sqrt{k_{3,x}^2 + k_{3,y}^2} .
 \end{aligned} \tag{6.3}$$

Here we have used the definition of the reciprocal lattice vectors and the fact that all wave vectors must have the same length (see section 2.2.5). This system of equations has 6 equations and 6 unknown variables and hence a unique solution which are the three wave vectors. We also solve the corresponding system of equations for the pairs $\mathbf{b}_1 / \mathbf{b}_3$ and $\mathbf{b}_2 / \mathbf{b}_3$. In this way we get three values for all components of the wave vectors. We average over these three values and take the standard deviation of this mean as the uncertainty of the results. By calculating the norm of any of the resulting wave vectors we can get the wave number $k_L = 2\pi/\lambda_L = 98.3808 \frac{1}{\text{px}}$ and the wavelength of the laser $\lambda_L = 0.0639 \text{ px}$ in units of camera pixels. With the wave number we can display the calculated wave vectors in the known form (see section 2.2.5):

$$\begin{aligned}
 \mathbf{k}_1 &= k_L \begin{pmatrix} -0.031 \\ 1.000 \end{pmatrix} \pm k_L \begin{pmatrix} 0.004 \\ 0.001 \end{pmatrix} , \\
 \mathbf{k}_2 &= \frac{k_L}{2} \begin{pmatrix} 1.753 \\ -0.963 \end{pmatrix} \pm \frac{k_L}{2} \begin{pmatrix} 0.004 \\ 0.002 \end{pmatrix} , \\
 \mathbf{k}_3 &= \frac{k_L}{2} \begin{pmatrix} -1.733 \\ -0.998 \end{pmatrix} \pm \frac{k_L}{2} \begin{pmatrix} 0.005 \\ 0.005 \end{pmatrix} .
 \end{aligned} \tag{6.4}$$

We see that they are very close to the values that are expected for a perfect triangular lattice. The indices of the reciprocal lattice vectors were chosen such that the indices of the resulting wave vectors correspond to the numbers that we gave the three lattice beams in section 3.5. In the same way as for the wave vectors we can now

also display the primitive reciprocal lattice vectors in the familiar form:

$$\begin{aligned} \mathbf{b}_1 &= \sqrt{3} k_L \begin{pmatrix} 1.005 \\ 0.011 \end{pmatrix} \pm \sqrt{3} k_L \begin{pmatrix} 0.011 \\ 0.017 \end{pmatrix} , \\ \mathbf{b}_2 &= \frac{\sqrt{3} k_L}{2} \begin{pmatrix} 0.967 \\ 1.729 \end{pmatrix} \pm \frac{\sqrt{3} k_L}{2} \begin{pmatrix} 0.048 \\ 0.001 \end{pmatrix} , \\ \mathbf{b}_3 &= \frac{\sqrt{3} k_L}{2} \begin{pmatrix} -1.051 \\ 1.711 \end{pmatrix} \pm \frac{\sqrt{3} k_L}{2} \begin{pmatrix} 0.075 \\ 0.025 \end{pmatrix} . \end{aligned} \quad (6.5)$$

The three lattice angles can be directly calculated using the inner product of the three wave vectors:

$$\alpha = \arccos \left(\frac{\mathbf{k}_2 \cdot \mathbf{k}_3}{|\mathbf{k}_2| |\mathbf{k}_3|} \right) , \quad \beta = \arccos \left(\frac{\mathbf{k}_1 \cdot \mathbf{k}_3}{|\mathbf{k}_1| |\mathbf{k}_3|} \right) , \quad \gamma = \arccos \left(\frac{\mathbf{k}_1 \cdot \mathbf{k}_2}{|\mathbf{k}_1| |\mathbf{k}_2|} \right) . \quad (6.6)$$

The resulting angles are:

$$\alpha = 121.3^\circ \pm 0.3^\circ , \quad \beta = 118.1^\circ \pm 0.3^\circ , \quad \gamma = 120.6^\circ \pm 0.3^\circ . \quad (6.7)$$

As already expected from the wave vectors and the reciprocal lattice vectors the actual lattice angles are reasonably close to the aspired 120° considering the fact that this is the first analysis of the lattice angles and that up to now we had no tool for a very precise adjustment of the angles. It should be possible to automatize and speed up the analysis described here to minimize its time and effort. Then it could be possible to use this method for a fine-tuning of the lattice angles. In general the lattice angles are not highly critical for using the triangular lattice as the pinning lattice for site-resolved imaging.

The primitive lattice vectors \mathbf{a}_i are related to the primitive reciprocal lattice vectors \mathbf{b}_j via the relation $\mathbf{a}_i \cdot \mathbf{b}_j = 2\pi\delta_{ij}$. Choosing two of the primitive lattice vectors and two of the primitive reciprocal lattice vectors this relation defines the following system of equations:

$$\begin{aligned} a_{1,x} b_{1,x} + a_{1,y} b_{1,y} &= 2\pi \\ a_{2,x} b_{2,x} + a_{2,y} b_{2,y} &= 2\pi \\ a_{1,x} b_{2,x} + a_{1,y} b_{2,y} &= 0 \\ a_{2,x} b_{1,x} + a_{2,y} b_{1,y} &= 0 , \end{aligned} \quad (6.8)$$

which can be solved to get \mathbf{a}_1 and \mathbf{a}_2 . This system of equations is again solved for all three combinations of reciprocal lattice vectors. The third primitive lattice vector can then be calculated as the sum of the two primitive lattice vectors of each solution. We again average the three values for each component of the primitive lattice vectors and take the standard deviation of this mean as the uncertainty of the results. We use $\lambda_L = 0.0639$ px to display the results of the primitive lattice vectors in the known

form:

$$\begin{aligned}
 \mathbf{a}_1 &= \frac{\lambda_L}{3} \begin{pmatrix} 1.731 \\ -0.965 \end{pmatrix} \pm \frac{\lambda_L}{3} \begin{pmatrix} 0.005 \\ 0.005 \end{pmatrix} , \\
 \mathbf{a}_2 &= \frac{2\lambda_L}{3} \begin{pmatrix} -0.010 \\ 1.007 \end{pmatrix} \pm \frac{2\lambda_L}{3} \begin{pmatrix} 0.001 \\ 0.001 \end{pmatrix} , \\
 \mathbf{a}_3 &= \frac{\lambda_L}{3} \begin{pmatrix} 1.710 \\ 1.049 \end{pmatrix} \pm \frac{\lambda_L}{3} \begin{pmatrix} 0.003 \\ 0.003 \end{pmatrix} .
 \end{aligned} \tag{6.9}$$

By calculating the norm of the primitive lattice vectors we can get the corresponding lattice spacings of the different lattice directions. To do this we have to convert the units of the results from camera pixels to the actual length. We already calculated $\lambda_L = 0.0639$ px in units of camera pixels and we know that the actual wavelength of the laser is 1069.8 nm. This results in a conversion factor of 16,751 nm/px. If the triangular lattice would be perfect the lattice spacing would be the same along all three directions. With the known wavelength of the laser the lattice spacing would then be $a = (2/3) \cdot \lambda_L = 713.2$ nm. The spacings resulting from our measurement are:

$$\begin{aligned}
 |\mathbf{a}_1| &= 706.6 \text{ nm} \pm 1.9 \text{ nm} , & |\mathbf{a}_2| &= 718.0 \text{ nm} \pm 0.7 \text{ nm} , \\
 |\mathbf{a}_3| &= 715.4 \text{ nm} \pm 1.2 \text{ nm} .
 \end{aligned} \tag{6.10}$$

Finally we can calculate the lattice spacings of the 1D lattices that we get if we turn on only two of the beams via

$$a_{1D} = \frac{\pi}{k_L \cdot \sin(\alpha/2)} . \tag{6.11}$$

For an ideal triangular lattice this spacing would be $a_{1D} = \lambda_L / \sqrt{3} = 617.6$ nm for all three combinations of two lattice beams. For the lattice angles that we obtained the 1D lattice angles are:

$$\begin{aligned}
 a_\alpha^{1D} &= 613.7 \text{ nm} \pm 0.8 \text{ nm} , & a_\beta^{1D} &= 623.6 \text{ nm} \pm 0.9 \text{ nm} , \\
 a_\gamma^{1D} &= 615.9 \text{ nm} \pm 0.9 \text{ nm} .
 \end{aligned} \tag{6.12}$$

6.2.4 Next steps

A natural next step would be to measure the actual on-site trap frequency that we realize in our lattice via amplitude modulation spectroscopy like for example in [129]. To perform this method the laser power of the optical lattice is modulated with different frequencies in the range where two times the on-site trap frequency is expected to be because this method mainly drives transitions of two harmonic oscillator quanta. A modulation frequency close to twice the trap frequency then leads to

heating and particle loss in the atomic cloud. Amplitude modulation spectroscopy works for bosonic and fermionic systems and is suitable for deep optical lattices.

Another elegant way to get the on-site trap frequency of a deep optical lattice are sideband-resolved Raman spectra. The advantage of this method is that they are measured anyway when Raman sideband cooling is implemented on the way to site-resolved imaging in the optical lattice (see section 7.1).

6.3 Implementation into the experimental cycle

After the discussion of the accordion lattice and the triangular lattice we now want to show how the optical lattices could be implemented in a typical experimental cycle. Therefore, we describe how we load the atoms into a very deep 3D lattice to freeze their spatial position along all directions. This is the starting point for Raman sideband cooling and by this means also for site-resolved imaging of the atoms in the optical lattice.

For the experimental steps that are displayed in figure 6.5 we start with a molecular BEC in a shallow dipole trap as it is the case at the end of the experimental steps that are shown in figure 5.3. First the dipole trap power is ramped linearly to a final value of 1 W within 50 ms. This heats up the atomic cloud but it also squeezes it. The size of the cloud along the vertical direction is reduced in this way such that it is possible to load the complete cloud into a single lattice plane of the accordion lattice if the lattice is tuned to its maximum level spacing of $45\ \mu\text{m}$. For an unsqueezed cloud it is not possible to load all atoms into a single plane of the accordion lattice. In addition to the squeezing we also depend on a high stability of the accordion lattice interference pattern to be able to load only a single plane in many consecutive experimental cycles.

After the squeeze we ramp up the accordion lattice power to 75 mW per beam with a linear slope within 250 ms. In our current setup the accordion lattice can not be turned off completely because we do not want to send the maximum 40 W of laser power through an AOM and it is problematic to switch a lattice laser amplifier on and off in every experimental run due to arising thermal instabilities. Nevertheless, we achieve a very good extinction ratio of the laser power using the motorized rotation mount such that the residual laser light of the accordion lattice does not affect the experimental sequence up to this point.

After the linear power ramp we start with the compression of the cloud to create a two-dimensional sample. A linear ramp of the position of the linear translation stage between its both limit values within 100 ms leads to a decrease of the accordion lattice spacing from $45\ \mu\text{m}$ to $2\ \mu\text{m}$ with the same curve as in figure 6.2.

After the preparation of a 2D sample with the accordion lattice the atoms need to be loaded into the triangular lattice to also create a strong confinement in the horizontal plane. We start with a linear ramp of the laser power in each lattice beam from 0 to 200 mW within 30 ms to adiabatically load the atoms into the triangular lattice.

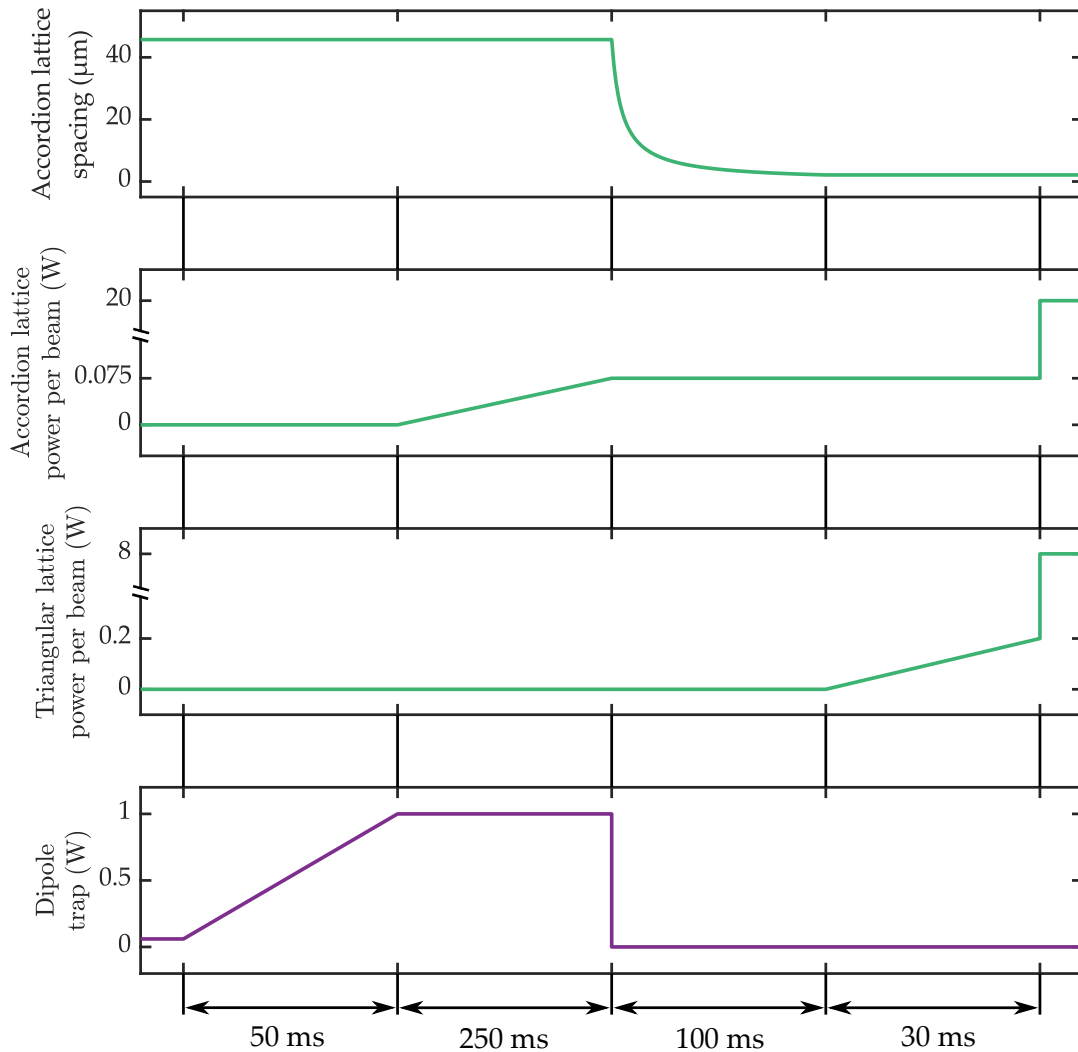


FIGURE 6.5: Timeline of the experimental steps to load the atoms into a deep three-dimensional optical lattice. The traces show the accordion lattice spacing, the laser power per beam for the accordion lattice and the triangular lattice and the power in the dipole trap. The axes for the laser power of the lattice beams are non-linear for better visibility of the respective power ramps.

The linear ramp is driven with the intensity control setup and the lattice beams are switched on at the begin of the ramp using the corresponding AOMs.

Directly after the linear ramp we instantly set the intensity control to its maximum value to ramp up the full power in the triangular lattice beams. A direct jump from 0 to maximum power heats up the atoms too much and they are not captured by the triangular lattice. At the same time we ramp up the power in the accordion lattice beams as fast as possible to the maximum value of 20 W per beam using the motorized rotation mount. By jumping to the full lattice depth along all directions we freeze the spatial position of the atoms.

The described sequence of experimental steps is for example used as the starting point for the observation of Raman spectra in the deep optical lattice as we describe it in section 7.1.3. Similarly it will be the starting point for performing single-atom resolved imaging. But the actual physics that shall be observed and investigated

with the quantum gas microscope is typically implemented between the preparation of the 2D sample with the accordion lattice and the freezing of the position of the atoms by ramping up the full power in the accordion lattice and the triangular lattice at the same time. If we consider experiments on the physics of ultracold atoms in triangular optical lattices we start with adiabatic loading of a moderately deep lattice as a starting point and ramp up the full power later for the imaging process.

The described steps will surely be changed and optimized along the continuing development of the experiment, for example to minimize heating of the atomic cloud during its transfer into the lattices. In addition short timesteps with no changes of experimental parameters might be inserted between some of the described steps such that the system can equilibrate before the start of the next step. Another likely change at some point of the experimental cycle is the implementation of an optical dimple to create a sample with on the one hand a smaller particle number but on the other hand an extremely high degeneracy.

Chapter 7

Preparation of single-atom resolved imaging

As described in the last chapters we are able to create ultracold samples of lithium atoms and to load these atoms into a deep three-dimensional lattice. Nevertheless, two main aspects still need to be implemented for the realization of single-atom resolved imaging: an efficient cooling mechanism for the atoms in the lattice and an imaging setup with a high optical resolution. In this chapter we present our work towards the realization of these ingredients.

The described experimental work has been done by a team consisting of Andreas Kerkmann, Mathis Fischer, Justus Brüggengjürgen and the author under the supervision of Klaus Sengstock and Christof Weitenberg. The displayed data were taken by the same team and the presented analysis of the data was performed by the author.

7.1 Towards Raman sideband cooling

This section is dedicated to our work towards the realization of Raman sideband cooling. We start with describing the procedure to adjust the two Raman beams to the position of the atoms. Next we discuss our first measurement of a broad two-photon Raman transition in the optical dipole trap. A much more narrow resonance is then realized by loading the atoms into the deep 3D lattice. Finally we show our measurements of Rabi oscillations between the two hyperfine states of the ${}^6\text{Li}$ ground state for two different intensities of the Raman beams.

7.1.1 Adjustment of the Raman beams

Before we can start to search for a Raman two-photon resonance in one of our optical traps we have to adjust the two Raman beams to the position of the atoms. We do this for the first Raman beam by switching it on simultaneously with the imaging light when we perform absorption imaging of the gray molasses. The laser light of the Raman beam induces a state-dependent light shift on the ${}^6\text{Li}$ atoms and shifts them out of the resonance of the imaging beam.

Both Raman beams are collimated and have a beam waist radius of approximately $150\ \mu\text{m}$ at the position of the atoms. The first Raman beam (R1) is therefore smaller

than the gray molasses after some expansion time. Due to the light shift the laser beam creates a hole with no atoms in the atomic cloud when it hits the cloud. The center of this hole can be overlapped with the known final position of the atomic cloud when it has been loaded into the deep three-dimensional optical lattice. In this way we realize a good initial adjustment for the first Raman beam. For all measurements described in this section the first Raman beam has a red-detuning of 7.0 GHz to the D1 line of ${}^6\text{Li}$.

As described in section 3.2.3 the second Raman beam (R2) is created by guiding the first Raman beam through a DPAOM which sends the second Raman beam automatically into the opposite direction of the first one. The overlap of the two Raman beams can be optimized with the 0° -mirror of the DPAOM by maximizing the power of the second Raman beam that is coupled back into the PM fiber of the first Raman beam.

7.1.2 Broadened Raman transition in the dipole trap

Raman sideband cooling as it has already been demonstrated in other experiments is performed at zero magnetic field or very small bias fields. We therefore perform our first experiments with the Raman beams with a Fermi gas of ${}^6\text{Li}$ atoms because a Fermi gas can be imaged at zero magnetic field which we can not do for a molecular BEC.

We first want to observe the carrier transition of the two-photon Raman resonance in a Fermi gas trapped in the crossed dipole trap. To avoid the formation of molecules we stop the evaporation, that is again performed at a bias field of 808 G, at a dipole trap laser power of ~ 6 W. At the end of the evaporation we rapidly switch off the bias field of the Feshbach coils using the corresponding IGBT and hence get a Fermi gas at a small magnetic background field. The Raman beams are then turned on in the form of a rectangular pulse for 500 μs by rapidly switching both Raman beams on and off at the same time using the SPAOM in front of the fiber.

To observe the carrier resonance of the Raman spectrum we change the frequency difference δ_{12} between the two Raman beams symmetrically around the hyperfine splitting $E_{HFS} = 228.205\,261$ MHz of the ground state of ${}^6\text{Li}$ between different experimental runs. The position of the carrier resonance is naively expected to lie at zero relative two-photon detuning $\delta = E_{HFS} - \delta_{12}$ between the two Raman beams. After the pulse we perform absorption imaging of the atomic cloud in situ with no ToF.

For all measurements with the Raman beams in this section we use a uniform color code for the two Hyperfine ground states of ${}^6\text{Li}$. If the atom number in the state $F = 1/2$ is imaged, the data and the fits are displayed in orange and for the state $F = 3/2$ the data and the fits are shown in purple. In general we always start with all atoms in the $F = 1/2$ state at the end of the evaporative cooling stage. Thus the atoms begin to disappear in the $F = 1/2$ state and begin to appear in the $F = 3/2$ state when we hit a two-photon Raman resonance with the Raman beams. To find

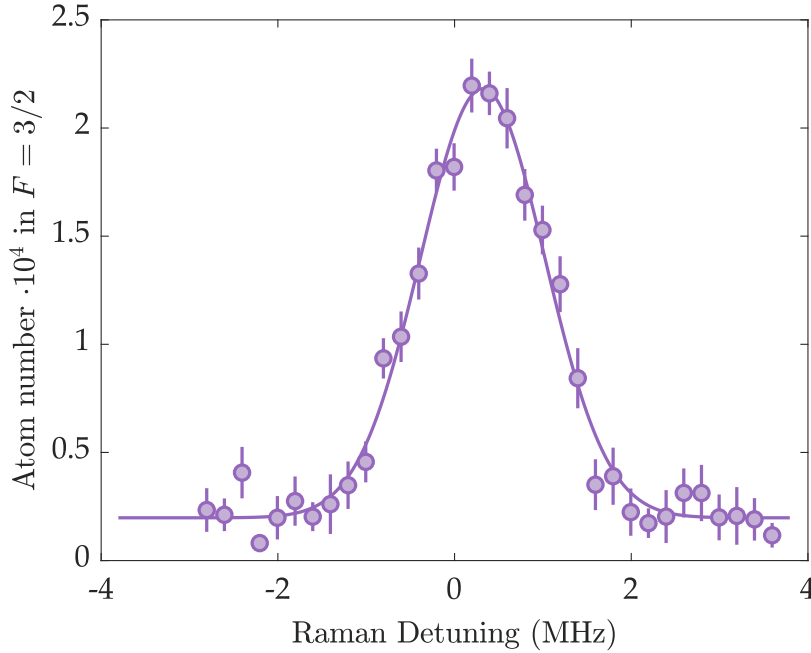


FIGURE 7.1: Raman carrier resonance of the two-photon transition between the Hyperfine ground states of ${}^6\text{Li}$ in the optical dipole trap. The data points show the particle number in the $F = 3/2$ state which is derived from a gaussian fit to the in situ distribution of the atomic cloud. The errorbars are the 1σ uncertainty of the particle number derived from the uncertainty of the fit results. The Doppler broadened resonance profile is then fitted with a gaussian function which has a FWHM of 1.657 MHz.

a resonance we usually first look for atoms disappearing in the $F = 1/2$ state and then check if they actually appear in the $F = 3/2$ state for the same experimental parameters. In this way we assure that we actually drive a two-photon transition and do not only see atoms disappearing due to off-resonant heating by the Raman beams.

The result of the described measurement of the Raman carrier resonance in the dipole trap is shown in figure 7.1. The Fermi gas is not very degenerate here which leads to Doppler broadening of the resonance profile. Due to this inhomogeneous broadening effect the data can be well fitted with a gaussian instead of a Lorentzian function. The latter one would be expected for a resonance profile that exhibits no line broadening effects. The gaussian fit to the resonance profile has a full width at half maximum (FWHM) of 1.657 MHz and the center of the fitted profile has an offset of 0.32 MHz to the expected relative frequency difference $\delta = E_{HFS} - \delta_{12} = 0$. This offset may result from Raman transitions on blue sidebands. Due to the fact that we are not in the sideband-resolved regime here we only measure a single resonance with a shifted center. The small offset in the atom number of the data points that are off-resonance results from the fact that is in general difficult for a fitting algorithm to precisely discriminate between an absorption image with a small number of atoms and an image with no atoms at all. But when we look at the absorption images taken with off-resonant Raman beams we can not see any atoms at all in the $F = 3/2$ state. For such a broad linewidth as measured here we can not expect to

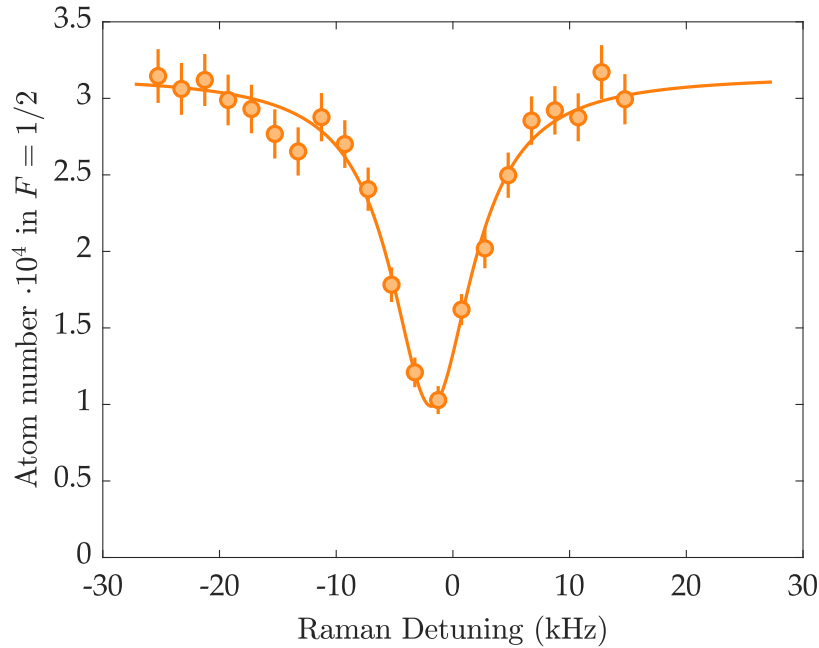


FIGURE 7.2: Raman carrier resonance of the two-photon transition between the hyperfine ground states of ${}^6\text{Li}$ in the 3D optical lattice. Here the data points show the particle number in the $F = 1/2$ state. The errorbars display the 1σ uncertainty of the particle number. A fit to the data points with a Lorentzian function has a FWHM of 8.5 kHz.

observe Rabi oscillations but by observing the Raman resonance at all we assure the basic functionality of our Raman setup.

7.1.3 Narrow Raman transition in the 3D lattice

To realize site-resolved imaging of individual atoms we want to realize Raman sideband cooling in the 3D optical lattice. Hence, the next step is to look at the two-photon Raman transition in the lattice. We start with loading a cold Fermi gas directly into a deep accordion lattice with narrow spacing and afterwards into the deep triangular lattice as it was similarly described in section 6.3. In this way the atoms are confined stronger than in the dipole trap along all spatial directions. This leads to a reduction of Doppler broadening of the Raman resonance and we see indeed a much more narrow resonance. Therefore, we have to step through a smaller frequency interval than in the dipole trap to resolve the shape of this resonance.

The measured resonance is displayed in figure 7.2. For this measurement we image the $F = 1/2$ state and hence the two-photon resonance appears as a dip in the atom number and not as a peak. Here the resonance profile is fitted by a Lorentzian function with a FWHM of 8.5 kHz. In contrast to the measurement of the resonance profile in the dipole trap the rectangular Raman pulse here has a length of only $100\ \mu\text{s}$ which leads to Fourier broadening for features smaller than 10 kHz. Thus the width of the Raman resonance might be limited by Fourier broadening. The small shift of the center of the fit can result from a shift of the energy of the hyperfine states due to background magnetic fields. We might not be able to precisely determine the

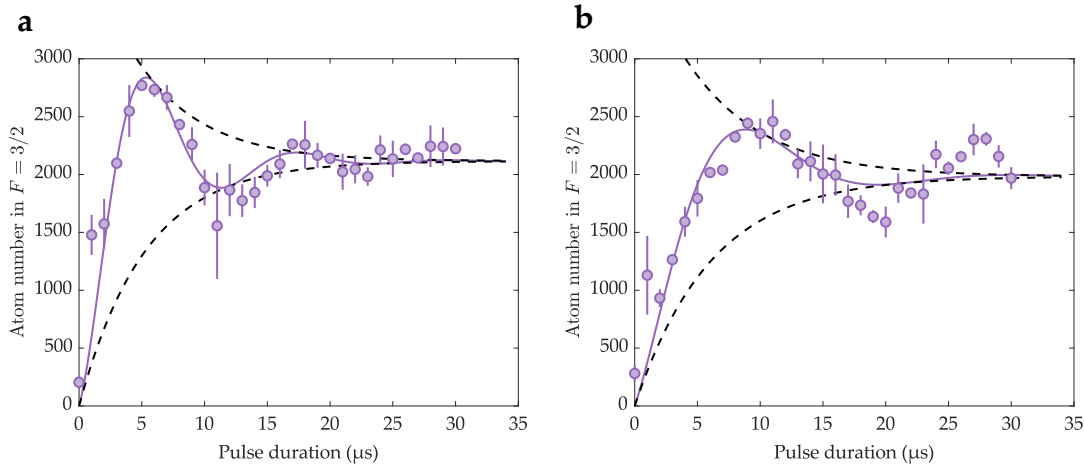


FIGURE 7.3: Rabi oscillations for two different laser powers in the Raman beams. Halving the laser power leads to a halving of the Rabi frequency in (b) compared to (a). The data points are the mean of five iterations and the errorbars are the 1σ standard deviation of this mean. The purple curves are a fit to the data and the dashed black lines show the damping part of the fit results.

width of the Raman resonance here but we can at least specify an upper limit for it. Next we take this much more narrow transition in the 3D lattice as a starting point to look for Rabi oscillations.

7.1.4 Rabi oscillations

For the observation of Rabi oscillations in the deep optical lattice we use an experimental sequence that is similar to the one described in the last section. But in this case the frequency detuning of the two Raman lasers is fixed at the position of the measured resonance and the length of the Raman pulse is varied to observe the time-dependent oscillation between the two hyperfine states. We perform this measurement for two different laser powers of the Raman beams to observe the intensity dependence of the Rabi oscillation.

The results of this measurement are shown in figure 7.3. We are able to observe Rabi oscillations even though they are strongly damped. In figure 7.3 (a) the power in the first Raman beam is ~ 12 mW and in figure 7.3 (b) it is ~ 6 mW. The DPAOM that creates the second Raman beam is adjusted for all measurements in this section such that the power in the second beam is maximized. Due to the finite efficiency of the DPAOM the power in the second Raman beam is limited to approximately 85% of the power in the first Raman beam. The data points are the mean of five iterations for every timestep and the errorbars show the 1σ standard deviation of this mean. We fit the data according to [130] using the function

$$N_{3/2}(t) = \frac{N_0}{2} \left(1 - \cos(2|\Omega|t) e^{-\frac{3}{4}\Gamma t} \right) , \quad (7.1)$$

with N_0 the number of atoms in the $F = 1/2$ state at $t = 0$, Ω the Rabi frequency and Γ the damping rate as free fit parameters. The blue curves are the fit results and

the dashed black lines show only the damping part $e^{-\frac{3}{4}\Gamma t}$ of the fit function. For the higher laser power in the Raman beams in figure 7.3 (a) the resulting two-photon Rabi frequency is $\Omega = 2\pi \cdot 42$ kHz and the damping rate is $\Gamma = 2\pi \cdot 253$ kHz. For the halved laser power in the Raman beams in figure 7.3 (b) we get as expected a halved two-photon Rabi frequency of $\Omega = 2\pi \cdot 24$ kHz. The damping rate of $\Gamma = 2\pi \cdot 220$ kHz is of the same order as in the first measurement. When we compare our results here to already existing quantum gas microscopes [68, 103, 131], we are optimistic that we should be able to achieve Raman sideband cooling in the optical lattice.

7.1.5 Next steps

By loading the atoms into the deep optical lattice we should be able to get into the sideband-resolved regime. So the next natural step on the way towards Raman sideband cooling is to look for the red and blue sidebands. If they are found we can then try to actually cool the atoms by adding a repumper beam. In addition the measurement of the red and blue sidebands also is an elegant way to measure the actual on-site trap frequencies of the pinning lattice. At the time this thesis is written we see first signals of red and blue sidebands in our data. Even though the results are not conclusive enough yet to be presented in this thesis we are optimistic that they will be in the near future.

7.2 Implementation of high-resolution imaging

Besides our work towards Raman sideband cooling we also start to prepare our experimental setup for high-resolution imaging. As described in section 3.6 the 2'' tube lens in our aspired imaging setup has a focal length of $f = 2000$ mm which, in combination with the effective focal length $f = 24.7$ mm of the objective, results in a magnification of $M \approx -80$. We expect this to be a suitable magnification to realize site-resolved imaging on our electron-multiplying charge-coupled device (EMCCD) camera.

Before the installation of the objective we had a useful auxiliary imaging setup in which the imaging beam was propagating along the z-direction coming from the same outcoupler as the upper vertical 3D-MOT beam. After the installation of the objective this imaging setup became impractical because the large imaging beam strongly diverged after passing through the objective. Therefore, we built up a new imaging setup in which the imaging beam was much smaller, had a focus in front of the objective and hence was less divergent behind the objective. This beam was sent in with an angle to the z-axis because the z-axis is blocked by the optics of the 3D-MOT beam. For this imaging setup the objective already needs to be focused on the atoms. As a tube lens we used a plano-convex lens with a focal length of $f = 250$ mm. With this setup we measured for example the Kapitza-Dirac peaks that

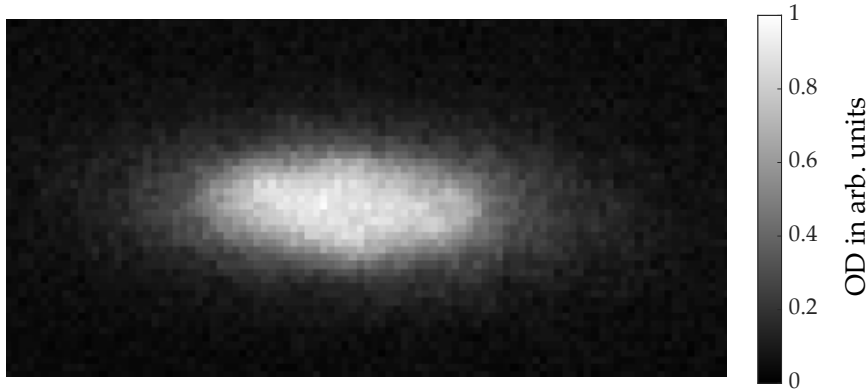


FIGURE 7.4: Absorption image of a molecular BEC taken with the EMCCD camera in the imaging setup with a magnification of $M \approx -40$. 4×4 pixel binning is applied to enhance the signal which is relatively low in the original image due to the distribution to many pixels.

were shown in figure 6.3. The image of the Kapitza-Dirac peaks were also used to calibrate the magnification of this imaging setup to be $M = 8.7(1)$ [18].

For the auxiliary imaging setup we used a *pixelfly usb* CCD camera by the company *PCO Imaging* which has 1392×1024 pixels and a pixel size of $6.45 \mu\text{m}$. When we begin to iterate our setup towards high-resolution imaging we exchange it with the *Andor iXon Ultra 897* EMCCD camera by the company *Oxford Instruments* which has 512×512 pixels and a pixel size of $16 \mu\text{m}$. The direct implementation of an imaging setup with a very large magnification can be technically challenging. We therefore start with the existing setup and iterate towards higher magnifications by stepwise increasing the focal length of the tube lens and readjusting the imaging setup after every exchange of the lens.

The procedure works in the following way: The EMCCD camera and the tube lens are placed on the breadboard such that a $4f$ imaging setup is realized as good as possible. We then adjust the distance between the tube lens and the camera by adding auxiliary mirrors and bringing the camera into focus with an object, which is as far away as possible in the lab, by moving the tube lens. Now the distance between the atomic cloud and the objective and the distance between the tube lens and the EMCCD camera are already adjusted to a degree that enables absorption imaging with this setup. Due to the increasing magnification the imaging beam becomes continuously larger at the position of the camera with every new lens. Hence, we have to search for the position of the atomic cloud in the imaging beam after the adjustment of a new tube lens by varying the part of the beam that is hitting the camera using a 2" inch mirror that is installed between the objective tower and the camera.

In this way we stepwise increase the focal length of the tube lens to $f = 1000 \text{ mm}$ and hence get a magnification of $M \approx -40$. We stop there for now because this magnification is more useful for the things that we do in the experiment at the moment but it is straightforward to go to $M \approx -80$ when we aim for site-resolved imaging.

In figure 7.4 an absorption image is shown that was taken by the EMCCD camera

with deactivated electron-multiplying gain in this imaging setup with a magnification of $M \approx -40$. For this in situ image of a molecular BEC of ${}^6\text{Li}$ dimers 4×4 pixel binning is applied because in the original image the signal is distributed to a lot of pixels due to the high magnification such that the signal per pixel becomes relatively weak. Such an image can be acquired with the described procedure without further adjustment of any element in the imaging setup.

The realization of nearly diffraction-limited imaging with our $\text{NA} = 0.5$ objective to resolve single atoms on individual lattice sites is of course much more difficult. The shown BEC is too large and has no sharp features. Hence, it is not useful to adjust the imaging setup with higher precision. We have to create smaller objects to be able to do this such as atoms in a dimple trap with a very small beam waist. Another possibility to adjust the objective is to determine the imaging response function from in situ images of a 2D thermal gas [132]. Finally we can try to directly adjust the objective to the signal of single atoms on individual lattice sites. Besides the realization of sufficient Raman sideband cooling the precise adjustment of the objective remains the main challenge on our way towards single-atom resolved imaging.

Chapter 8

Conclusion & Outlook

In this final chapter we start with a conclusion of the work that is presented in this thesis. We mention some of the next experimental steps that need to be performed next and we have a look at some of the many interesting physical systems that we can explore with our experimental apparatus.

8.1 Conclusion

The goal of this PhD thesis was the design and setup of a new experiment for quantum gas microscopy of small samples of bosonic and fermionic lithium atoms. First we motivated the choice of lithium as the atomic species for our cold atom experiment and the quantum gas microscope as the technique that we want to use for our experiment. While discussing the basics of a quantum gas microscope we introduced the accordion lattice and the triangular lattice as our pinning lattices and Raman sideband cooling as the method to cool the atoms in these lattices.

Next we introduced the details of our experimental setup including among other things the vacuum chamber, the laser systems for the creation of near-resonant light, the crossed dipole trap, the optical lattices and the high-resolution imaging setup. An extra chapter was dedicated to the design, construction and implementation of the magnetic field coils. We described the possible magnetic field configurations and the necessary infrastructure for providing high electrical currents and sufficient water cooling of the coils.

Then we turned to the first experiments that we performed with our new machine. We displayed a typical experimental sequence with the steps 2D- and 3D-MOT, compressed MOT, gray molasses and evaporative cooling in the dipole trap for the creation of ultracold quantum gases of ${}^6\text{Li}$. Afterwards we discussed the adjustment and characterization of the accordion lattice, which loads the atoms from the dipole trap and dynamically squeezes them into the two-dimensional regime, and the triangular lattice that can either be used as a physics lattice, a pinning lattice or as both in the same experimental sequence. Next we described the measurement of Raman spectra and Rabi oscillations as first steps towards Raman sideband cooling. Finally we implemented an imaging setup with a large magnification to get into the regime where individual atoms can become visible.

8.2 Upcoming experimental steps

As described in section 7.1 we are working towards Raman sideband cooling in our experiment. We are optimistic that we will soon have conclusive measurements of the red and blue sidebands of the two-photon Raman transition. We then can strive for actually cooling the atoms by adding a repumper beam. A clear signature of the atoms being cooled to the lowest harmonic oscillator level would be the suppression of the red sidebands. If a cooling effect is visible we can test how long we can hold the atoms in the lattice with Raman sideband cooling without significant loss of atoms compared to not cooling the sample. This can only be a first measure for the efficiency of the cooling mechanism because hopping of atoms to other lattices during the imaging process also prohibits single-site resolution.

Based on a simulation that has been performed by Jan Mika Jacobsen during his Master's thesis [110] and based on the experience of existing quantum gas microscopes we expect the number of photons that we have to collect per atom to be ~ 150 for our setup. As the overall collection efficiency will not significantly exceed 5% every atom needs to scatter ~ 3000 photons during the imaging process that can not be significantly longer than 1 s. In [110] very realistic quantum gas microscope images were simulated and then these images were used to test different algorithms for the reconstruction of the lattice site occupation numbers. We are also working towards applying deep learning techniques for the reconstruction of quantum gas microscopes images [133] in a similar way as it has been proposed in [134]. This might reduce the number of photons per atom that need to be collected for reliable reconstruction of the measured images. Applying deep learning to this problem is a natural next step as these methods already have been applied in several quantum gases experiments [135–137].

Another important experimental step is the implementation of a small dimple trap. By loading a small number of atoms from a larger reservoir a sample with complete occupation of the lowest energy levels can be created. This is a requirement for the deterministic preparation of a small particle number in 1D [63] or 2D [64]. Such a dimple can be created by sending a red-detuned laser beam through the objective. Due to the high numerical aperture of the objective the dimple beam will have the desired small waist. As a consequence of the small waist the laser power of the dimple can be relatively low compared to other off-resonant optical traps like the dipole trap or the optical lattices. As the dimple trap is a very small object it can also be a good tool for the fine adjustment of the objective which is another important task that has to be done to realize a quantum gas microscope. In addition we will benefit from the experience in precisely adjusting the objective that we gained in a separate test setup [111].

Devices that are becoming more and more common in experiments with ultracold

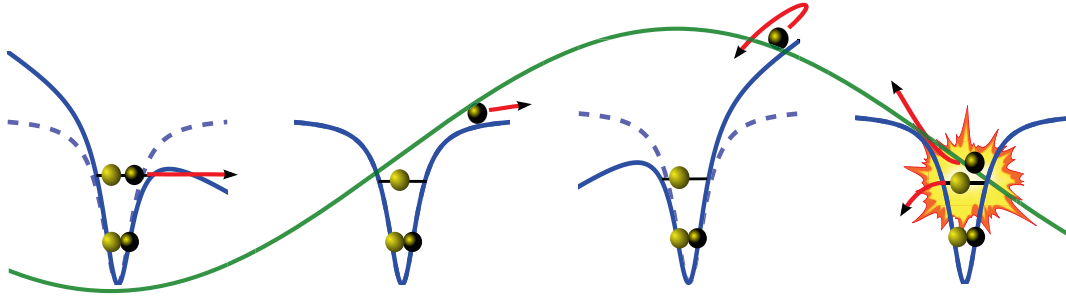


FIGURE 8.1: Proposal for the simulation of non-sequential double ionization with ultracold atoms. A dipole trap (dashed blue) that contains four atoms in two different spin states (yellow, black) is tilted with an oscillating magnetic field gradient (green). One atom first tunnels through the barrier that is reduced due to the resulting tilt of the overall potential (blue). As the direction of the tilt changes the atom is accelerated and recollides with the other atom in its initial state. The result is that both atoms leave the trap. Image taken from [142].

atoms are spatial light modulators for the creation of nearly arbitrary optical potentials [138]. Even though the laser power that can be sent into these potentials is relatively low they have already enabled several remarkable experiments that have not been possible before, for example the redistribution of entropy for the preparation of quantum states with very low temperatures [39, 40]. In the team of our experiment a setup based on a digital micromirror device (DMD) has been implemented [139, 140] to enable us to also create all the potentials that might be needed for the possible future research topics that we present in the next section. Moreover dynamical modulation of these potentials has recently been implemented in our setup [141].

8.3 Prospective research topics

A lot of the work that has been done in the quantum gases community up to now has focused on quantum simulation of solid state systems in the sense that the ultracold atoms mimic the electrons and the optical lattices imitate the potential of the atomic cores. But there are also several proposals and experiments where ultracold atoms are used for the simulation of other physical systems. We now want to focus on proposals to simulate atomic [142] and molecular [143] dynamics that could be implemented in our experiment.

On the atomic side the electronic shells of an atom could be mimicked by the energy levels of an optical potential which could for example be tailored with the DMD that was mentioned in the last section. By making use of the already discussed deterministic preparation of a small atom number different shell structures and fillings could be realized [63, 64]. In consequence such an experiment needs to be performed with fermionic atoms. Atomic dynamics generally happen on the timescale of attoseconds. The field of research of attosecond science is dedicated to the resolution of this extremely fast processes by using intense ultrashort light pulses [144]. Hence it is a fascinating idea to use the intrinsically much slower dynamics of ultracold atoms to

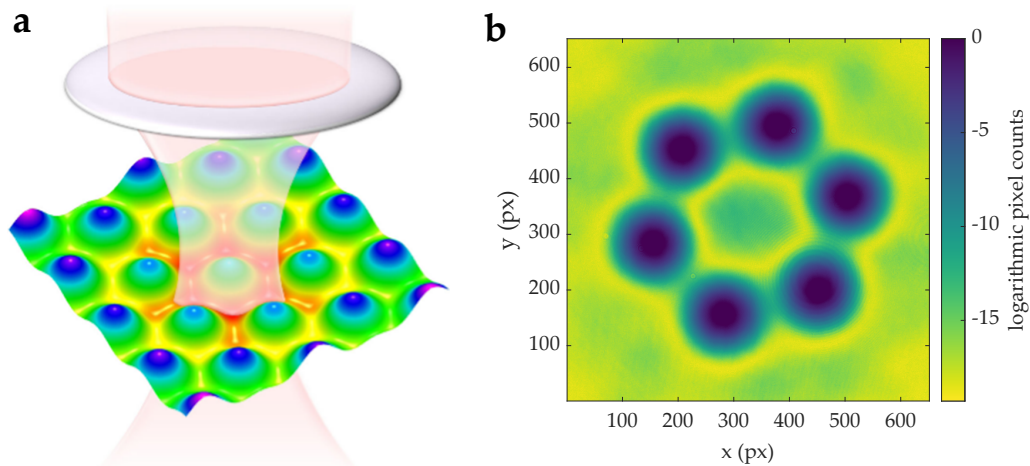


FIGURE 8.2: Two possibilities to create an artificial benzene molecule for the simulation of molecular orbitals and dynamics. (a) A single hexagon of a hexagonal optical lattice structure is selected by using a small dipole trap. Image taken from [143]. (b) Six optical traps in a hexagonal structure are created with a DMD. We choose a logarithmic color scale for better visibility of experimental imperfections. Figure adapted from [18] where the data were taken from [139].

try to imitate some of the many interesting phenomena of this physical regime like the Auger effect or non-sequential double ionization (see figure 8.1). The strong light field in attosecond science could be mimicked by an alternating magnetic field gradient or an additional laser beam in a cold atom experiment. In addition excitations could be implemented into the system by amplitude modulation of the optical trap. The tuning of the interaction strength between the atoms by making use of the broad Feshbach resonance of both lithium isotopes could also be an interesting addition to these type of experiments. A first experiment in this direction has been carried out in which a BEC of strontium atoms mimics the electron wave packet [145]. We want to expand this kind of experiment to the single-atom level using a quantum gas microscope in the described way.

The simulation of an artificial benzene molecule that is proposed in [143] follows a related approach. By overlapping a small dipole trap with a hexagonal optical lattice, as it is shown in figure 8.2 (a), a single hexagon of the lattice structure can be selected. Every lattice site of this hexagon needs to be prepared with a single atom. An alternative approach is displayed in figure 8.2 (b) where six individual optical traps in a hexagonal configuration are realized using a DMD. With one of these configurations the molecular orbitals of the artificial benzene ring could be studied via momentum-space mapping even without the need for site-resolved imaging. Removing one of the atoms or again tuning their interaction will lead to interesting dynamics which could be studied in this setup.

Other interesting proposals which our experimental setup should be suited to realize include for example the implementation of supersymmetric dynamics with one atom in the ground state of a harmonic trap [146] and the analysis of spectral properties and breathing dynamics of a few-body Bose-Bose mixture in a 1D harmonic

trap [147]. For the investigation of bulk systems like the latter one there is the problem that the pinning lattice of a quantum gas microscope distorts the original density distribution if the structure of the bulk system is on the order of the pinning lattice spacing. An additional proposal suggests the implementation of a so-called quantum point spread function as a solution for this issue [62].

Finally another possible direction for our experiment is the very interesting regime of ultracold atoms in rapidly rotating optical traps [148]. The trap rotation creates an artificial magnetic field for the atoms. In the limit of only a few particles quasihole excitations from the ground state are expected to have anyonic properties. Anyons are quantum particles that behave neither like a boson or a fermion. The statistical phase θ they acquire by an interchange can be anything between the limits of a boson ($\theta = 0$) and a fermion ($\theta = \pi$). In condensed matter physics anyons are believed to be closely related to the fractional quantum Hall effect. The single-particle resolution of a quantum gas microscope can be an important ingredient towards the measurement of anyons with ultracold atoms and the exploration of their properties.

Appendix A

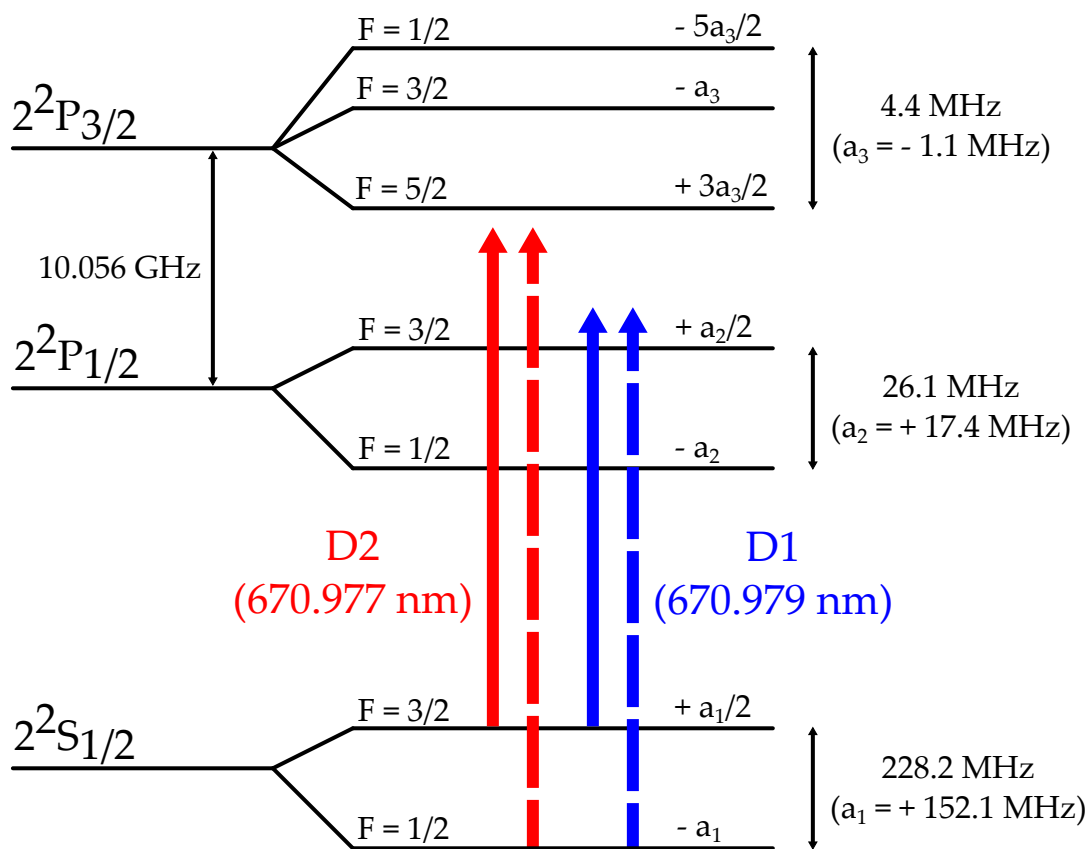
Level diagram of ${}^6\text{Li}$ 

FIGURE A.1: Level diagram of the ground state and the $2P$ excited state of ${}^6\text{Li}$. The energy splittings are not to scale. The $D2$ transition is used for the red-detuned 2D- and 3D-MOT and the $D1$ transition is used for the blue-detuned gray molasses. The solid arrows correspond to the cooler transitions and the dashed lines indicate the repumper transitions. Data taken from [149, 150].

Appendix B

Magnetic field shift of ${}^6\text{Li}$

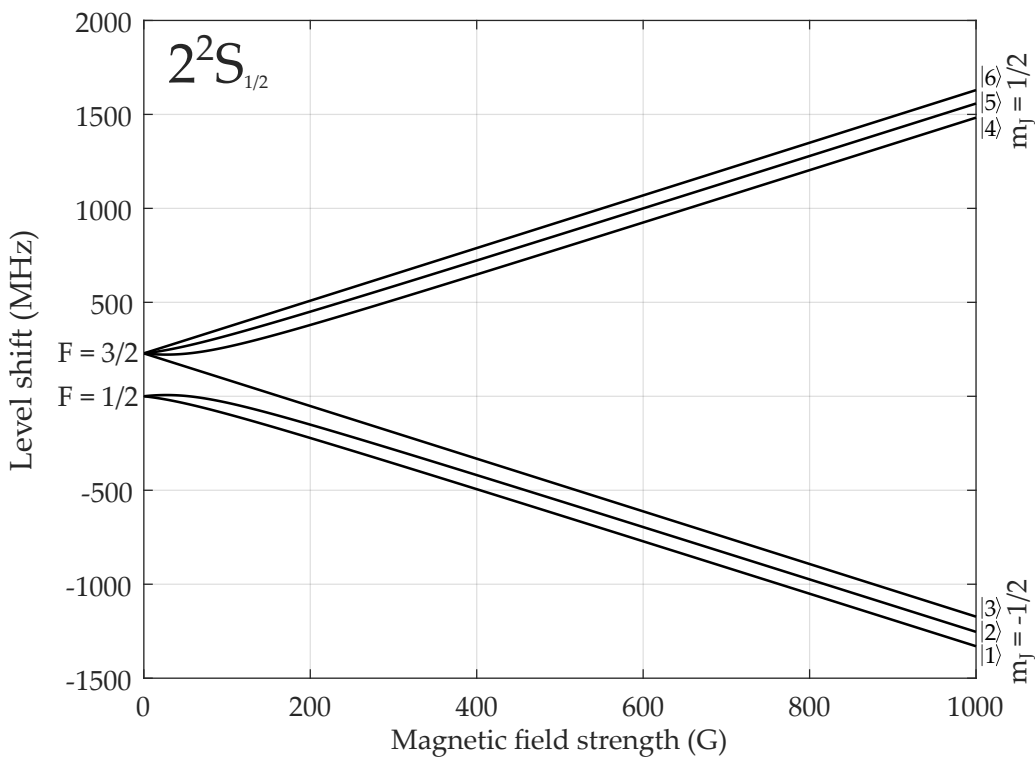


FIGURE B.1: Magnetic field dependence of the $2^2S_{1/2}$ ground state of ${}^6\text{Li}$. ${}^6\text{Li}$ enters the Paschen-Back regime at relatively low magnetic fields and the states regroup according to the m_j quantum number. The energy difference within a subgroup is ~ 80 MHz. The Paschen-Back states of the ground state are typically labeled from $|1\rangle$ to $|6\rangle$ in energetic order. We have only worked with the high-field seeking states $|1\rangle$ to $|3\rangle$ in our experiment up to now. Hence in the discussion of magnetic fields and the design of our coils (see chapter 4) we always consider only these states. Image taken from [18] where the data for the plot was taken from [20].

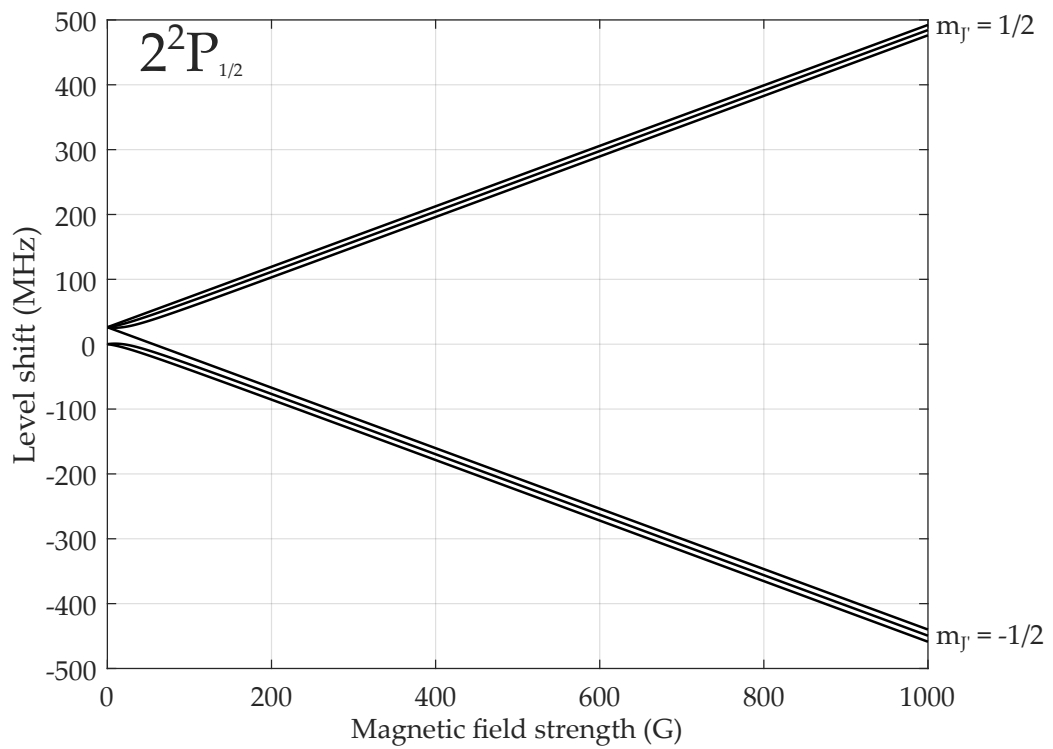


FIGURE B.2: Magnetic field dependence of the $2^2P_{1/2}$ excited state of ${}^6\text{Li}$. In this state ${}^6\text{Li}$ enters the Paschen-Back regime at lower magnetic fields than in the ground state. The states regroup according to the m_J quantum number. The energy difference within a subgroup is ~ 10 MHz. Image taken from [18] where the data for the plot was taken from [20].

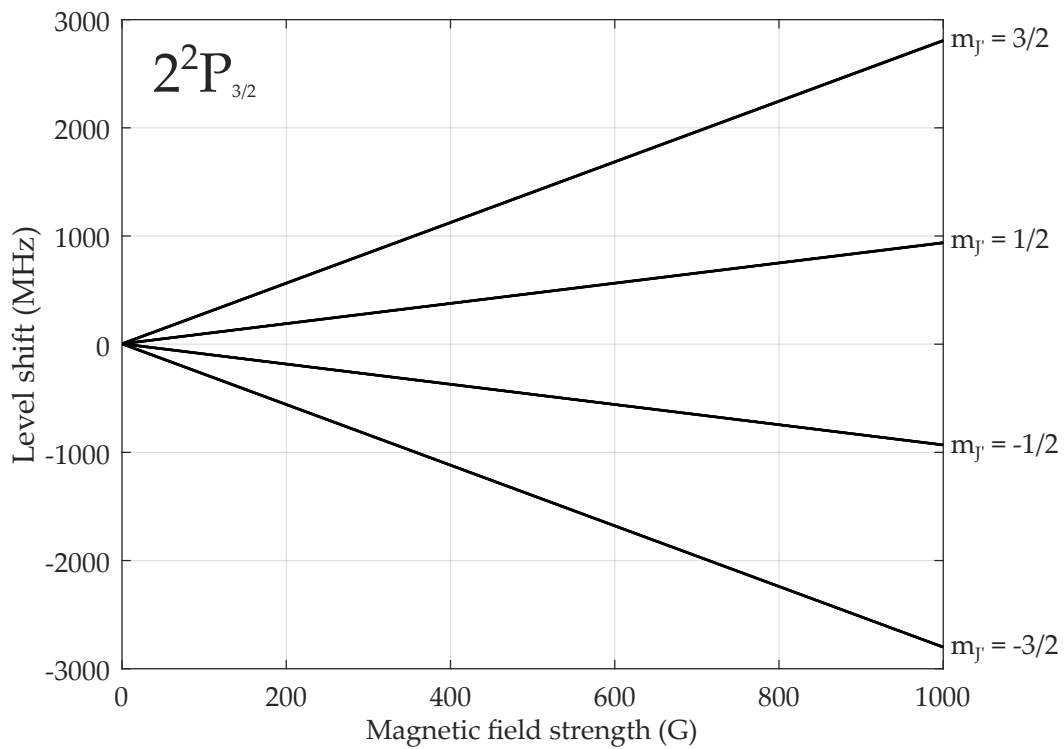


FIGURE B.3: Magnetic field dependence of the $2^2P_{3/2}$ excited state of ${}^6\text{Li}$. In this state ${}^6\text{Li}$ enters the Paschen-Back regime at even lower magnetic fields than in the $2^2S_{1/2}$ ground state and in the $2^2P_{1/2}$ excited state. The states regroup according to the $m_{J'}$ quantum number. The energy difference within a subgroup is ~ 2 MHz. Image taken from [18] where the data for the plot was taken from [20].

Appendix C

Feshbach resonances of ${}^6\text{Li}$

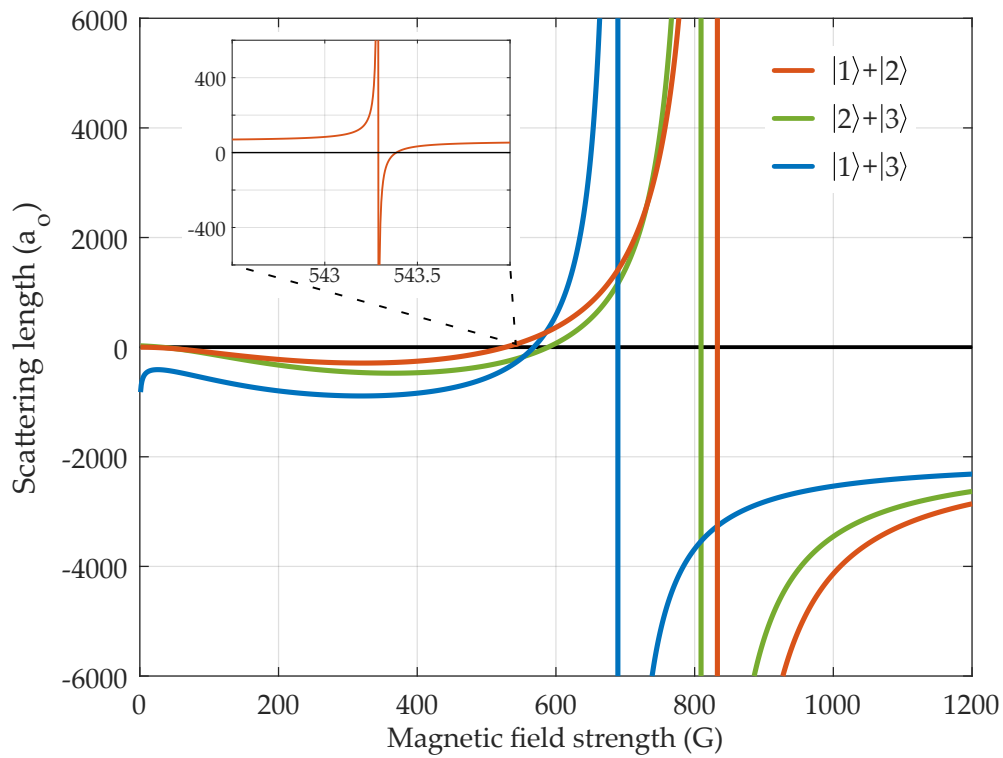


FIGURE C.1: Broad Feshbach resonances between the three lowest Paschen-Back states of ${}^6\text{Li}$. The inset shows an additional narrow resonance of the states $|1\rangle$ and $|2\rangle$ at 543.286(3) G which has a width of 0.10(1) G and a background scattering length of $\simeq 62 a_0$ [151]. Image taken from [18] where the data for the plot was taken from the supplemental material of [152].

Appendix D

Analysis of Kapitza-Dirac peaks

TABLE D.1: All values derived from the analysis of the Kapitza-Dirac peaks. The calculation and the conversion from camera pixels to SI units are explained in section 6.2.3.

	Camera pixel		SI units	
p_1	$\begin{pmatrix} 170.0 \\ 3.8 \end{pmatrix}$	$\pm \begin{pmatrix} 1.7 \\ 1.1 \end{pmatrix}$		
p_2	$\begin{pmatrix} 79.5 \\ 147.4 \end{pmatrix}$	$\pm \begin{pmatrix} 1.3 \\ 1.1 \end{pmatrix}$		
p_3	$\begin{pmatrix} -94.1 \\ 144.3 \end{pmatrix}$	$\pm \begin{pmatrix} 1.6 \\ 1.0 \end{pmatrix}$		
p_4	$\begin{pmatrix} -172.5 \\ 0.2 \end{pmatrix}$	$\pm \begin{pmatrix} 1.2 \\ 1.1 \end{pmatrix}$		
p_5	$\begin{pmatrix} -85.3 \\ -147.3 \end{pmatrix}$	$\pm \begin{pmatrix} 1.8 \\ 1.0 \end{pmatrix}$		
p_6	$\begin{pmatrix} 85.1 \\ -147.3 \end{pmatrix}$	$\pm \begin{pmatrix} 1.8 \\ 0.9 \end{pmatrix}$		
b_1	$\begin{pmatrix} 171.3 \\ 1.8 \end{pmatrix}$	$\pm \begin{pmatrix} 1.8 \\ 2.8 \end{pmatrix}$	$\sqrt{3} k_L \begin{pmatrix} 1.005 \\ 0.011 \end{pmatrix}$	$\pm \sqrt{3} k_L \begin{pmatrix} 0.011 \\ 0.017 \end{pmatrix}$
b_2	$\begin{pmatrix} 82.4 \\ 147.3 \end{pmatrix}$	$\pm \begin{pmatrix} 4.1 \\ 0.1 \end{pmatrix}$	$\frac{\sqrt{3} k_L}{2} \begin{pmatrix} 0.967 \\ 1.729 \end{pmatrix}$	$\pm \frac{\sqrt{3} k_L}{2} \begin{pmatrix} 0.048 \\ 0.001 \end{pmatrix}$
b_3	$\begin{pmatrix} -89.6 \\ 145.8 \end{pmatrix}$	$\pm \begin{pmatrix} 6.4 \\ 2.1 \end{pmatrix}$	$\frac{\sqrt{3} k_L}{2} \begin{pmatrix} -1.051 \\ 1.711 \end{pmatrix}$	$\pm \frac{\sqrt{3} k_L}{2} \begin{pmatrix} 0.075 \\ 0.025 \end{pmatrix}$
k_1	$\begin{pmatrix} -3.1 \\ 98.3 \end{pmatrix}$	$\pm \begin{pmatrix} 0.4 \\ 0.1 \end{pmatrix}$	$k_L \begin{pmatrix} -0.031 \\ 1.000 \end{pmatrix}$	$\pm k_L \begin{pmatrix} 0.004 \\ 0.001 \end{pmatrix}$
k_2	$\begin{pmatrix} 86.2 \\ -47.3 \end{pmatrix}$	$\pm \begin{pmatrix} 0.2 \\ 0.1 \end{pmatrix}$	$\frac{k_L}{2} \begin{pmatrix} 1.753 \\ -0.963 \end{pmatrix}$	$\pm \frac{k_L}{2} \begin{pmatrix} 0.004 \\ 0.002 \end{pmatrix}$
k_3	$\begin{pmatrix} -85.3 \\ -49.1 \end{pmatrix}$	$\pm \begin{pmatrix} 0.3 \\ 0.2 \end{pmatrix}$	$\frac{k_L}{2} \begin{pmatrix} -1.733 \\ -0.998 \end{pmatrix}$	$\pm \frac{k_L}{2} \begin{pmatrix} 0.005 \\ 0.005 \end{pmatrix}$

Camera pixel		SI units		
α		121.3°	±	0.3°
β		118.1°	±	0.3°
γ		120.6°	±	0.3°
\mathbf{a}_1	$\begin{pmatrix} 0.03684 \\ -0.02054 \end{pmatrix} \pm \begin{pmatrix} 0.00011 \\ 0.00011 \end{pmatrix}$	$\frac{\lambda_L}{3} \begin{pmatrix} 1.731 \\ -0.965 \end{pmatrix}$	±	$\frac{\lambda_L}{3} \begin{pmatrix} 0.005 \\ 0.005 \end{pmatrix}$
\mathbf{a}_2	$\begin{pmatrix} 0.00043 \\ 0.04286 \end{pmatrix} \pm \begin{pmatrix} 0.00004 \\ 0.00004 \end{pmatrix}$	$\frac{2\lambda_L}{3} \begin{pmatrix} -0.010 \\ 1.007 \end{pmatrix}$	±	$\frac{2\lambda_L}{3} \begin{pmatrix} 0.001 \\ 0.001 \end{pmatrix}$
\mathbf{a}_3	$\begin{pmatrix} 0.03641 \\ 0.02233 \end{pmatrix} \pm \begin{pmatrix} 0.00007 \\ 0.00007 \end{pmatrix}$	$\frac{\lambda_L}{3} \begin{pmatrix} 1.710 \\ 1.049 \end{pmatrix}$	±	$\frac{\lambda_L}{3} \begin{pmatrix} 0.003 \\ 0.003 \end{pmatrix}$
$ \mathbf{a}_1 $		706.6 nm	±	1.9 nm
$ \mathbf{a}_2 $		718.0 nm	±	0.7 nm
$ \mathbf{a}_3 $		715.4 nm	±	1.2 nm
a_α^{1D}		613.7 nm	±	0.8 nm
a_β^{1D}		623.6 nm	±	0.9 nm
a_γ^{1D}		615.9 nm	±	0.9 nm

List of Abbreviations

1D	1-Dimension(al)
2D	2-Dimension(al)
3D	3-Dimension(al)
AOM	Acousto-Optic-Modulator
AR	Anti-Reflective
BEC	Bose-Einstein Condensate
CCD	Charge-Coupled Device
CL	Cylindrical Lens
cMOT	compressed Magneto-Optical Trap
D1	$2^2S_{1/2}$ - $2^2P_{1/2}$ transition (see appendix A)
D2	$2^2S_{1/2}$ - $2^2P_{3/2}$ transition (see appendix A)
DFB	Distributed FeedBack
DL	Diode Laser
DMD	Digital Micromirror Device
DPAOM	Double-Pass AOM
ECDL	External Cavity Diode Laser
EOM	Electro-Optic Modulator
FC	Feshbach Coils
FWHM	Full Width at Half Maximum
HWP	Half-Wave Plate
IGBT	Insulated-Gate Bipolar Transistor
IP	Internet Protocol
mBEC	molecular BEC
MC	MOT Coils
MOSFET	Metal-Oxide-Semiconductor Field-Effect Transistor
MOT	Magneto-Optical Trap
NA	Numerical Aperture
OD	Optical Density
PBS	Polarizing Beam Splitter
PD	PhotoDiode
PID	Proportional Integral Derivative
PM	Polarization Maintaining
QWP	Quarter-Wave Plate
RF	Radio Frequency
SI	Système International d'unités

SPAOM	Single-Pass AOM
TA	Tapered Amplifier
TCP	Transmission Control Protocol
ToF	Time-of-Flight
TTL	Transistor-Transistor Logic

List of Figures

2.1	Fluorescence image of individual ^{87}Rb atoms	7
2.2	Working principle of the accordion lattice	10
2.3	Setup and interference pattern of a triangular lattice	12
2.4	Principle of Raman sideband cooling for ^6Li	15
3.1	Vacuum chamber and science cell shown in a vertical cut	18
3.2	View into the 2D-MOT steel chamber	19
3.3	Raman laser system	25
3.4	Top view of the Raman setup around the glass cell	26
3.5	Side view of the Raman setup around the glass cell	27
3.6	Electronic circuits for the offset lock of the Raman laser to the D1 laser.	27
3.7	Resulting error signal of the offset lock setup	28
3.8	Setup of the crossed dipole trap	30
3.9	Setup of the accordion lattice	31
3.10	Telescopes behind the fibers for the beams of the triangular lattice . . .	33
3.11	Optomechanics for the adjustment of the objective and the integration of the MOT beam through the objective	35
4.1	Draft for the simulation and production of the MOT coils and Fesh- bach coils	46
4.2	Draft for the simulation and production of the Tilt coil	47
4.3	MOT coils, Feshbach coils and Tilt coil in their final position at the experiment	48
4.4	Simulated magnetic field of 810 G created by running the Feshbach coils in Helmholtz configuration	51
4.5	Combining Feshbach coils and MOT coils in different configurations . .	52
4.6	Resulting magnetic field of the combination of the Feshbach coils in Helmholtz configuration and the Tilt coil	54
4.7	Combining the Tilt coil with a gradient field of 50 G/cm along the hor- izontal x-direction created by the MOT coils in anti-Helmholtz confi- guration	55
4.8	Circuit for switching the current through the Feshbach coils and the Tilt coil	58
4.9	Circuit for switching the current through the MOT coils	60

4.10	Switch-on behavior of the Feshbach coils when a current of 80 A is ramped up	61
5.1	Timeline of the MOT and the compressed MOT phase	66
5.2	Timeline of the gray molasses phase	69
5.3	Timeline of the evaporative cooling phase in the optical dipole trap for the creation of a molecular BEC	70
5.4	Onset of Bose-Einstein condensation of the molecular ${}^6\text{Li}$ dimers . . .	71
5.5	Time-of-Flight series of a molecular BEC	72
5.6	Timeline of the evaporative cooling phase in the optical dipole trap for the creation of a degenerate Fermi gas	73
6.1	Absorption images of the accordion lattice with various intersection angles and hence lattice spacings taken with three different imaging setups	76
6.2	Realizable lattice spacings of the optical accordion	78
6.3	Kapitza-Dirac scattering of the atoms by the transient triangular optical lattice	82
6.4	Analysis of the positions of the Kapitza-Dirac peaks for the determination of the lattice structure	83
6.5	Timeline of the experimental steps to load the atoms into a deep three-dimensional optical lattice	88
7.1	Raman carrier resonance of the two-photon transition between the Hyperfine ground states of ${}^6\text{Li}$ in the optical dipole trap	93
7.2	Raman carrier resonance of the two-photon transition between the hyperfine ground states of ${}^6\text{Li}$ in the 3D optical lattice	94
7.3	Rabi oscillations for two different laser powers in the Raman beams . .	95
7.4	Absorption image of a molecular BEC taken with the EMCCD camera in the imaging setup with a magnification of $M \approx -40$	97
8.1	Proposal for the simulation of non-sequential double ionization with ultracold atoms	101
8.2	Two possibilities to create an artificial benzene molecule for the simulation of molecular orbitals and dynamics	102
A.1	Level diagram of the ground state and the $2P$ excited state of ${}^6\text{Li}$	105
B.1	Magnetic field dependence of the $2^2S_{1/2}$ ground state of ${}^6\text{Li}$	107
B.2	Magnetic field dependence of the $2^2P_{1/2}$ excited state of ${}^6\text{Li}$	108
B.3	Magnetic field dependence of the $2^2P_{3/2}$ excited state of ${}^6\text{Li}$	109
C.1	Broad Feshbach resonances between the three lowest Paschen-Back states of ${}^6\text{Li}$	111

List of Tables

3.1	Anti-reflective coating of the science cell	21
4.1	Mechanical and electrical properties of the two coil pairs and the single coil	49
4.2	Magnetic fields of the MOT coils and the Feshbach coils	50
4.3	Magnetic field of the Tilt coil	53
4.4	Magnetic field of all offset coil pairs	56
D.1	All values derived from the analysis of the Kapitza-Dirac peaks	113

Bibliography

- [1] Richard P. Feynman. “Simulating physics with computers”. In: *International Journal of Theoretical Physics* 21.6-7 (1982), pp. 467–488. DOI: 10.1007/bf02650179 (cit. on p. 1).
- [2] Michael A. Nielsen and Isaac L. Chuang. *Quantum Computation and Quantum Information: 10th Anniversary Edition*. Cambridge University Press, 2011. ISBN: 9781107002173 (cit. on p. 1).
- [3] T. D. Ladd et al. “Quantum computers”. In: *Nature* 464.7285 (2010), pp. 45–53 (cit. on p. 1).
- [4] M. H. Anderson et al. “Observation of Bose-Einstein Condensation in a Dilute Atomic Vapor”. In: *Science* 269.5221 (1995), pp. 198–201. DOI: 10.1126/science.269.5221.198 (cit. on p. 1).
- [5] K. B. Davis et al. “Bose-Einstein Condensation in a Gas of Sodium Atoms”. In: *Physical Review Letters* 75.22 (1995), pp. 3969–3973. DOI: 10.1103/physrevlett.75.3969 (cit. on p. 1).
- [6] C. C. Bradley et al. “Evidence of Bose-Einstein Condensation in an Atomic Gas with Attractive Interactions”. In: *Physical Review Letters* 75.9 (1995), pp. 1687–1690. DOI: 10.1103/physrevlett.75.1687 (cit. on p. 1).
- [7] Maciej Lewenstein et al. “Ultracold atomic gases in optical lattices: mimicking condensed matter physics and beyond”. In: *Advances in Physics* 56.2 (2007), pp. 243–379. DOI: 10.1080/00018730701223200 (cit. on p. 1).
- [8] Immanuel Bloch, Jean Dalibard, and Wilhelm Zwerger. “Many-body physics with ultracold gases”. In: *Reviews of Modern Physics* 80.3 (2008), pp. 885–964. DOI: 10.1103/revmodphys.80.885 (cit. on p. 1).
- [9] Immanuel Bloch, Jean Dalibard, and Sylvain Nascimbène. “Quantum simulations with ultracold quantum gases”. In: *Nature Physics* 8.4 (2012), pp. 267–276. DOI: 10.1038/nphys2259 (cit. on p. 1).
- [10] Päivi Törmä and Klaus Sengstock. *Quantum Gas Experiments*. Imperial College Press, 2014. DOI: 10.1142/p945 (cit. on p. 1).
- [11] Christian Gross and Immanuel Bloch. “Quantum simulations with ultracold atoms in optical lattices”. In: *Science* 357.6355 (2017), pp. 995–1001. DOI: 10.1126/science.aal3837 (cit. on p. 1).

- [12] W. Ketterle, D. S. Durfee, and D. M. Stamper-Kurn. "Making, probing and understanding Bose-Einstein condensates". In: *Proc. of the International School of Physics 'Enrico Fermi'* 140 (1999), pp. 67–176. DOI: 10.3254/978-1-61499-225-7-67 (cit. on p. 1).
- [13] W. Ketterle and M. W. Zwierlein. "Making, probing and understanding ultracold fermi gases". In: *Proc. of the International School of Physics 'Enrico Fermi'* CLXIV (2008). DOI: 10.1393/ncr/i2008-10033-1 (cit. on pp. 1, 6, 71, 74).
- [14] Rudolf Grimm, Matthias Weidemüller, and Yurii B. Ovchinnikov. "Optical Dipole Traps for Neutral Atoms". In: ed. by Benjamin Bederson and Herbert Walther. Vol. 42. *Advances In Atomic, Molecular, and Optical Physics*. Academic Press, 2000, pp. 95 –170. DOI: [https://doi.org/10.1016/S1049-250X\(08\)60186-X](https://doi.org/10.1016/S1049-250X(08)60186-X) (cit. on p. 1).
- [15] Cheng Chin et al. "Feshbach resonances in ultracold gases". In: *Rev. Mod. Phys.* 82 (2 2010), pp. 1225–1286. DOI: 10.1103/RevModPhys.82.1225 (cit. on pp. 1, 6, 42).
- [16] Waseem S. Bakr et al. "A quantum gas microscope for detecting single atoms in a Hubbard-regime optical lattice". In: *Nature* 462.7269 (2009), 74–77. ISSN: 1476-4687. DOI: 10.1038/nature08482 (cit. on pp. 1, 7–9, 14).
- [17] Jacob F. Sherson et al. "Single-atom-resolved fluorescence imaging of an atomic Mott insulator". In: *Nature* 467.7311 (2010), 68–72. ISSN: 1476-4687. DOI: 10.1038/nature09378 (cit. on pp. 1, 7, 9, 14).
- [18] Andreas Kerkmann. "A novel Apparatus for Quantum Gas Microscopy of Lithium Atoms". PhD thesis. Universität Hamburg, 2019 (cit. on pp. 3, 10, 12, 17–19, 22, 23, 25, 30–35, 37, 45, 48, 56, 67, 69, 71, 72, 76–78, 97, 102, 107–109, 111).
- [19] G. Audi et al. "The Nubase evaluation of nuclear and decay properties". In: *Nuclear Physics A* 729.1 (2003). The 2003 NUBASE and Atomic Mass Evaluations, pp. 3 –128. ISSN: 0375-9474. DOI: <https://doi.org/10.1016/j.nuclphysa.2003.11.001> (cit. on p. 5).
- [20] Michael Eric Gehm. "Preparation of an optically-trapped degenerate Fermi gas of ${}^6\text{Li}$: Finding the route to degeneracy". PhD thesis. Duke University, 2003 (cit. on pp. 6, 107–109).
- [21] Timon Alexander Hilker. "Spin-Resolved Microscopy of Strongly Correlated Fermionic Many-Body States". PhD thesis. Ludwig-Maximilians-Universität München, 2017 (cit. on pp. 6, 15, 16).
- [22] Martin Miranda et al. "Site-resolved imaging of ytterbium atoms in a two-dimensional optical lattice". In: *Phys. Rev. A* 91 (6 2015), p. 063414. DOI: 10.1103/PhysRevA.91.063414 (cit. on pp. 7, 14).

- [23] Ryuta Yamamoto et al. "An ytterbium quantum gas microscope with narrow-line laser cooling". In: *New Journal of Physics* 18.2 (2016), p. 023016. DOI: 10.1088/1367-2630/18/2/023016 (cit. on p. 7).
- [24] Elmar Haller et al. "Single-atom imaging of fermions in a quantum-gas microscope". In: *Nature Physics* 11.9 (2015), 738–742. ISSN: 1745-2481. DOI: 10.1038/nphys3403 (cit. on pp. 7, 14).
- [25] Lawrence W. Cheuk et al. "Quantum-Gas Microscope for Fermionic Atoms". In: *Phys. Rev. Lett.* 114 (19 2015), p. 193001. DOI: 10.1103/PhysRevLett.114.193001 (cit. on pp. 7, 8, 14).
- [26] G. J. A. Edge et al. "Imaging and addressing of individual fermionic atoms in an optical lattice". In: *Phys. Rev. A* 92 (6 2015), p. 063406. DOI: 10.1103/PhysRevA.92.063406 (cit. on pp. 7, 14).
- [27] Maxwell F. Parsons et al. "Site-Resolved Imaging of Fermionic ${}^6\text{Li}$ in an Optical Lattice". In: *Phys. Rev. Lett.* 114 (21 2015), p. 213002. DOI: 10.1103/PhysRevLett.114.213002 (cit. on pp. 7–9, 14–16).
- [28] Ahmed Omran et al. "Microscopic Observation of Pauli Blocking in Degenerate Fermionic Lattice Gases". In: *Phys. Rev. Lett.* 115 (26 2015), p. 263001. DOI: 10.1103/PhysRevLett.115.263001 (cit. on pp. 7, 9, 14–16).
- [29] Peter T. Brown et al. "Spin-imbalance in a 2D Fermi-Hubbard system". In: *Science* 357.6358 (2017), pp. 1385–1388. ISSN: 0036-8075. DOI: 10.1126/science.aam7838. eprint: <https://science.sciencemag.org/content/357/6358/1385.full.pdf> (cit. on pp. 7, 9, 13–16).
- [30] W. S. Bakr et al. "Probing the Superfluid-to-Mott Insulator Transition at the Single-Atom Level". In: *Science* 329.5991 (2010), 547–550. ISSN: 1095-9203. DOI: 10.1126/science.1192368 (cit. on pp. 7, 9).
- [31] Martin Miranda et al. "Site-resolved imaging of a bosonic Mott insulator using ytterbium atoms". In: *Phys. Rev. A* 96 (4 2017), p. 043626. DOI: 10.1103/PhysRevA.96.043626 (cit. on pp. 7, 14).
- [32] Daniel Greif et al. "Site-resolved imaging of a fermionic Mott insulator". In: *Science* 351.6276 (2016), pp. 953–957. ISSN: 0036-8075. DOI: 10.1126/science.aad9041. eprint: <https://science.sciencemag.org/content/351/6276/953.full.pdf> (cit. on pp. 7, 9).
- [33] Lawrence W. Cheuk et al. "Observation of 2D Fermionic Mott Insulators of ${}^{40}\text{K}$ with Single-Site Resolution". In: *Phys. Rev. Lett.* 116 (23 2016), p. 235301. DOI: 10.1103/PhysRevLett.116.235301 (cit. on pp. 7, 9).
- [34] Christof Weitenberg et al. "Single-spin addressing in an atomic Mott insulator". In: *Nature* 471.7338 (2011), 319–324. ISSN: 1476-4687. DOI: 10.1038/nature09827 (cit. on p. 7).

- [35] M. Endres et al. "Observation of Correlated Particle-Hole Pairs and String Order in Low-Dimensional Mott Insulators". In: *Science* 334.6053 (2011), pp. 200–203. ISSN: 0036-8075. DOI: 10.1126/science.1209284. eprint: <https://science.sciencemag.org/content/334/6053/200.full.pdf> (cit. on p. 7).
- [36] M. Endres et al. "Single-site- and single-atom-resolved measurement of correlation functions". In: *Applied Physics B* 113.1 (2013), 27–39. ISSN: 1432-0649. DOI: 10.1007/s00340-013-5552-9 (cit. on p. 7).
- [37] Jonathan Simon et al. "Quantum simulation of antiferromagnetic spin chains in an optical lattice". In: *Nature* 472.7343 (2011), 307–312. ISSN: 1476-4687. DOI: 10.1038/nature09994 (cit. on p. 7).
- [38] Maxwell F. Parsons et al. "Site-resolved measurement of the spin-correlation function in the Fermi-Hubbard model". In: *Science* 353.6305 (2016), pp. 1253–1256. DOI: 10.1126/science.aag1430. eprint: <https://science.sciencemag.org/content/353/6305/1253.full.pdf> (cit. on p. 7).
- [39] Anton Mazurenko et al. "A cold-atom Fermi-Hubbard antiferromagnet". In: *Nature* 545.7655 (2017), pp. 462–466. DOI: 10.1038/nature22362 (cit. on pp. 7, 101).
- [40] Christie S. Chiu et al. "Quantum State Engineering of a Hubbard System with Ultracold Fermions". In: *Phys. Rev. Lett.* 120 (24 2018), p. 243201. DOI: 10.1103/PhysRevLett.120.243201 (cit. on pp. 7, 101).
- [41] Christie S. Chiu et al. "String patterns in the doped Hubbard model". In: *Science* 365.6450 (2019), pp. 251–256. ISSN: 0036-8075. DOI: 10.1126/science.aav3587. eprint: <https://science.sciencemag.org/content/365/6450/251.full.pdf> (cit. on p. 7).
- [42] Geoffrey Ji et al. *Dynamical interplay between a single hole and a Hubbard antiferromagnet*. 2020. arXiv: 2006.06672 [cond-mat.quant-gas] (cit. on p. 7).
- [43] Martin Boll et al. "Spin- and density-resolved microscopy of antiferromagnetic correlations in Fermi-Hubbard chains". In: *Science* 353.6305 (2016), pp. 1257–1260. DOI: 10.1126/science.aag1635. eprint: <https://science.sciencemag.org/content/353/6305/1257.full.pdf> (cit. on pp. 7, 9).
- [44] Timon A. Hilker et al. "Revealing hidden antiferromagnetic correlations in doped Hubbard chains via string correlators". In: *Science* 357.6350 (2017), pp. 484–487. ISSN: 0036-8075. DOI: 10.1126/science.aam8990. eprint: <https://science.sciencemag.org/content/357/6350/484.full.pdf> (cit. on p. 7).
- [45] Guillaume Salomon et al. "Direct observation of incommensurate magnetism in Hubbard chains". In: *Nature* 565.7737 (2018), 56–60. ISSN: 1476-4687. DOI: 10.1038/s41586-018-0778-7 (cit. on p. 7).
- [46] Joannis Koepsell et al. "Imaging magnetic polarons in the doped Fermi-Hubbard model". In: *Nature* 572.7769 (2019), 358–362. ISSN: 1476-4687. DOI: 10.1038/s41586-019-1463-1 (cit. on p. 7).

- [47] Jayadev Vijayan et al. “Time-resolved observation of spin-charge deconfinement in fermionic Hubbard chains”. In: *Science* 367.6474 (2020), pp. 186–189. ISSN: 0036-8075. DOI: 10.1126/science.aay2354. eprint: <https://science.sciencemag.org/content/367/6474/186.full.pdf> (cit. on p. 7).
- [48] Joannis Koepsell et al. *Microscopic evolution of doped Mott insulators from polaronic metal to Fermi liquid*. 2020. arXiv: 2009.04440 [cond-mat.quant-gas] (cit. on p. 7).
- [49] Elmer Guardado-Sanchez et al. “Probing the Quench Dynamics of Antiferromagnetic Correlations in a 2D Quantum Ising Spin System”. In: *Phys. Rev. X* 8 (2 2018), p. 021069. DOI: 10.1103/PhysRevX.8.021069 (cit. on p. 7).
- [50] Lawrence W. Cheuk et al. “Observation of spatial charge and spin correlations in the 2D Fermi-Hubbard model”. In: *Science* 353.6305 (2016), pp. 1260–1264. DOI: 10.1126/science.aag3349. eprint: <https://science.sciencemag.org/content/353/6305/1260.full.pdf> (cit. on p. 7).
- [51] Matthew A. Nichols et al. “Spin transport in a Mott insulator of ultracold fermions”. In: *Science* 363.6425 (2019), pp. 383–387. ISSN: 0036-8075. DOI: 10.1126/science.aat4387. eprint: <https://science.sciencemag.org/content/363/6425/383.full.pdf> (cit. on p. 7).
- [52] Andrea Bergschneider et al. “Spin-resolved single-atom imaging of ${}^6\text{Li}$ in free space”. In: *Phys. Rev. A* 97 (6 2018), p. 063613. DOI: 10.1103/PhysRevA.97.063613 (cit. on p. 7).
- [53] S. Blatt et al. “Low-noise optical lattices for ultracold ${}^6\text{Li}$ ”. In: *Phys. Rev. A* 92 (2 2015), p. 021402. DOI: 10.1103/PhysRevA.92.021402 (cit. on p. 9).
- [54] A. Mazurenko et al. “Implementation of a stable, high-power optical lattice for quantum gas microscopy”. In: *Review of Scientific Instruments* 90.3 (2019), p. 033101. DOI: 10.1063/1.5066623. eprint: <https://doi.org/10.1063/1.5066623> (cit. on p. 9).
- [55] Christof Weitenberg. “Single-Atom Resolved Imaging and Manipulation in an Atomic Mott Insulator”. PhD thesis. Ludwig-Maximilians-Universität München, 2011 (cit. on pp. 9, 79).
- [56] Karl D. Nelson, Xiao Li, and David S. Weiss. “Imaging single atoms in a three-dimensional array”. In: *Nature Physics* 3.8 (2007), 556–560. ISSN: 1745-2481. DOI: 10.1038/nphys645 (cit. on pp. 9, 79).
- [57] Joannis Koepsell et al. “Robust Bilayer Charge Pumping for Spin- and Density-Resolved Quantum Gas Microscopy”. In: *Phys. Rev. Lett.* 125 (1 2020), p. 010403. DOI: 10.1103/PhysRevLett.125.010403 (cit. on p. 9).
- [58] Thomas Hartke et al. *Measuring total density correlations in a Fermi-Hubbard gas via bilayer microscopy*. 2020. arXiv: 2003.11669 [cond-mat.quant-gas] (cit. on p. 9).

- [59] Ottó Eliasson et al. *Spatial tomography of individual atoms in a quantum gas microscope*. 2019. arXiv: 1912.03079 [cond-mat.quant-gas] (cit. on p. 9).
- [60] J. L. Ville et al. “Loading and compression of a single two-dimensional Bose gas in an optical accordion”. In: *Phys. Rev. A* 95 (1 2017), p. 013632. DOI: 10.1103/PhysRevA.95.013632 (cit. on pp. 9, 11, 31).
- [61] Ryuta Yamamoto et al. *Single-site-resolved imaging of ultracold atoms in a triangular optical lattice*. 2020. arXiv: 2010.05200 [cond-mat.quant-gas] (cit. on pp. 9, 11).
- [62] Maxim Pyzh et al. “Quantum point spread function for imaging trapped few-body systems with a quantum gas microscope”. In: *New Journal of Physics* 21.5 (2019), p. 053013. ISSN: 1367-2630. DOI: 10.1088/1367-2630/ab1ae7 (cit. on pp. 9, 103).
- [63] F. Serwane et al. “Deterministic Preparation of a Tunable Few-Fermion System”. In: *Science* 332.6027 (2011), pp. 336–338. ISSN: 0036-8075. DOI: 10.1126/science.1201351. eprint: <https://science.sciencemag.org/content/332/6027/336.full.pdf> (cit. on pp. 10, 50, 54, 100, 101).
- [64] Luca Bayha et al. *Observing the emergence of a quantum phase transition – shell by shell*. 2020. arXiv: 2004.14761 [cond-mat.quant-gas] (cit. on pp. 10, 100, 101).
- [65] Maxwell Fredrick Parsons. “Probing the Hubbard model with single-site resolution”. PhD thesis. Harvard University, 2016 (cit. on p. 10).
- [66] Martin Boll. “Spin and Density Resolved Microscopy of Hubbard Chains”. PhD thesis. Ludwig-Maximilians-Universität München, 2016 (cit. on p. 10).
- [67] Eleonora Lippi. “Realization of a large-spacing optical lattice for trapping fermionic lithium gases in two dimensions”. Master’s thesis. Università degli Studi di Firenze, 2017 (cit. on p. 11).
- [68] Debayan Mitra. “Exploring attractively interacting fermions in 2D using a quantum gas microscope”. PhD thesis. Princeton University, 2018 (cit. on pp. 11, 15, 74, 96).
- [69] J. Struck et al. “Quantum Simulation of Frustrated Classical Magnetism in Triangular Optical Lattices”. In: *Science* 333.6045 (2011), pp. 996–999. ISSN: 0036-8075. DOI: 10.1126/science.1207239. eprint: <https://science.sciencemag.org/content/333/6045/996.full.pdf> (cit. on p. 11).
- [70] J. Struck et al. “Engineering Ising-XY spin-models in a triangular lattice using tunable artificial gauge fields”. In: *Nature Physics* 9.11 (2013), 738–743. ISSN: 1745-2481. DOI: 10.1038/nphys2750 (cit. on p. 11).

- [71] Daniel Greif et al. “Short-Range Quantum Magnetism of Ultracold Fermions in an Optical Lattice”. In: *Science* 340.6138 (2013), pp. 1307–1310. ISSN: 0036-8075. DOI: 10.1126/science.1236362. eprint: <https://science.sciencemag.org/content/340/6138/1307.full.pdf> (cit. on p. 11).
- [72] P. Soltan-Panahi et al. “Multi-component quantum gases in spin-dependent hexagonal lattices”. In: *Nature Physics* 7.5 (2011), 434–440. ISSN: 1745-2481. DOI: 10.1038/nphys1916 (cit. on p. 11).
- [73] M Weinberg et al. “Breaking inversion symmetry in a state-dependent honeycomb lattice: artificial graphene with tunable band gap”. In: *2D Materials* 3.2 (2016), p. 024005. ISSN: 2053-1583. DOI: 10.1088/2053-1583/3/2/024005 (cit. on p. 11).
- [74] Gregor Jotzu et al. “Experimental realization of the topological Haldane model with ultracold fermions”. In: *Nature* 515.7526 (2014), 237–240. ISSN: 1476-4687. DOI: 10.1038/nature13915 (cit. on p. 11).
- [75] N. Fläschner et al. “Experimental reconstruction of the Berry curvature in a Floquet Bloch band”. In: *Science* 352.6289 (2016), pp. 1091–1094. ISSN: 0036-8075. DOI: 10.1126/science.aad4568. eprint: <https://science.sciencemag.org/content/352/6289/1091.full.pdf> (cit. on p. 11).
- [76] C Becker et al. “Ultracold quantum gases in triangular optical lattices”. In: 12.6 (2010), p. 065025. DOI: 10.1088/1367-2630/12/6/065025 (cit. on p. 12).
- [77] Julian Struck. “Artificial Gauge Fields in Driven Optical Lattices - From Frustrated XY Models to Ising Ferromagnetism”. PhD thesis. Universität Hamburg, 2013 (cit. on p. 12).
- [78] Nick Fläschner. “Ultracold Fermions in Tunable Hexagonal Lattices: From High-Precision Spectroscopy to the Measurement of Berry Curvature”. PhD thesis. Universität Hamburg, 2016 (cit. on p. 12).
- [79] Rio Fernandes, D. et al. “Sub-Doppler laser cooling of fermionic 40K atoms in three-dimensional gray optical molasses”. In: *EPL* 100.6 (2012), p. 63001. DOI: 10.1209/0295-5075/100/63001 (cit. on p. 14).
- [80] Andrew T. Grier et al. “ Λ -enhanced sub-Doppler cooling of lithium atoms in D_1 gray molasses”. In: *Phys. Rev. A* 87 (6 2013), p. 063411. DOI: 10.1103/PhysRevA.87.063411 (cit. on pp. 14, 68).
- [81] Dipankar Nath et al. “Quantum-interference-enhanced deep sub-Doppler cooling of ^{39}K atoms in gray molasses”. In: *Phys. Rev. A* 88 (5 2013), p. 053407. DOI: 10.1103/PhysRevA.88.053407 (cit. on p. 14).
- [82] G. Salomon et al. “Gray-molasses cooling of 39K to a high phase-space density”. In: *EPL (Europhysics Letters)* 104.6 (2013), p. 63002. DOI: 10.1209/0295-5075/104/63002 (cit. on p. 14).

- [83] A. Burchianti et al. "Efficient all-optical production of large ${}^6\text{Li}$ quantum gases using D_1 gray-molasses cooling". In: *Phys. Rev. A* 90 (4 2014), p. 043408. DOI: 10.1103/PhysRevA.90.043408 (cit. on pp. 14, 29, 67, 74).
- [84] Franz Sievers et al. "Simultaneous sub-Doppler laser cooling of fermionic ${}^6\text{Li}$ and ${}^{40}\text{K}$ on the D_1 line: Theory and experiment". In: *Phys. Rev. A* 91 (2 2015), p. 023426. DOI: 10.1103/PhysRevA.91.023426 (cit. on p. 14).
- [85] Giacomo Colzi et al. "Sub-Doppler cooling of sodium atoms in gray molasses". In: *Phys. Rev. A* 93 (2 2016), p. 023421. DOI: 10.1103/PhysRevA.93.023421 (cit. on p. 14).
- [86] Hao-Ze Chen et al. "Production of large ${}^{41}\text{K}$ Bose-Einstein condensates using D_1 gray molasses". In: *Phys. Rev. A* 94 (3 2016), p. 033408. DOI: 10.1103/PhysRevA.94.033408 (cit. on p. 14).
- [87] G D Bruce et al. "Sub-Doppler laser cooling of 40K with Raman gray molasses on the D_2 line". In: *Journal of Physics B: Atomic, Molecular and Optical Physics* 50.9 (2017), p. 095002. DOI: 10.1088/1361-6455/aa65ea (cit. on p. 14).
- [88] Sara Rosi et al. " Λ -enhanced grey molasses on the D_2 transition of Rubidium-87 atoms". In: *Scientific Reports* 8.1 (2018). ISSN: 2045-2322. DOI: 10.1038/s41598-018-19814-z (cit. on p. 14).
- [89] Ya-Fen Hsiao, Yu-Ju Lin, and Ying-Cheng Chen. " Λ -enhanced gray-molasses cooling of cesium atoms on the D_2 line". In: *Phys. Rev. A* 98 (3 2018), p. 033419. DOI: 10.1103/PhysRevA.98.033419 (cit. on p. 14).
- [90] Zhenlian Shi et al. "Sub-Doppler Laser Cooling of ${}^{23}\text{Na}$ in Gray Molasses on the D_2 Line". In: *Chinese Physics Letters* 35.12 (2018), p. 123701. DOI: 10.1088/0256-307x/35/12/123701 (cit. on p. 14).
- [91] L. Gabardos et al. "Cooling all external degrees of freedom of optically trapped chromium atoms using gray molasses". In: *Phys. Rev. A* 99 (2 2019), p. 023607. DOI: 10.1103/PhysRevA.99.023607 (cit. on p. 14).
- [92] E. Neri et al. "Realization of a cold mixture of fermionic chromium and lithium atoms". In: *Phys. Rev. A* 101 (6 2020), p. 063602. DOI: 10.1103/PhysRevA.101.063602 (cit. on p. 14).
- [93] D. Leibfried et al. "Quantum dynamics of single trapped ions". In: *Rev. Mod. Phys.* 75 (1 2003), pp. 281–324. DOI: 10.1103/RevModPhys.75.281 (cit. on p. 14).
- [94] A. M. Kaufman, B. J. Lester, and C. A. Regal. "Cooling a Single Atom in an Optical Tweezer to Its Quantum Ground State". In: *Phys. Rev. X* 2 (4 2012), p. 041014. DOI: 10.1103/PhysRevX.2.041014 (cit. on p. 16).
- [95] Peter Thomas Brown. "Probing dynamical quantities in the 2D Fermi-Hubbard model with quantum gas microscopy". PhD thesis. Princeton University, 2019 (cit. on p. 16).

- [96] Mathis Fischer. "An Optical Dipole Trap and an Accordion Lattice for a Quantum Gas Microscope". Master's thesis. Universität Hamburg, 2018 (cit. on pp. 17, 29–32, 37, 49, 71, 75, 76).
- [97] Michael Hagemann. "Magnetfeldspulen und ein Interferometer für ein Quantengasmikroskop mit Lithiumatomen". Master's thesis. Universität Hamburg, 2016 (cit. on pp. 17, 21, 39).
- [98] Andreas Kerkmann. "Ein Lasersystem zum Fangen und Kühlen von bosonischem und fermionischem Lithium". Master's thesis. Universität Hamburg, 2015 (cit. on pp. 17, 20–22, 57).
- [99] T. G. Tiecke et al. "High-flux two-dimensional magneto-optical-trap source for cold lithium atoms". In: *Phys. Rev. A* 80 (1 2009), p. 013409. DOI: 10.1103/PhysRevA.80.013409 (cit. on p. 17).
- [100] Claudiu Andrei Stan. "Experiments with Interacting Bose and Fermi Gases". PhD thesis. Massachusetts Institute of Technology, 2005 (cit. on p. 18).
- [101] Silke Ospelkaus. "Quantum Degenerate Fermi-Bose Mixtures of ^{40}K and ^{87}Rb in 3D Optical Lattices". PhD thesis. Universität Hamburg, 2006 (cit. on p. 19).
- [102] G. Lamporesi et al. "Compact high-flux source of cold sodium atoms". In: *Review of Scientific Instruments* 84.6 (2013), p. 063102. DOI: 10.1063/1.4808375. eprint: <https://doi.org/10.1063/1.4808375> (cit. on p. 20).
- [103] Florian Huber. "Site-Resolved Imaging with the Fermi Gas Microscope". PhD thesis. Harvard University, 2014 (cit. on pp. 25, 27, 96).
- [104] Alexander Franzen. "ComponentLibrary". In: gwoptics.org (cit. on p. 25).
- [105] U. Schünemann et al. "Simple scheme for tunable frequency offset locking of two lasers". In: *Review of Scientific Instruments* 70.1 (1999), pp. 242–243. DOI: 10.1063/1.1149573. eprint: <https://doi.org/10.1063/1.1149573> (cit. on p. 27).
- [106] Jonathan Schwardt. "Untersuchung von Resonatoren für die Stabilisierung von Laserstrahlquellen". Bachelor's thesis. Universität Hamburg, 2019 (cit. on pp. 28, 29).
- [107] Kyungtae Kim et al. "Rapid production of large ^7Li Bose-Einstein condensates using D_1 gray molasses". In: *Phys. Rev. A* 99 (5 2019), p. 053604. DOI: 10.1103/PhysRevA.99.053604 (cit. on pp. 29, 51, 54).
- [108] Yann Hendrick Kiefer. "Aufbau und Planung einer Intensitätskontrolle für eine Dipolfalle zur evaporativen Kühlung von Lithiumatomen". Bachelor's thesis. Universität Hamburg, 2016 (cit. on p. 30).
- [109] Hauke Schmidt. "Dynamische Kontrolle der Geometrie optischer Gitter". Bachelor's thesis. Universität Hamburg, 2015 (cit. on p. 30).

- [110] Jan Mika Jacobsen. “A Reconstruction Algorithm for Fluorescence Images of Lithium Atoms in a Triangular Optical Lattice”. Master’s thesis. Universität Hamburg, 2017 (cit. on pp. 36, 100).
- [111] Tobias Petersen. “Charakterisierung eines hochauflösenden Abbildungssystems”. Bachelor’s thesis. Universität Hamburg, 2018 (cit. on pp. 37, 100).
- [112] J. Pérez-Ríos and A. S. Sanz. “How does a magnetic trap work?” In: *American Journal of Physics* 81.11 (2013), pp. 836–843. DOI: 10.1119/1.4819167. eprint: <https://doi.org/10.1119/1.4819167> (cit. on p. 40).
- [113] Ralf Dinter. “Aufbau und Charakterisierung einer Magnetfalle zur simultanen Speicherung von ^{40}K und ^{87}Rb ”. Diploma’s thesis. Universität Hamburg, 2004 (cit. on p. 40).
- [114] Tilman Esslinger, Immanuel Bloch, and Theodor W. Hänsch. “Bose-Einstein condensation in a quadrupole-Ioffe-configuration trap”. In: *Phys. Rev. A* 58 (4 1998), R2664–R2667. DOI: 10.1103/PhysRevA.58.R2664 (cit. on pp. 41, 55).
- [115] Widagdo Setiawan. “Fermi Gas Microscope”. PhD thesis. Harvard University, 2012 (cit. on p. 41).
- [116] Kai Morgener. “Microscopy of 2D Fermi Gases: Exploring Excitations and Thermodynamics”. PhD thesis. Universität Hamburg, 2014 (cit. on p. 41).
- [117] Eric Wille. “Preparation of an Optically Trapped Fermi-Fermi Mixture of ^6Li and ^{40}K Atoms and Characterization of the Interspecies Interactions by Feshbach Spectroscopy”. PhD thesis. Universität Innsbruck, 2014 (cit. on p. 41).
- [118] Timo Ottenstein. “Few-body physics in ultracold Fermi gases”. PhD thesis. Ruperto-Carola University of Heidelberg, 2010 (cit. on p. 41).
- [119] Florian Schreck. “Mixtures of Ultracold Gases: Fermi Sea and Bose-Einstein Condensate of Lithium Isotopes”. PhD thesis. Université Paris VI, 2002 (cit. on p. 41).
- [120] Chen-Lung Hung et al. “Accelerating evaporative cooling of atoms into Bose-Einstein condensation in optical traps”. In: *Phys. Rev. A* 78 (1 2008), p. 011604. DOI: 10.1103/PhysRevA.78.011604 (cit. on p. 51).
- [121] D. M. Brink and C. V. Sukumar. “Majorana spin-flip transitions in a magnetic trap”. In: *Phys. Rev. A* 74 (3 2006), p. 035401. DOI: 10.1103/PhysRevA.74.035401 (cit. on p. 55).
- [122] Malte Hagemann. “Aufbau und Charakterisierung einer Lithium-MOT”. Bachelor’s thesis. Universität Hamburg, 2017 (cit. on p. 56).
- [123] M. S. Safronova, U. I. Safronova, and Charles W. Clark. “Magic wavelengths for optical cooling and trapping of lithium”. In: *Phys. Rev. A* 86 (4 2012), p. 042505. DOI: 10.1103/PhysRevA.86.042505 (cit. on p. 67).

- [124] G. E. Astrakharchik et al. “Momentum Distribution and Condensate Fraction of a Fermion Gas in the BCS-BEC Crossover”. In: *Phys. Rev. Lett.* 95 (23 2005), p. 230405. DOI: 10.1103/PhysRevLett.95.230405 (cit. on p. 71).
- [125] Shu-Jin Deng et al. “All-Optical Production of Quantum Degeneracy and Molecular Bose–Einstein Condensation of ^6Li ”. In: *Chinese Physics Letters* 32.5, 053401 (2015), p. 053401. DOI: 10.1088/0256-307X/32/5/053401 (cit. on p. 71).
- [126] Bryce Gadway et al. “Analysis of Kapitza-Dirac diffraction patterns beyond the Raman-Nath regime”. In: *Opt. Express* 17.21 (2009), pp. 19173–19180. DOI: 10.1364/OE.17.019173 (cit. on p. 81).
- [127] Gunnar Ritt. “Fourier-Synthese von asymmetrischen optischen Potentialen für Atome”. PhD thesis. Eberhard Karls Universität zu Tübingen, 2007 (cit. on p. 81).
- [128] Christoph Ölschläger. “Quantensimulation von frustriertem Magnetismus in einem optischen Dreiecksgitter”. Diploma’s thesis. Universität Hamburg, 2011 (cit. on p. 82).
- [129] Ralf Labouvie. “Parametrisches Heizen in optischen Gittern und Charakterisierung eines akusto-optischen Deflektors für die Erzeugung von zeitgemittelten Potentialen”. Diploma’s thesis. Johannes Gutenberg-Universität Mainz, 2010 (cit. on p. 86).
- [130] Sun Kyung Lee and Hai-Woong Lee. “Damped population oscillation in a spontaneously decaying two-level atom coupled to a monochromatic field”. In: *Phys. Rev. A* 74 (6 2006), p. 063817. DOI: 10.1103/PhysRevA.74.063817 (cit. on p. 95).
- [131] Ahmed Omran. “A Microscope for Fermi Gases”. PhD thesis. Ludwig-Maximilians-Universität München, 2016 (cit. on p. 96).
- [132] Chen-Lung Hung et al. “Extracting density–density correlations from in situ images of atomic quantum gases”. In: *New Journal of Physics* 13.7 (2011), p. 075019. DOI: 10.1088/1367-2630/13/7/075019 (cit. on p. 98).
- [133] Bastian Lunow. “Applications of Neural Networks in Quantum Gas Experiments”. Master’s thesis. Universität Hamburg, 2020 (cit. on p. 100).
- [134] Lewis R B Picard et al. “Deep learning-assisted classification of site-resolved quantum gas microscope images”. In: *Measurement Science and Technology* 31.2 (2019), p. 025201. ISSN: 1361-6501. DOI: 10.1088/1361-6501/ab44d8 (cit. on p. 100).
- [135] Benno S. Rem et al. “Identifying quantum phase transitions using artificial neural networks on experimental data”. In: *Nature Physics* 15.9 (2019), 917–920. ISSN: 1745-2481. DOI: 10.1038/s41567-019-0554-0 (cit. on p. 100).

- [136] Annabelle Bohrdt et al. “Classifying snapshots of the doped Hubbard model with machine learning”. In: *Nature Physics* 15.9 (2019), 921–924. ISSN: 1745-2481. DOI: 10.1038/s41567-019-0565-x (cit. on p. 100).
- [137] Ehsan Khatami et al. *Visualizing Correlations in the 2D Fermi-Hubbard Model with AI*. 2020. arXiv: 2002.12310 [cond-mat.str-el] (cit. on p. 100).
- [138] Philip Zupancic et al. “Ultra-precise holographic beam shaping for microscopic quantum control”. In: *Opt. Express* 24.13 (2016), pp. 13881–13893. DOI: 10.1364/OE.24.013881 (cit. on p. 101).
- [139] Justus Christopher Brüggjenjürgen. “Maßgeschneiderte optische Fallen mit Hilfe örtlicher Lichtmodulatoren”. Bachelor’s thesis. Universität Hamburg, 2017 (cit. on pp. 101, 102).
- [140] Katinka Horn. “Örtliche Lichtmodulatoren zum Einsatz in Quantengasexperimenten”. Bachelor’s thesis. Universität Hamburg, 2018 (cit. on p. 101).
- [141] Marco Stolpmann. “Dynamische optische Potentiale mit einem Lichtmodulator”. Bachelor’s thesis. Universität Hamburg, 2020 (cit. on p. 101).
- [142] Simon Sala, Johann Förster, and Alejandro Saenz. “Ultracold-atom quantum simulator for attosecond science”. In: *Phys. Rev. A* 95 (1 2017), p. 011403. DOI: 10.1103/PhysRevA.95.011403 (cit. on p. 101).
- [143] Dirk-Sören Lühmann, Christof Weitenberg, and Klaus Sengstock. “Emulating Molecular Orbitals and Electronic Dynamics with Ultracold Atoms”. In: *Phys. Rev. X* 5 (3 2015), p. 031016. DOI: 10.1103/PhysRevX.5.031016 (cit. on pp. 101, 102).
- [144] Ferenc Krausz and Misha Ivanov. “Attosecond physics”. In: *Rev. Mod. Phys.* 81 (1 2009), pp. 163–234. DOI: 10.1103/RevModPhys.81.163 (cit. on p. 101).
- [145] Ruwan Senaratne et al. “Quantum simulation of ultrafast dynamics using trapped ultracold atoms”. In: *Nature Communications* 9.1 (2018). ISSN: 2041-1723. DOI: 10.1038/s41467-018-04556-3 (cit. on p. 102).
- [146] M. Lahrz, C. Weitenberg, and L. Mathey. “Implementing supersymmetric dynamics in ultracold-atom systems”. In: *Phys. Rev. A* 96 (4 2017), p. 043624. DOI: 10.1103/PhysRevA.96.043624 (cit. on p. 102).
- [147] Maxim Pyzh et al. “Spectral properties and breathing dynamics of a few-body Bose–Bose mixture in a 1D harmonic trap”. In: *New Journal of Physics* 20.1 (2018), p. 015006. ISSN: 1367-2630. DOI: 10.1088/1367-2630/aa9cb2 (cit. on p. 103).
- [148] N.R. Cooper. “Rapidly rotating atomic gases”. In: *Advances in Physics* 57.6 (2008), 539–616. ISSN: 1460-6976. DOI: 10.1080/00018730802564122 (cit. on p. 103).

- [149] Craig J. Sansonetti et al. "Absolute Transition Frequencies and Quantum Interference in a Frequency Comb Based Measurement of the $^{6,7}\text{Li}$ D Lines". In: *Phys. Rev. Lett.* 107 (2 2011), p. 023001. DOI: 10.1103/PhysRevLett.107.023001 (cit. on p. 105).
- [150] G. A. Noble et al. "Isotope shifts and fine structures of $^{6,7}\text{Li}$ D lines and determination of the relative nuclear charge radius". In: *Phys. Rev. A* 74 (1 2006), p. 012502. DOI: 10.1103/PhysRevA.74.012502 (cit. on p. 105).
- [151] E. L. Hazlett et al. "Realization of a Resonant Fermi Gas with a Large Effective Range". In: *Phys. Rev. Lett.* 108 (4 2012), p. 045304. DOI: 10.1103/PhysRevLett.108.045304 (cit. on p. 111).
- [152] G. Zürn et al. "Precise Characterization of ^6Li Feshbach Resonances Using Trap-Sideband-Resolved RF Spectroscopy of Weakly Bound Molecules". In: *Phys. Rev. Lett.* 110 (13 2013), p. 135301. DOI: 10.1103/PhysRevLett.110.135301 (cit. on p. 111).

Danksagung

Mein erster Dank gilt meinem Doktorvater Klaus Sengstock, der mir bereits seit dem Beginn meiner Bachelorarbeit in seiner Forschungsgruppe immer viel Vertrauen und Ermutigung entgegengebracht und auf diese Weise dazu beigetragen hat, dass ich mich dazu entschieden habe, eine Doktorarbeit an einem neuen Experiment in seiner Gruppe in Angriff zu nehmen. Sein umfangreiches Wissen und seine langjährige Erfahrung in allen technischen und physikalischen Fragen waren unersetzbar für den Aufbau dieses Experiments.

Bei Henning Moritz bedanke ich mich für die Übernahme des Zweitgutachtens und bei allen Mitgliedern der Prüfungskommission dafür, dass sie sich freundlicherweise dazu bereit erklärt haben, diese Aufgabe zu übernehmen.

Ein großer Dank gilt natürlich Christof Weitenberg, der gemeinsam mit Klaus Sengstock der PI unseres Experiments ist. Sein unermüdliches Engagement und seine immer wieder neuen Ideen haben entscheidend zum Gelingen dieser Promotion beigetragen. Darüber hinaus habe ich durch die intensive Zusammenarbeit mit ihm in den letzten Jahren sehr viel von ihm lernen können. Außerdem möchte ich mich bei ihm sehr für das Korrekturlesen meiner kompletten Doktorarbeit bedanken.

Ebenso gilt mein Dank Benno Rem, der für einen Großteil meiner Promotion Postdoc an unserem Experiment war. Von ihm habe ich ebenfalls viel gelernt und er hat in seiner Zeit bei uns das Experiment entscheidend mitgeprägt.

Ein persönlicher Dank gilt meinem Mitdoktoranden Andreas Kerkmann, mit dem ich einen Großteil meiner Masterarbeit und meiner Promotion gemeinsam im Labor verbracht habe. Ich bedanke mich bei ihm für die vertrauensvolle Zusammenarbeit, die kontinuierliche Unterstützung und dafür, dass wir schon seit längerer Zeit auch außerhalb des Labors freundschaftlich miteinander verbunden sind.

Außerdem bedanke ich mich herzlich bei Mathis Fischer, Justus Brüggjenjürgen und Tobias Petersen, die in verschiedenen Funktionen nun auch schon lange Mitglieder unseres Teams sind und mit denen die Zusammenarbeit an jedem Tag eine besondere Freude ist. Darüber hinaus möchte ich mich bei den vielen Hiwis, Bachelor- und Master-Studierenden bedanken, die wertvolle Beiträge zu unserem Experiment geleistet haben. Dazu gehören Jan Mika Jacobsen, Niels Rohweder, Cora Braun, Bojan Hansen, Yann Kiefer, Katinka Horn, Malte Hagemann, Jonathan Schwardt, Bastian Lunow, Jinggang Xiang, Vivien Sleziona, Corinna Menz, Nora Bidzinski, Silvan Heinrich und Niklas Käming.

Bei der gesamten Forschungsgruppe von Klaus Sengstock möchte ich mich für die stets freundliche und sehr kooperative Arbeitsatmosphäre bedanken. Ich schätze alle meine Mitdoktoranden sehr und freue mich darüber, einige von ihnen mittlerweile als gute Freunde bezeichnen zu dürfen. Den Post-Docs und Senior-Scientists unserer Forschungsgruppe, namentlich Juliette Simonet, Christoph Becker, Ortwin Hellmig und Philipp Wessels-Staarmann, danke ich für die stets gute Zusammenarbeit und für die sehr wertvolle Unterstützung bei vielen Gelegenheiten.

Ich bedanke mich natürlich auch herzlich beim Personal für Technik und Verwaltung für stets freundliche und kompetente Unterstützung. Von den vielen Personen, mit denen man im Laufe einer Promotion in Kontakt kommt, möchte ich an dieser Stelle namentlich Ellen Gloy, Nadja Wardenburg, Janina Neubert, Loreen Tornier, Sylke Strien, Dieter Barlösius, Ralf Lühr und Reinhard Mielck nennen. Die immer hilfsbereite und kompetente technische Unterstützung von Reinhard Mielck war unerlässlich für den Aufbau der Infrastruktur eines neuen Experiments. Dafür danke ich ihm ganz herzlich.

Als Experiment im Aufbau hat man außerdem einen ständigen Bedarf für individuell gefertigte Bauteile aus verschiedenen Materialien. Deswegen danke ich der Standortwerkstatt Bahrenfeld für die stets gute Zusammenarbeit, insbesondere dem Werkstatteleiter Stephan Fleig und seinem Stellvertreter Frank Jonas.

Zuletzt gilt mein Dank natürlich meiner Familie und meinen Freunden, die mein gesamtes Studium und die anschließende Promotion mit viel Interesse, Unterstützung und Rücksicht begleitet haben.

Eidesstattliche Erklärung

Hiermit versichere ich an Eides statt, die vorliegende Dissertationsschrift selbst verfasst und keine anderen als die angegebenen Hilfsmittel und Quellen benutzt zu haben. Die eingereichte schriftliche Fassung entspricht der auf dem elektronischen Speichermedium. Die Dissertation wurde in der vorgelegten oder einer ähnlichen Form nicht schon einmal in einem früheren Promotionsverfahren angenommen oder als ungenügend beurteilt. Es sind keine Vorveröffentlichungen aus dieser Dissertation hervorgegangen.

Unterschrift:

Datum:
